A Laboratory Study on the Kinematic and Pressure Responses of an Internally Pressurized Novel Surrogate Headform Subjected to Blunt Impacts

by

Ashton Alexander Martin

A thesis submitted in partial fulfillment of the requirements for the degree of

Master of Science

Department of Mechanical Engineering

University of Alberta

Abstract

Instrumented surrogate head models – each of which exhibits varying degrees of complexity – are employed to study traumatic brain injury and mild traumatic brain injury. Despite advancements over the years, many existing surrogate head models lack a pressurized cerebrospinal fluid (CSF) or CSF-simulant layer. The significance of CSF has been underscored as a form of mechanical protection and a shock absorber during impacts between the brain and skull. However, the precise biomechanical role that CSF plays during head impacts remains largely unknown. The Brain Injury Protection Evaluation Device (BIPED) developed at Defence Research and Development Canada, was modified, and used to elucidate the role of CSF within an artificial surrogate headform.

To better grasp the role of CSF, particularly its positive pressure, this thesis explored how changing the internal resting pressure in a novel surrogate headform (BIPED) affects its kinematic and pressure responses to blunt impacts. Furthermore, a limited biofidelity assessment of the pressurized BIPED was performed. This thesis aims to enhance our understanding of how resting pressure influences surrogate headforms and if it requires control when designing, constructing, and using these headforms to study head and neck injury.

A set of Schrader valves were added to the second iteration of the BIPED (BIPED Mk. 2) which enabled and maintained headform pressurization. Further additions to the BIPED included four miniature pressure sensors embedded within the inner surface of the skull at the anterior, posterior, left, and right surfaces. The BIPED also possessed two intraparenchymal pressure (IPP) sensors embedded within the surrogate brain as well as a triaxial accelerometer and gyroscope sensor.

The BIPED underwent blunt pendulum impacts to the forehead along the sagittal plane at four pressure levels: 0, 3, 6, and 9 inH2O-gauge. Each pressure level received five impacts at 18.8, 37.7, and 65.9 J of energy. Parameters such as peak linear head acceleration, maximum front CSF-layer intracranial pressure (ICP), maximum anterior (front) intraparenchymal pressure (IPP), maximum posterior (back) IPP, and minimum back IPP were recorded and analyzed. Comparisons between zero and non-zero gauge pressure cases revealed that, except for maximum back IPP away from the impact site, none of the listed response parameters differed by more than 10% from the zero-pressure configuration. Notably, the maximum back IPP increased by up to 35% when the resting ICP was raised. These results reflect the intricate nature of the cumulative pressure wave progression from the impact site throughout the intracranium.

A limited biofidelity assessment was also undertaken to evaluate the efficacy of using the resting ICP to tune the surrogate head model's response to improve consistency with a cadaver model. The BIPED's responses to the pendulum impacts were compared to relevant sets of the cadaver experiments previously completed by Nahum and Smith. CORrelation and Analysis (CORA) was used to compare the time histories of the global head linear acceleration, and front and left CSF-layer ICP. Subsequently, the CSF ICP-acceleration responses of the BIPED were compared to cadaver data using linear regression methods. This involved incorporating additional parameters for head model type and the interaction effect between head model type and head acceleration to explore differences between the models. The CORA ratings for each BIPED Mk. 2 pressure configuration were 0.614, 0.616, 0.612, and 0.617 when compared to experiment 37 from Nahum and Smith. Overall, these ratings are below 0.7 – the generally accepted threshold for "good" biofidelity. The interaction effects for each BIPED resting ICP configuration were observed to be non-significant when compared to a diverse cadaver specimen set while the

interaction effects compared to a single cadaver specimen were indeed significantly different. This suggests that the BIPED offers a reasonable representation of an aggregate response not significantly different from a diverse collection of specimens. Taken together, the BIPED Mk. 2 was considered to be moderately biofidelic. Additionally, these results indicate that altering the resting ICP does not improve or diminish the biofidelity of the BIPED.

Overall, although changing the resting ICP may alter the intracranial and intraparenchymal pressure wave interactions, the absolute maximum pressures the surrogate brain experiences during a blunt impact are not expected to deviate significantly. The largest variations in the headform's response due to changing resting ICPs were observed in the positive pressures opposite the impact site – away from where peak positive pressures typically occur in head impacts. Moreover, altering the resting ICP does not improve nor diminish the biofidelity of the BIPED.

Preface

This thesis is the work of Ashton A. Martin. The completed work contributes to the larger efforts of an NSERC Alliance grant project between Defence Research and Development Canada (DRDC) and the University of Victoria and the University of Alberta. The work presented within this thesis is largely contained within the manuscript located in Appendix A. The paper includes the background information presented in chapter 1, the experimental setup in chapter 3, the results from chapter 4, and the relevant conclusions from chapter 6. At the time of submission, this manuscript is still being prepared for submission to the ASME Journal of Biomechanical Engineering.

- Martin, A.A., Chauvet, R., Brice, A., Ouellet, S., Westover, L., and Dennison, C.R., 2024, A laboratory study on the kinematic and pressure responses of an internally pressurized novel surrogate headform subjected to blunt impacts, J Biomech Eng (IN PREPARATION)

While DRDC provided the headform and guidance on its use, the author of the thesis is responsible for modifying the surrogate headform, conducting the experiment described within, and writing the majority of the manuscript attached in the appendix with occasional assistance from Aaron Brice, Robert Chauvet, and the remainder of the University of Alberta and Victoria research teams. The research project did not require ethics approval.

The views and conclusions contained in this document are those of the author's and should not be interpreted as representing the official policies, either expressed or implied, of DRDC or the Department of National Defense (DND). This work does not necessarily represent the opinions of DRDC or the DND.

Dedications

I would like to dedicate this to my mother, Melinda Martin. Without her, I would not be where I am today.

Acknowledgements

First and foremost, I would like to express my deepest gratitude to Dr. Christopher Dennison. As I reflect on the journey that began nearly nine years ago when I first stepped into the world of injury biomechanics, my heart overflows with gratitude for the unwavering guidance and mentorship you have provided. Your belief in my potential, your dedication to my growth, and your wisdom have been the bedrock upon which my academic and professional foundation rests.

To Dr. Lindsey Westover, I would also like to express my gratitude. Throughout these past 5 years, your mentorship has been more than just professional guidance; it has been a profound source of inspiration and support. Your patience, encouragement, and genuine commitment to my success have been instrumental in shaping not only my technical skills but also my resilience and passion for this field.

As I embark on the next chapter of my journey, I carry with me the invaluable lessons, skills, and, above all, the spirit of dedication and excellence that you both have instilled in me. I am profoundly grateful for the immeasurable impact you both have had on my academic and professional development. Thank you, not just for being supervisors, but for being mentors, and sources of inspiration. The lessons I've learned from you will continue to shape my career and life.

To my current and former lab mates, thank you for your collaboration, creativity, and the shared moments of both challenge and triumph. Working alongside such a talented and dedicated group has been an enriching experience that I will carry with me into the next phase of my journey.

And lastly to my cherished family, dear friends, and those who never failed to inquire about the progress of my thesis, your unwavering support has been a beacon of inspiration throughout this journey. Your encouragement has not only propelled me toward the finish line but has infused each day with renewed vigor and purpose. From the bottom of my heart, thank you for being the driving force behind my perseverance and success.

Table of Contents

List of Tables

List of Figures

Chapter 1: Introduction

1.1 Motivation

Recent studies indicate that, globally, up to 69 million people per year sustain a traumatic brain injury (TBI) [1], [2], [3]. In the US alone, the cost of TBI, both directly and indirectly, was estimated to be around $76 billion in 2010 [1], [4], [5]. In an effort to mitigate the incidence and economic impact of TBI, researchers investigate the biomechanics leading to TBI using various types of head models that are much more ethical and cost effective than *in-vivo* human subjects, or cadavers. In recent years, significant advances have been made in the development of artificial surrogate headforms. Each of these surrogate head models is characterized by different levels of complexity and attention to replicating the intricacies of the human head's anatomy [6]. Although many of these surrogate models are quite complex in nature, such as the Wayne State University head model that features a surrogate gel brain, very few models possess a cerebrospinal fluid simulant like the Realistic Explosive Dummy (RED) Head developed at the University of Nebraska [7] [8], [9], [10], [11]. Even fewer models, in fact, possess extensive intracranial instrumentation like the Brain Injury Protection Evaluation Device (BIPED) and the Instrumented Human Head Surrogate (IHHeadS_1) developed at Defence Research and Development Canada and the University of Padova respectively [12], [13], [14]. Despite the advances made with surrogate headforms and the efforts made towards anatomical biofidelity, the precise role that CSF plays during head impacts remains largely unknown and largely unexplored. The BIPED, however, provides a unique opportunity to investigate this further.

The BIPED is an instrumented headform designed by DRDC Valcartier Research Centre and is used for evaluating head protection devices subjected to insults that can cause mild to severe brain injuries. Such insults include, but are not limited to, blasts and blunt impacts. At the time of writing, extensive blast experiments have been performed with the BIPED, but it has yet to be subjected to similarly extensive blunt impact scenarios. However, the existing studies that make use of the BIPED for blunt impact testing provide a reliable foundation for further studies. To date, the blunt impact scenarios the BIPED has been tested in are vertical drop tower and pendulum experiments [15], [16], [17], [18], [19]. These studies assessed the BIPED's biofidelity [16], [17], [18], with regards to its kinematic and pressure responses, and its capabilities of measuring the

attenuation of protective headgear [15], [19]. Moreover, since the BIPED possesses a CSF layer that can be filled with a simulant fluid, it is possible to pressurize the fluid after making some modifications to the head itself. Taken together, the BIPED can serve as the model for this thesis.

1.2 Background

Artificial surrogate headforms have been widely used in the field of biomechanics to study the response of the human head to blunt impacts. These models serve as simplified representations of the human head and are used to simulate real-world scenarios to understand how energy is delivered to the head during injury-causing events. In order to record meaningful responses, the devices themselves must be as anatomically biofidelic as possible so as to not disrupt the response during injury/loading scenarios [6].

At present, researchers have developed (or are developing) several surrogate headforms, each with varying levels of complexity and detail aimed to mimic the anatomy of the head. Models such as the Hybrid III, shown in Figure 1-1, possess a surrogate skull made of metal alloys enveloped by a soft vinyl skin but lack a surrogate brain among all other intracranial anatomy [20], [21]. The head model developed by Hodgson et al. at Wayne State University, shown in Figure 1-2, sought to improve the biofidelity of available headforms that could be used for impact safety standards compliance tests in automotive contexts [7]. Although the skull of this particular headform is made of a self-hardening urethane foam that contains a cranial cavity, in which a surrogate gel brain was cast, the model lacks any instrumentation that measures intracranial responses aside from a triaxial accelerometer located at the head center-of-gravity (CoG) [7]. The Realistic Explosive Dummy (RED) Head, shown in Figure 1-3, developed at the University of Nebraska by Sogbesan and Ganpule, however, did possess such instrumentation. The RED head was based on the Facial and Ocular Countermeasure Safety (FOCUS) headform and is meant to replicate the 50^{th} percentile male soldier [8], [9], [10], [11]. It possesses a polyurethane skull and an instrumented cranial cavity for a surrogate brain and cerebrospinal fluid simulant (CSF-simulant). However, the intracranial instruments were abandoned in favor of using an accompanying Finite Element model (FE model) to predict intracranial responses. This was accomplished by physically simulating a loading scenario (blast), measuring the applied load with externally-mounted pressure sensors, and applying this measured input to the FE model [8], [9], [10].

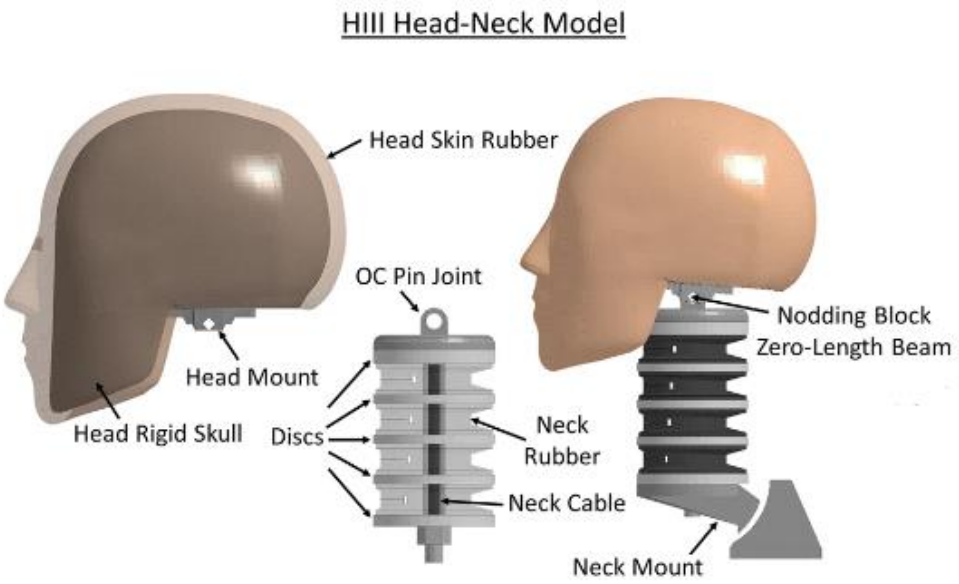

Figure 1-1: Hybrid III head model. Figure was adapted from Giudice et al. [22].

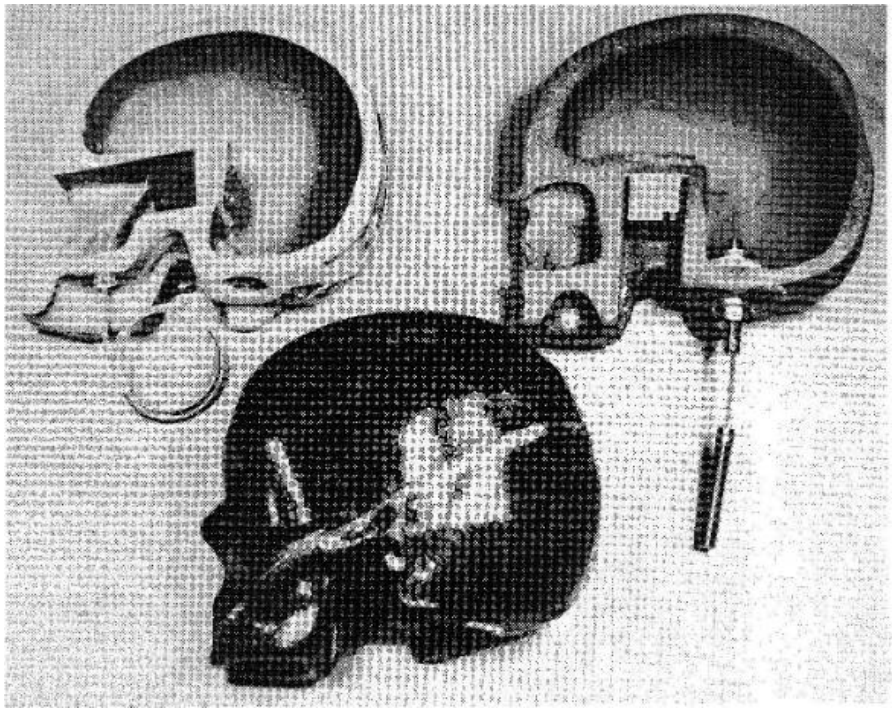

Figure 1-2: Wayne State University head model. Figure was adapted from Hodgson et al. [7].

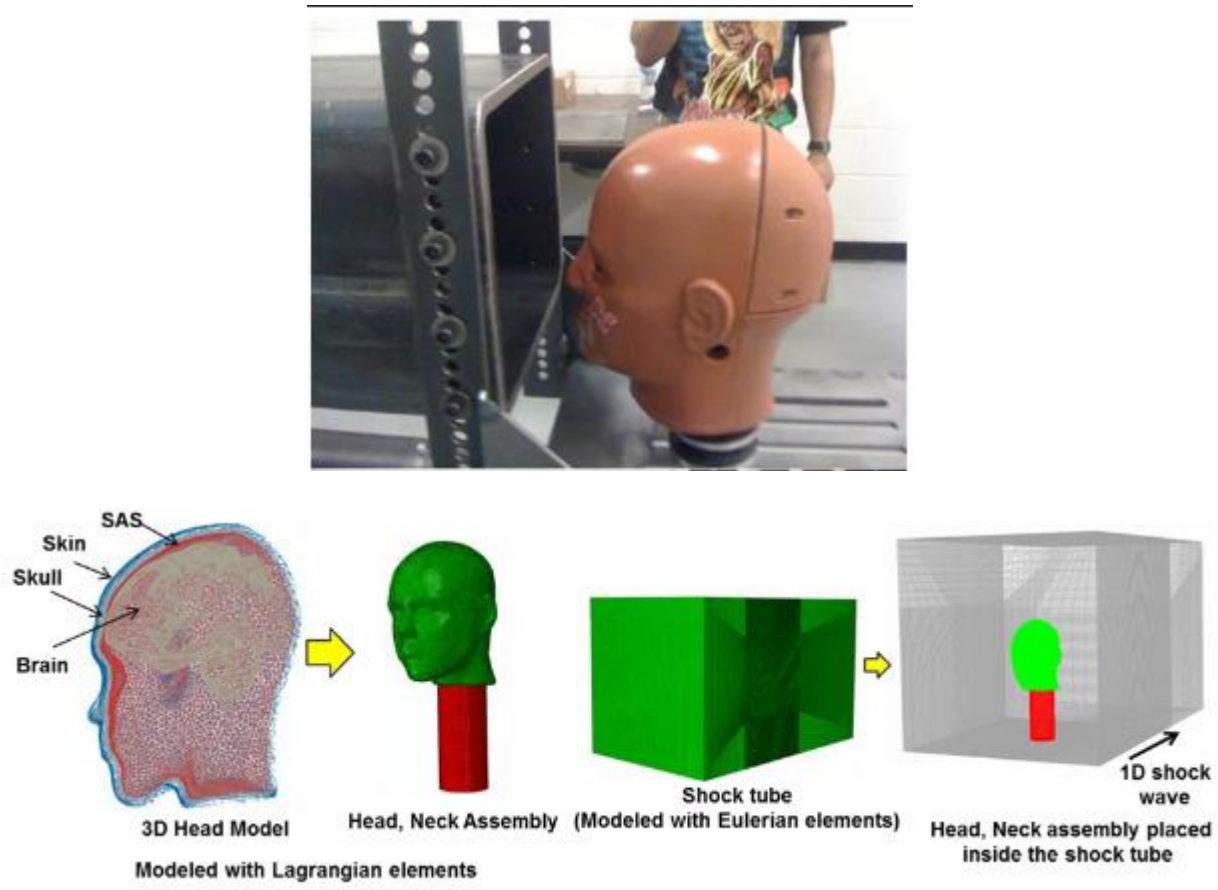

Figure 1-3: Realistic Explosive Dummy (RED) Head physical model and FE model developed by Sogbesan [8] and Ganpule [9], [10]. Figure was adapted from Sogbesan [8] and Ganpule [9].

More recently developed models make use of their intracranial instruments to measure brain parenchyma accelerations, angular velocities, and pressures. Examples include the Brain Injury Protection Evaluation Device (BIPED), shown in Figure 1-4, and the Instrumented Human Head Surrogate (IHHeadS_1), shown in Figure 1-5, which feature a plastic skull, a urethane or gel skin, a gel brain, and can contain a cerebrospinal fluid simulant (CSF-simulant) [12], [13], [14]. Not only did these features serve to improve the anatomical likeness of either head model, they were carefully instrumented to record the responses in each of the head models' components [12], [23], [15], [18], [13], [14]. The BIPED's surrogate brain contains pressure sensors that measure intraparenchymal stresses while the surrogate skull can be modified to measure external pressure waves and internal stresses and pressures at the CSF layer [12], [15], [18], [23]. Meanwhile, the IHHeadS_1 features nine triaxial accelerometers and ten pressure sensors to measure head kinematics and intracranial pressures at various local regions throughout the head model [13], [14].

This allowed researchers to gain a deeper understanding of the mechanisms that lead to brain injury as a result of several loading scenarios [12], [23], [15], [18], [13], [14].

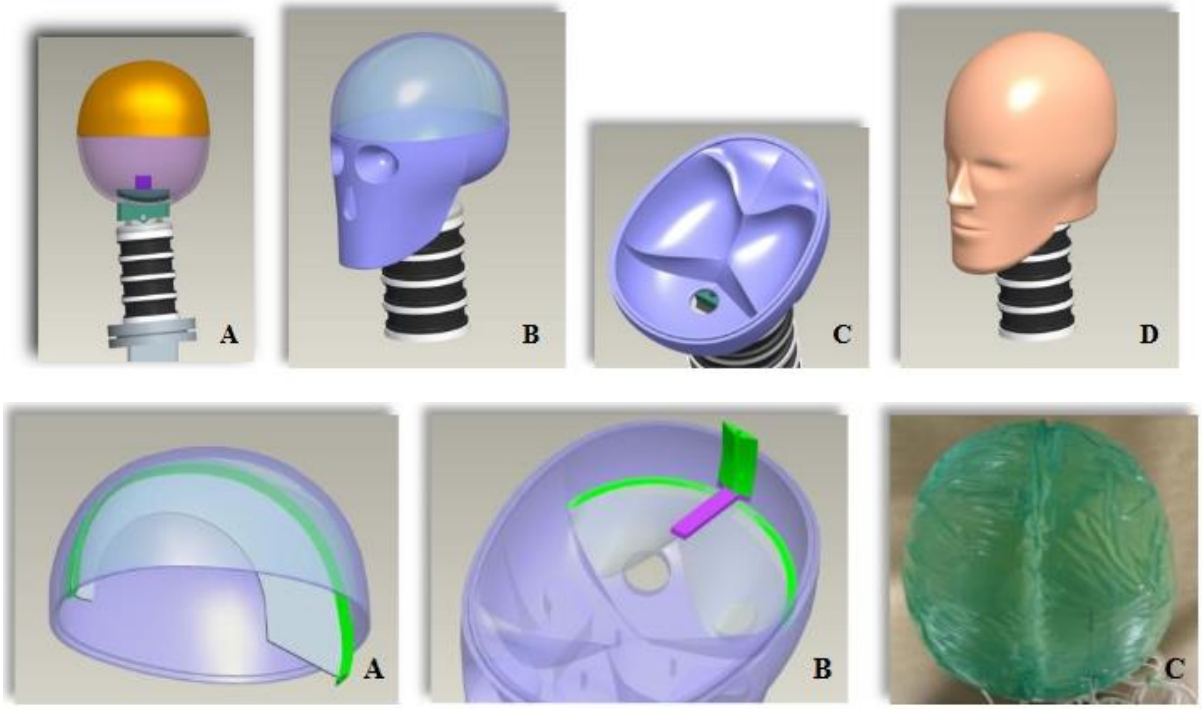

Figure 1-4: Brain Injury Protection Evaluation Device (BIPED), originally named the Blast-Induced Brain Injury Protection Evaluation Device (BI^2PED) developed by Defence Research and Development Canada – Valcartier. Figure was adapted from Ouellet et al. [12].

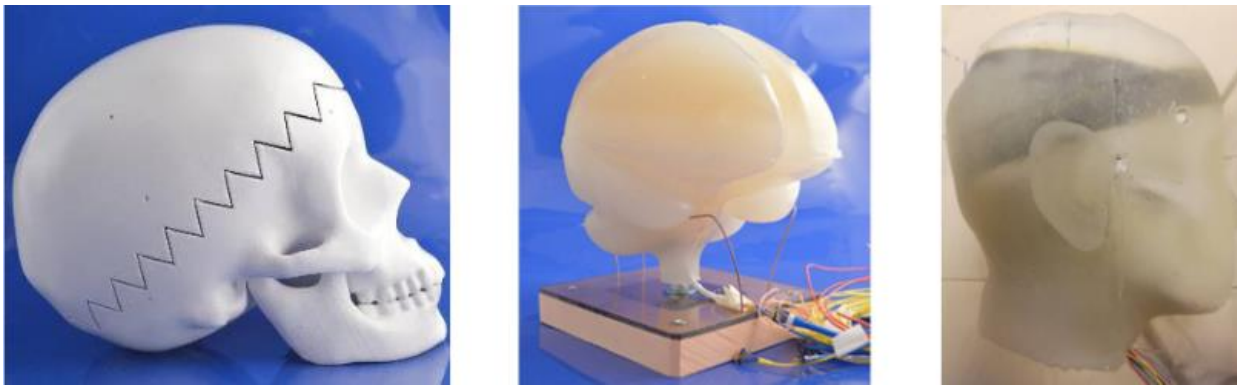

Figure 1-5: Instrumented Human Head Surrogate (IHHeadS_1) developed at Mid Sweden University, Ostersund-SWE in collaboration with University of Padova-IT. Figure was adapted from Petrone et al. [13].

Although these more anatomically correct artificial surrogate headforms possess many biofidelic features, the accurate representation of the resting intracranial pressure (ICP) in these models has remained a challenge. In practice, artificial headforms that contain CSF-simulant are filled with simulant while simultaneously evacuating the cavity of air until the fluid composition within the cranial cavity is nearly 100% CSF-simulant. However, no additional steps are taken to pressurize the cavity to known *in-vivo* levels [12], [13], [14].

The average resting ICP in healthy humans is approximately between 7 and 15 mmHg when measured via spinal tap while subjects are supine. This is the pressure that can be measured in the space occupied by the CSF. In general, it has been more practical to account for this pressurization in human cadaver, animal, and finite element head models used for injury biomechanics research. In the case of the cadaver models, head models were generally perfused via the ventricular duct to a consistent pressure through the course of the experiments to restore the rigidity of otherwise flaccid brain tissue such that it may properly interact with the skull during experiments as was noted by Stalnaker et al. [24]. The perfusion pressure also facilitated the marking of structural brain damage with the use of a staining technique that was infused with the perfusion fluid [24]. Nahum and Smith [25], [26] pressurized their cadaveric models to 74 mmH_2O (5 mmHg) at the ventricular level while Hardy et al. [27] maintained a perfusion pressure of 75 mmHg at the carotid artery. Similar to Hardy et al., Alshareef et al. perfused their head model to 78 mmHg to explore brain motions during head rotations [28]. Following Stalnaker et al. [24], Got and Patel [29] also recognized the importance of pressurizing their cadaver models to ensure proper brain-skull interactions. As such, they pressurized their specimens until they obtained a reading of 120 mmHg at the carotid artery [24], [29]. By pressurizing their respective cadaver head models, these researchers were able to alter intracranial interactions for their experiments. However, none of the aforementioned investigators reported any explorations into the effects of altering this cranial pressure.

Most studies that utilize animal models are *in-vivo* experiments, therefore ICP may only be measured rather than controlled. Moreover, ICP is not necessarily measured during the impact event, rather, it is measured before impact and at several instances post-impact to allow for comparison of between-subject ICP and cognitive performance [30], [31], [32]. In these studies, the ICP is not controlled to illicit different responses to injury, rather, it is used as a medium by

which to measure the post-injury physiological response [30], [31], [32]. A surrogate model with a pressurized CSF-layer, unfortunately, cannot make use of this function.

In-silico finite element (FE) models, present a much easier opportunity to implement changes in material properties. Pressure changes in the CSF can be reflected by simple material changes to the CSF bulk modulus. However, the extent of the changes that an increased CSF pressure will effect remains largely unknown *in-vivo*. Because of this, it is difficult to assume that FE models can accurately and completely represent the physical and mechanical effects of the increase in CSF pressure especially since FE models are limited in how they model the CSF layer. Even industry standard models of the human head, such as the SIMON and GHBMC, use a Lagrangian solid to represent the fluid layer rather than a multiphysics fluid approach [33], [34]. This poses difficulties in changing the properties of a solid in order to represent the changes to a fluid. An FE model of the BIPED has also been created [19], [35], which also relies on a Lagrangian solid for its fluid layer. While the opportunity to implement changes in CSF pressure are greatest in FE models, the advances in modelling a multiphysics fluid layer limit the confidence that blunt impact experiments accurately represent the physiological response in the human head [19]. To gain confidence in the biofidelity of these experiments, the role of CSF must first be considered before the mechanical responses, and the underlying physiological responses, that present after blunt head impacts following changes in CSF pressure can be understood.

The CSF is primarily generated in the ventricular system and occupies this space as well as the subarachnoid space surrounding the brain and the spinal cord [36], [37], [38]. It is composed of approximately 99% water while the rest is proteins and minerals. CSF serves three primary functions: (1) nourishment, (2) waste removal, and (3) protection [36]. The former two purposes are achieved by allowing nutrients to pass to the brain and removing waste excreted by the brain [36]. CSF offers chemical/molecular protection to the brain by disallowing harmful molecules to pass. When immersed in CSF, the brain and spinal cord gain a form of mechanical protection since they are neutrally buoyant [36], [39]. Moreover, the CSF serves as a shock absorber to lessen the severity of brain-skull impacts [36], [37], [38], [39]. Based on this, some researchers conducted further studies on the CSF's shock-absorbing abilities. These studies suggest that increasing this resting intracranial pressure can reduce relative motion between the brain and skull during a head impact through a phenomenon coined as "slosh mitigation" [40], [41], [42]. It is thought that the

added pressure forces the CSF to occupy previously empty space thus limiting the volume within which the brain can move [40], [41], [42].

Here, we wish to consider another potential effect of increasing the resting ICP in the CSF-layer that would be observed during blunt impacts to the head. As mentioned previously, pressure changes in the CSF can be represented by minute changes to the bulk modulus of the CSF-layer assuming the volume available for the CSF remained unchanged. Although small, this change may affect the overall shell stiffness of the skull, which may have a cascading effect on the pressure wave that develops during an impact event. Kopecky and Ripperger demonstrated that different pressure amplitudes are observed after impacting a fluid-filled closed shell by changing either the fluid bulk modulus or the shell stiffness [43]. This phenomenon has been implicitly explored by previous researchers when investigating the pressure waves that develop in head models that are subjected to blunt impacts or to blasts [9], [10], [15], [44], [45], [46].

It is well known that the pressure wave that forms within the brain during an impact or blast is caused and affected by several factors. The most obvious and largest contributor to this pressure wave is the component generated by the brain colliding the skull at the coup site. This produces a longitudinal and a shear stress wave with a duration of 5 to 10 ms as seen in Nahum and Smith [26], Hardy et al. [27], and in Pearce et al. [47]. Prior to this brain-skull collision, however, another contributing pressure wave is generated. At impact, the skull deforms which generates a flexural wave that propagates through the skull (or surrogate skull) itself. Along the way, the rippling flexural waves generate further stress waves in the CSF that are then passed onto the brain and culminate into a resultant stress wave in the parenchyma [9], [10], [44], [47], [48], [49]. This stress wave has a duration of approximately 0.5 to 2 ms as seen in blast experiments and blunt impact experiments with smaller objects traveling at high velocities [9], [15], [44], [45], [46]. Ganpule et al. discuss the complex nature of the pressure (stress) field within the brain and how the intracranial response to injury largely depends on the interactions of all these wave components [10], [44]. Therefore, if changing the resting pressure of the CSF affects the effective shell stiffness of the skull, any flexural waves generated or transmitted through the skull may indeed be affected.

In addition to the flexural waves, wave speeds in and around the brain itself may be affected by increasing the resting ICP. Zhang et al. demonstrated that the longitudinal wave speed within an object under a compressive load increases logarithmically [50], while Ottenio et al. and

Destrade and Ogden analytically demonstrated that compressing a hyperelastic object ultimately leads to altered wave speeds [51], [52]. As such, under different compressive loads, the brain may transmit some or all of the components of the pressure wave at different speeds. Altogether, these changes may be enough to significantly affect the locations and magnitudes of the maximum stresses experienced within the brain.

1.3 Problem Statement

To deepen our understanding of the role of the CSF – in particular, the role of the positive pressure of the CSF – an experimental series presented herein explores the effects of changing the internal resting ICP of a surrogate headform (the BIPED Mk. 2). The surrogate headform is subjected to blunt impacts while measuring global head kinematic, intraparenchymal pressure (IPP), and intracranial pressure (ICP) responses. The goal of this thesis is to determine if pressurizing the CSF-layer alters the surrogate headform's responses to blunt impacts. The results from this work will provide valuable insight and may contribute to the development of more accurate injury prediction models.

1.4 Thesis organization

The remainder of this thesis is divided into 5 chapters. Chapter 2 discusses the modifications made to the surrogate headform to allow for pressurization. Chapter 3 describes the blunt impact experimental setup and procedure. Chapter 4 discusses the results of the experiment and the effect of the changing the resting ICP within a high-level mechanical context while Chapter 5 discusses the results in comparison to cadaver literature and provides a limited assessment of the BIPED's biofidelity. Lastly, Chapter 6 contains the overall conclusions and suggestions for future work.

Chapter 2: Modifications to a Surrogate Headform

Chapter 2 describes the modifications that were made to the BIPED Mk. 2 surrogate headform to allow for pressurization of the intracranial space. The modifications included the addition of Schrader valve and pressure sensors to the headform, as well as the construction of a simple tool that can be used to set the pressure of the intracranial space.

2.1 Addition of Schrader Valves

The BIPED Mk. 2 was selected to explore the effects of increasing the resting ICP in an artificial head model because it features a cranial cavity that can be filled with CSF-simulant and it has since been tested for several head injury scenarios, including blunt impacts [12], [15], [16], [18], [23]. The BIPED is comprised of a two-part polyurethane skull, a surrogate gel brain with sulci and gyri features molded around two intraparenchymal pressure (IPP) sensors, a urethane rubber outer skin layer, neoprene tentorium and falx membranes, aluminium nodding block and counterbalance, and an accelerometer/gyroscope unit as shown in Figure 2-1 [12]. Once the membranes, brain, and instrumentation are assembled and sealed within the skull with a urethane adhesive, the BIPED's cranial cavity can then be filled with water as the CSF-simulant [12]. This was originally accomplished by adding water to the fill port at the vertex of the skull until full and then sealing the port with a plug and silicone sealant. By this method, the internal pressure of the BIPED was thus consistent with the atmospheric pressure at the time of sealing (along with any minor changes contributed by inserting the plug). To pressurize the intracranial space, however, the BIPED skull required modifications to its fill port such that any additional water added to the cavity to increase the pressure must be held in place to maintain said pressure and, subsequently, the port must be able to be rapidly sealed. Two valve options were considered for this role: inflation valves for sports balls and Schrader valves.

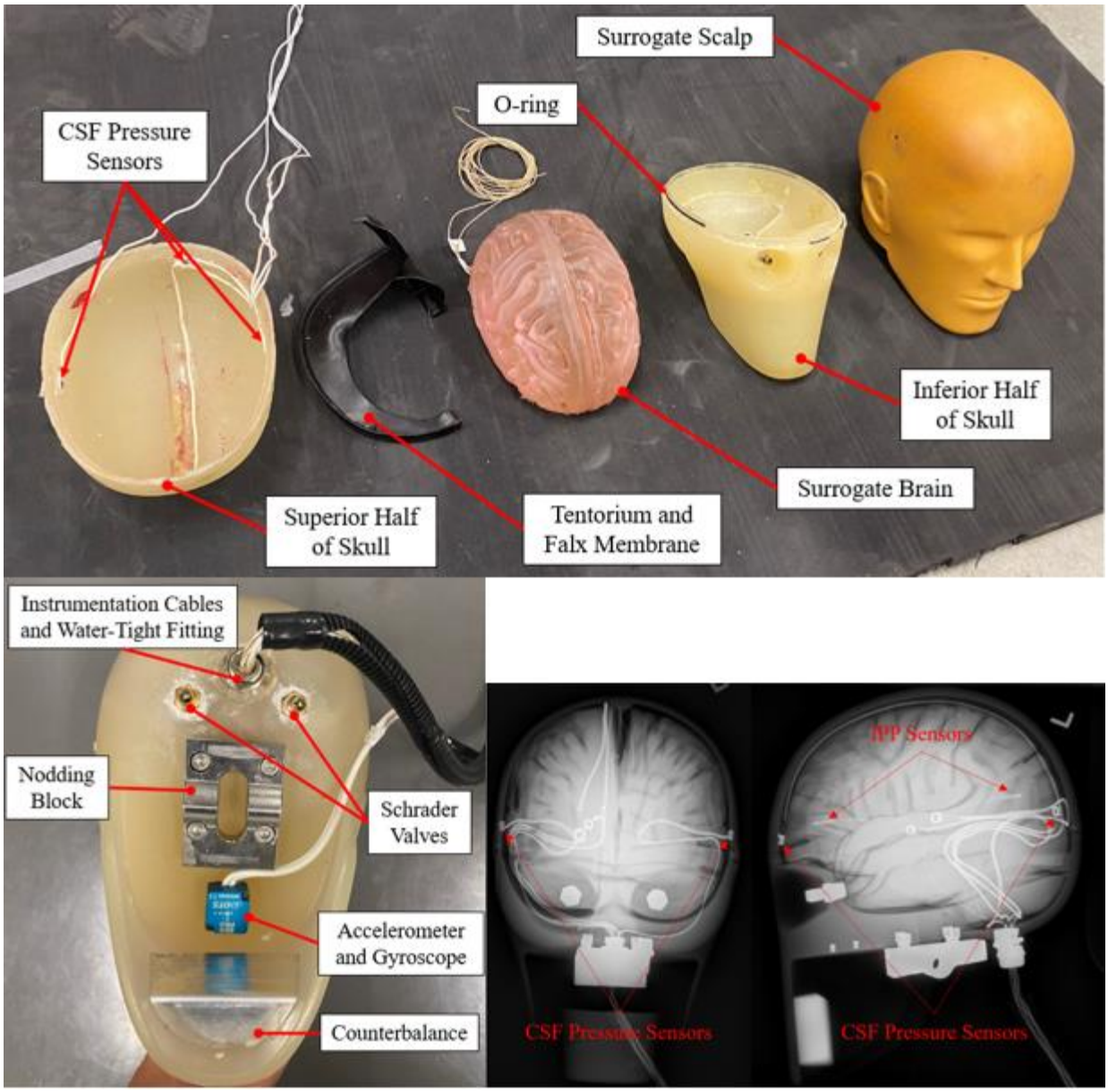

Figure 2-1: The BIPED Mk. 2 shown in its original components, inferiorly when fully assembled, and under x-ray. All components are part of the original design except for the CSF pressure sensors and the valves that were added for this work. The CSF pressure sensors and the intraparenchymal pressure (IPP) sensors are visible in the x-ray image.

Typical inflation valves that are found in basketballs, soccer balls, etc. were first considered for pressurizing the cranial cavity. It is a specialized valve designed to inflate, maintain, and release air pressure in sports balls They are engineered for durability and ease of use, catering to the specific needs of sports equipment. Inflation valves are typically made of durable materials like rubber or rubber-like compounds. The valve is inserted into a hole in the ball, shown in the diagram in **Figure 2-2**, during manufacturing and can be replaced if damaged. Within the ball, the valve

features an oval patch with a central stem that extends into the ball. This stem accommodates an inflation needle while the patch seals the hole. When pressure is applied through the needle, the valve stem's internal mechanism, which is often a one-way valve, allows air to flow into the ball but prevents it from escaping. This one-way design ensures that the ball stays inflated during play. This further allows for precise control over the air pressure inside the ball. Air can be added to increase pressure for a firmer ball or released to decrease pressure for a softer feel, depending on the requirements of the specific sport. The design of these valves is aimed at preventing air leaks [53].

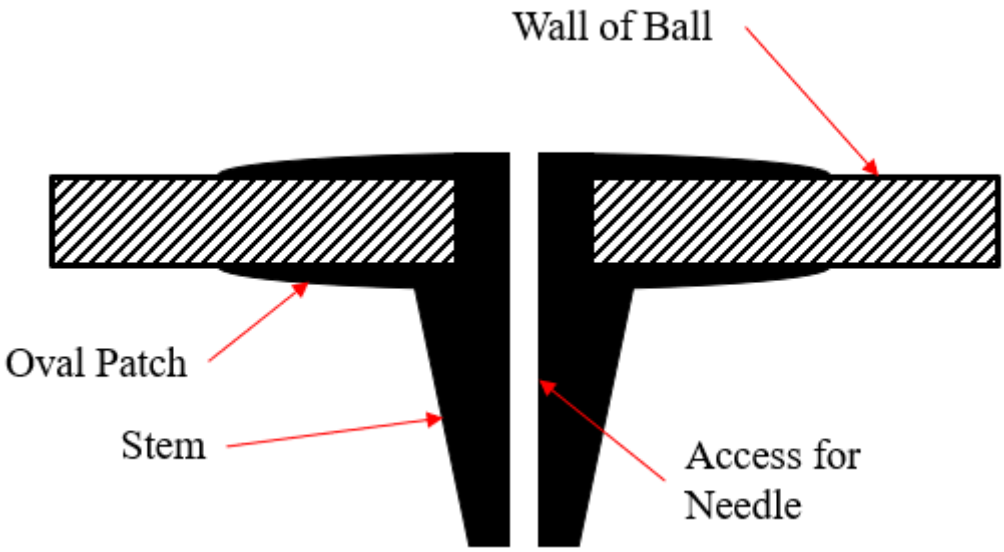

Figure 2-2: Cross-section of inflation valve inserted into the wall of a sports ball.

Schrader valves perform a similar function but operate in a different manner. They are commonly used in pneumatic and hydraulic systems, with their most widespread application found in tires, particularly in cars, bicycles, and motorcycles. A Schrader valve's primary function is to control the inflation and deflation of a container, typically a tire, by allowing air to enter or exit when needed. Schrader valve installation depends on the type of valve. Valves that terminate in a rubber seal, as shown on the left in Figure 2-3a, require that the seal be adhered to the inner surface of the container in which it is used. Valves that terminate in pipe threads, as shown on the right in Figure 2-3a, simply require a congruent threaded connection and additional adhesive if desired. To inflate or fill a container with a Schrader valve, the fluid supply line is directly connected to the Schrader valve. The valve's core, which is a small threaded pin inside the valve stem, is depressed by the pump or compressor, allowing fluid to flow into the container. This open position

is shown on the left in Figure 2-3b. Once the desired pressure is reached, the Schrader valve prevents fluid from escaping the container. As the supply is disconnected, the valve core is no longer depressed, so it seals the opening and maintains the pressure within the container as shown on the right in Figure 2-3b. This is crucial for keeping the container at the desired inflation level. For deflation, a Schrader valve tool (a simple, hand-held device) can be attached to the valve stem to depress the valve core. This releases the fluid. Again, once the desired pressure is reached, allowing the core to return to its closed state will seal the container. In addition to inflation and deflation, Schrader valves also facilitate pressure measurement. For example, tire pressure gauges are designed to connect to the valve stem, allowing one to check the tire's pressure easily. By depressing the valve core with the gauge, an accurate reading of the tire's pressure can be obtained [54].

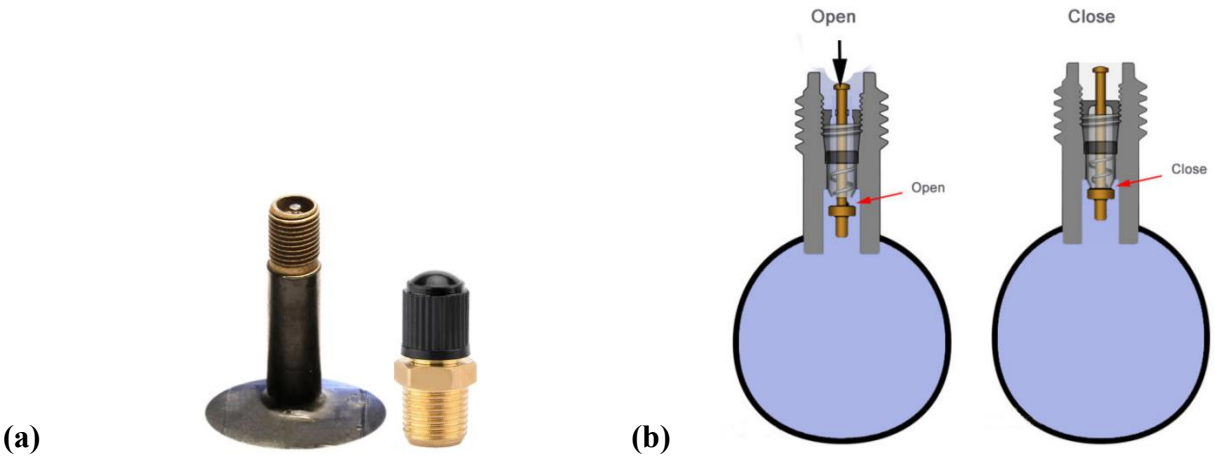

Figure 2-3: (a) A Schrader valve with a rubber seal that is often used in tires is shown on the left while a threaded tank valve is shown on the right. (b) Demonstration of the function of a Schrader valve. The left image shows the depressed core which opens the valve. As soon as pressure is removed from the core, it retracts and closes the valve as shown on the right [55]

Inflation valves and Schrader valves both possess their own advantages and disadvantages; however, the threaded Schrader valve was ultimately chosen as the fill port replacement for the BIPED. When deciding on the valve to select, factors such as cost, user-friendliness, ease of installation, compatibility with surrounding systems, and performance were all considered but the deciding factor was performance. Both inflation valves and Schrader valves are inexpensive and are commercially available for roughly $5 CAD each. Both valves are user-friendly and only require a special fitting to connect to the valve to add or remove fluid. However, the Schrader

valve might be slightly easier to use for removing fluid since the inner valve component can be removed if need. The installation of the inflation valve was thought to perhaps be less difficult than that of a threaded Schrader valve and perhaps just as difficult as that for a rubber sealed Schrader valve. This is because threads need to be cut in the additional hole for the threaded Schrader valve while only adhesives are required for the inflation valve and rubber sealed Schrader valve. Despite this, the threaded Schrader valve was more favourable when considering its compatibility with the surrounding systems and its overall performance. The threaded valve could be inserted such that its edge is flush with the inner surface of the skull and therefore does not interfere or come into contact with the brain at all. The other valve options would require that the seal be within the cranial vault. The inflation valve stem would extend into the cranial vault and press into the brain while the rubber seal on the alternative Schrader valve – although nearly flush with the skull – may still affect the brain kinematics and kinetics during impact experiments. In addition to this compatibility with the skull, the sealing mechanism of the Schrader valve was believed to be more effective and durable than the stem of the inflation valve since, over time and repeated use, the rubber material was expected to lose its stiffness faster than the metal components in the Schrader valve.

Once selected, two 1/8” NPT Schrader valves were installed into the BIPED on the inferior side of the skull, posterior to the mounting location for the nodding block and adjacent to the central port for the pressure sensor wires. In this location, the valves would still be easily accessible while not interfering with the surrogate scalp. They were sealed with Dow 732 silicone sealant. Two valves were used so that one could be left open (by removing the valve component) during the filling process. Figure 2-4 shows the installation locations.

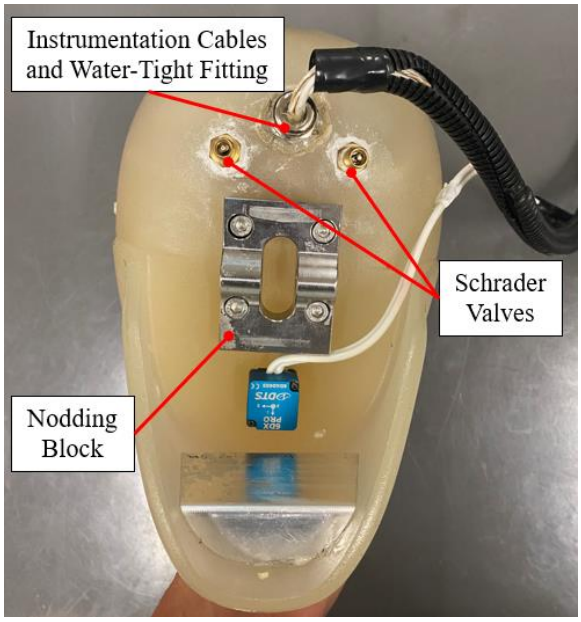

Figure 2-4: Threaded Schrader valves were installed on the inferior side of the skull, posterior to the nodding block but anterior to the instrumentation water-tight fitting. The valves are used to add and remove water or CSF-simulant from the BIPED Mk.2.

2.2 Construction and Use of a Custom Filling Tool

To accompany the Schrader valves on the BIPED Mk 2, a custom fill-tool was assembled, with off-the-shelf components, to facilitate pressurizing the intra-cranium. The tool is shown in **Figure 2-5**. It features a sealing ball valve connected to a tee fitting that feeds into a Schrader connector that threads onto a Schrader valve, and a Bourdon gauge that measures pressure from 0 to 15 inH_2O (~3.7 kPa). A hose lead is connected to the other end of the ball valve where a syringe can be attached to provide the water. With this tool, the internal pressure of the BIPED can be controlled through the addition or removal of water until the desired pressure is reached as indicated on the gauge. Once the desired pressure is reached, closing the ball valve will seal off the measurement zone shown in Figure 2-5**,** whose pressure is equivalent to that within the BIPED, and the BIPED can be sealed at this pressure by disengaging the Schrader valve core. The detailed filling procedure is described below.

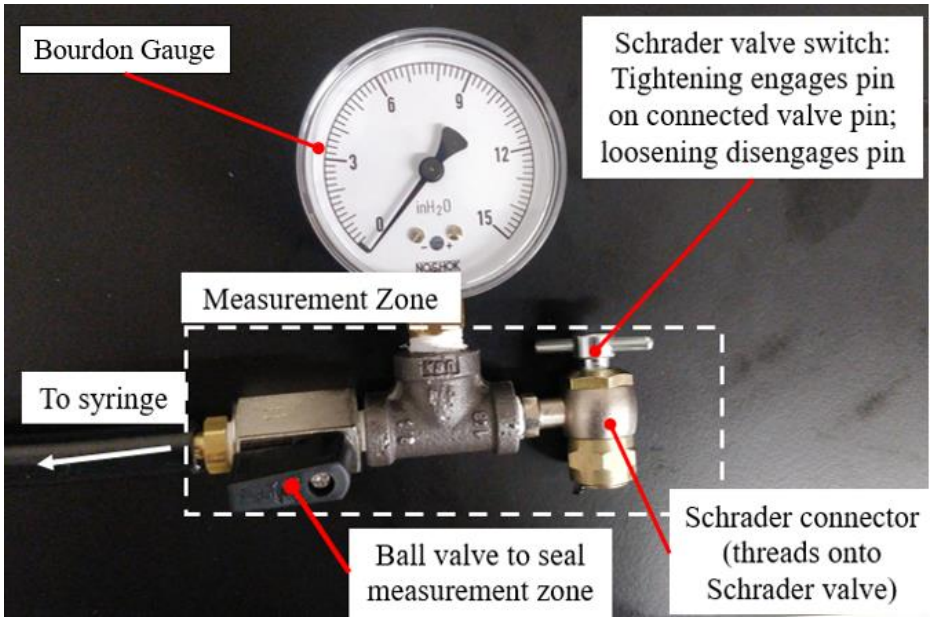

Figure 2-5: Custom fill tool used to pressurize the modified BIPED Mk. 2 by interfacing with the Schrader valves.

The following filling procedure is described with an earlier modified version of the BIPED Mk. 2 with Schrader valves installed in each of the eye slots, and one on the inferior side of the skull, each sealed with Dow 732 silicone sealant as shown in Figure 2-6. The same procedure can be used for the updated modified BIPED shown in Figure 2-4. To initially fill the BIPED, a water source, a vacuum pump, and a method by which to connect these to the Schrader valves are required. Here, a 100 mL syringe with female Schrader coupler was used for the water source while a manual brake pump was used as the vacuum pump.

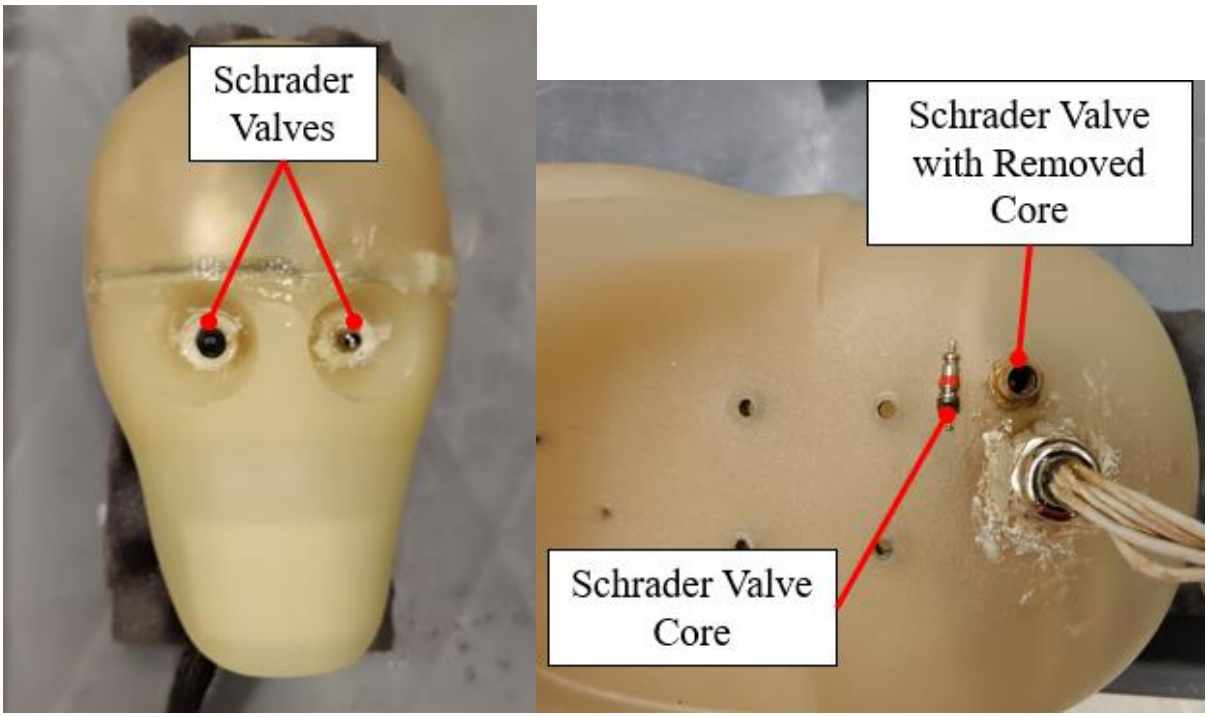

Figure 2-6: Early version of the modified BIPED Mk.2 with Schrader valves installed in the eye slots and one valve on the inferior side of the skull.

1. Designate one Schrader valve as the inlet and the other as the outlet. Here, the left eye valve and the inferior valve are chosen as the inlet and outlet valves, respectively, as shown in Figure 2-7a. Remove the inner valve core from both the inlet and the outlet valves to allow for easier flow for initial filling.
2. Position the BIPED as shown in Figure 2-7b. Attach the water source to the inlet valve and the vacuum pump to the outlet valve. Ensuring a proper seal on both valves, use the vacuum pump to draw water from the water source into the BIPED while simultaneously removing air. Once the BIPED is filled and no air pockets remain in the intracranium, detach the vacuum pump and water source, and replace the valve cores.
3. Attach the syringe to the custom fill-tool. Open the ball valve and ensure the Schrader valve switch on the Schrader connector is fully disengaged (spun counterclockwise to its limit). Prime the fill-tool by depressing the syringe until some water flows out of the Schrader connector.
4. Lay the BIPED on its side as shown in Figure 2-7c and attach the custom fill-tool to the outlet valve by threading the Schrader connector onto the valve. The custom fill-

tool may be attached to any preferred valve at this point. The outlet valve was chosen here since it was the most accessible.

5. Engage the Schrader valve core by spinning the connector switch clockwise. Water is now able to flow from the syringe into the BIPED. Using the syringe, slowly add/remove water to the BIPED until the Bourdon gauge reads 2 inH_2O *greater* than the desired pressure setting. Do not exceed the limit of the Bourdon gauge. Once the gauge reading is steady, close the ball valve to ensure no more water is added or removed from the system. Next, disengage the Schrader valve core by spinning the connector switch counterclockwise. The reading on the gauge will decrease by approximately 2 inH_2O. Once the valve core is fully disengaged, the BIPED is sealed at the pressure indicated by the gauge. The custom fill-tool may now be removed.
6. To check the pressure of the BIPED after having already disconnected the custom fill-tool, start by repeating steps 3 and 4. Then before engaging the valve core, pressurize the measurement zone to the last recorded pressure before the custom fill-tool was removed. Once the measurement zone is pressurized, close the ball valve and engage the valve core. If the BIPED maintained its pressure between instances of connecting the custom fill-tool, the reading on the gauge should be approximately 2 inH_2O higher than the desired set point.

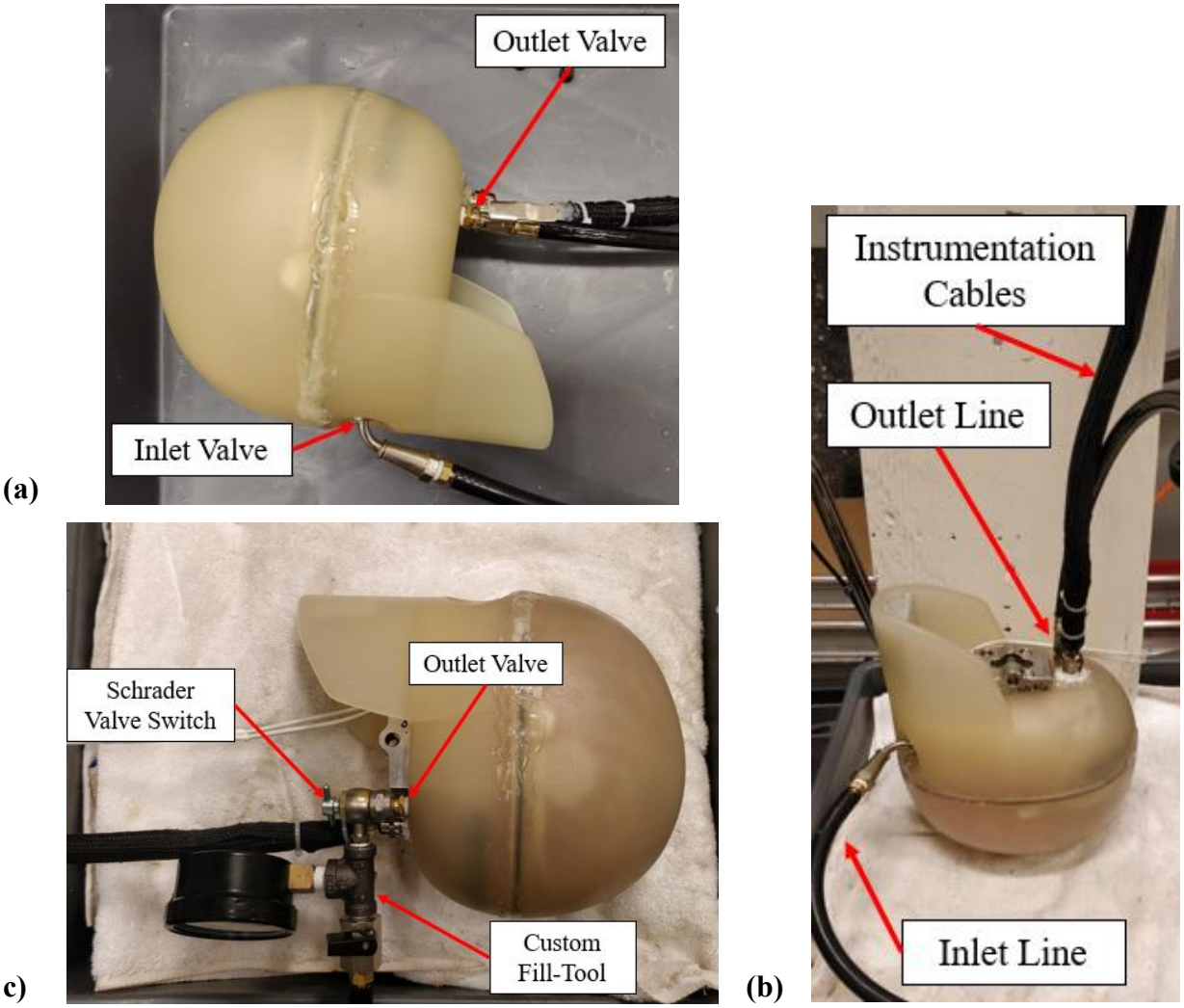

Figure 2-7: (a) The Schrader valve in the left eye socket was selected as the inlet valve while the inferior Schrader valve was used as the outlet valve. Together they were used to fill and pressurize the BIPED. (b) Two hoses were connected to the inlet and outlet valves. The inlet line leads to a water source (a syringe) and the outlet line leads to a vacuum pump (manual brake pump). (c) After disconnecting the inlet line and closing the inlet valve, the custom fill-tool was connected to the outlet valve to pressurize the BIPED.

2.3 Addition of Pressure Sensors

Measuring intracranial responses to blunt impacts in surrogate headforms, requires low-profile instrumentation. Previous researchers have used and/or developed suitable instrumentation for the task. Older solutions, especially those for cadaver models, used externally mounted transcranial pressure transducers to reach the inner surface of the skull [25], [56]. Newer solutions for surrogate head models employ sensors with a very small footprint (<3 mm diameter) mounted flush with the inner surface of the skull itself [13], [18], [23]. In the work presented here, the latter method is

mimicked to instrument the modified BIPED Mk. 2 with pressure transducers capable of measuring intracranial pressures at locations comparable to that in Nahum and Smith [26]. Li et al. prototyped this method for the BIPED Mk. 1 shown in Figure 2-8. Although the BIPED is now capable of measuring ICPs, the sensor cables were fed through the posterior region of the skull. Here, they interfere with the surrogate scalp and obstruct any posterior impact tests. For the BIPED Mk. 2 modifications, the cables for the additional pressure sensors were instead fed through the existing instrumentation port located on the inferior side of the skull (Figure 2-4).

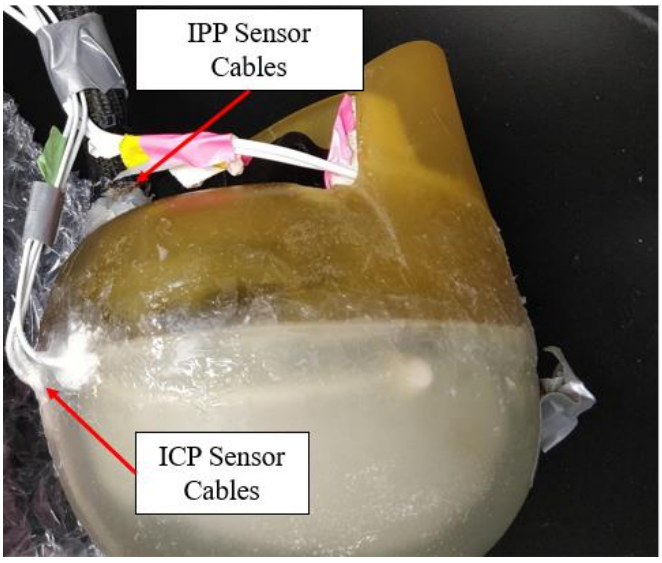

Figure 2-8: BIPED Mk. 1 modified to have ICP sensors installed on the inner surface of the skull. The ICP sensor cables were fed to the posterior of the headform.

To install the ICP sensors (MS5407, TE Connectivity Ltd, CA USA), a 3 mm deep recess was drilled into the surface of the skull using a custom drill guide that was previously used by Azar et al. and Li et al. [18], [23]. The guide is shown in **Figure 2-9a.** The guide was originally designed such that each sensor would be positioned 58.2 mm above the Frankfort plane. After creating the recesses, the pressure sensors were installed with Dow 732 silicone sealant such that any exposed electronics were sealed as shown in **Figure 2-9b.** The cables were then adhered to the inner surface of the skull, with cyanoacrylate, such that their paths took the most direct route to the instrumentation cable port (**Figure 2-4**).

(a)

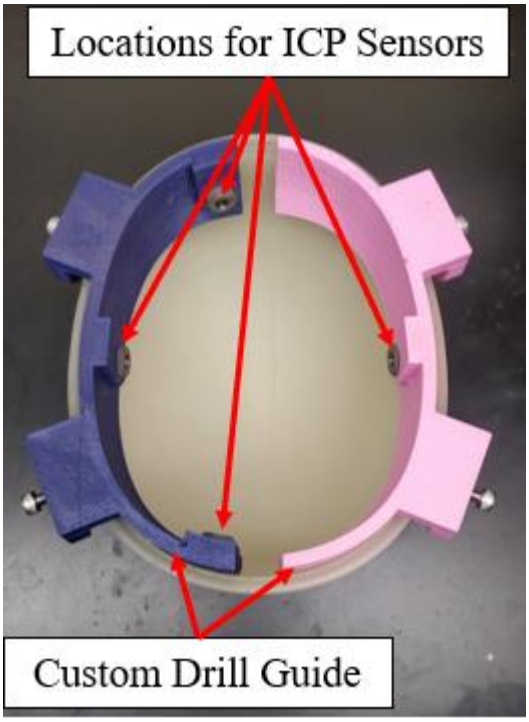

(b)

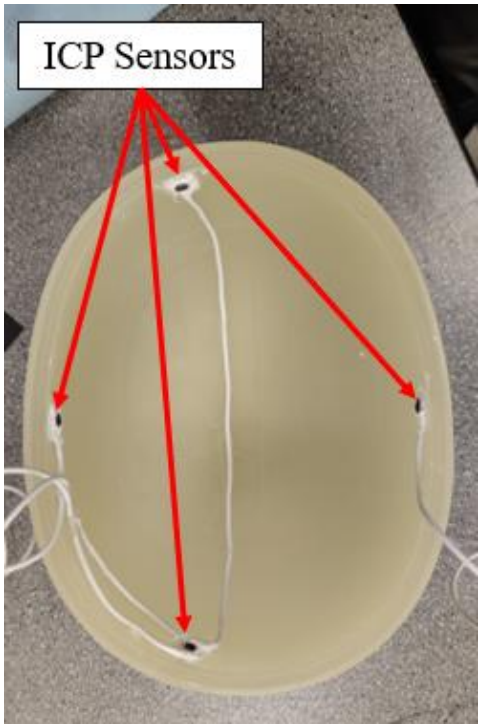

Figure 2-9: (a) The superior half of the BIPED skull with the custom drill guide attached. The guide assists in drilling out four recesses in which a miniature pressure sensor can be mounted. (b) Four pressure sensors mounted to the superior portion of the BIPED skull. The sensors were adhered with Dow 732 silicone sealant.

2.4 Summary

To perform the experiments described in the next chapter that investigate the effect of changing the resting ICP of the BIPED, some modifications were required. First, a set of valves that enabled and maintained headform pressurization were selected and installed into the inferior aspect of the BIPED skull. A custom fill-tool was constructed to interface with these valves to fill and pressurize the BIPED up to 13 inH_2O. Next, to measure the CSF-layer ICP, miniature pressure sensors were added to the inner surface of the BIPED skull. These additional sensors record pressure data that may now contribute to the already available information that is collected regarding the distribution and development of the transient pressure wave.

Following the modifications that were made to the BIPED Mk. 2 described above and following the experiments throughout the course of this work, there are two key recommendations to be noted regarding these modifications. First, only two Schrader valves are required for filling/draining the BIPED and they should be installed in an easily accessible location like the one

shown in **Figure 2-4**. This way, the scalp need not be removed to pressurize the BIPED. Secondly, either embedding the ICP sensors and their cables in the skull itself during fabrication or adding grooves to the existing mold to accommodate the sensors and their cables would drastically reduce assembly time and inconsistencies that may arise from sensor placement.

Chapter 3: Pendulum Impact Experiment with a Modified Surrogate Headform

This chapter describes the pendulum impact experiment, starting with an explanation of the Brain Injury Protection Evaluation Device (BIPED) instrumentation, the setup of the pendulum impact, how measurements were recorded and processed, and the experimental design and analysis methods. The experiment was first conducted with the Hybrid III headform to obtain preliminary kinematic results. Once these results were verified to not be beyond the estimated limits of the BIPED, the experiments continued with the BIPED.

3.1 BIPED Instrumentation Overview

The effects of changing the resting ICP of a head model were explored with the Brain Injury Protection Evaluation Device (BIPED) surrogate headform developed by Defense Research and Development Canada, Valcartier Research Centre (DRDC – VRC). The second version dubbed the BIPED Mk. 2, shown in Figure 3-1, features a two-part skull meant to encase a surrogate brain, the falx and tentorium membranes, and a cerebrospinal fluid (CSF) simulant layer [16]. The top and bottom halves of the skull are then sealed with an o-ring and with a urethane adhesive (AP-2220 Armor-Bond SEMI-FLEX, BJB Materials, CA USA). The inferior side of the BIPED Mk. 2 possess a nodding block to attach to a surrogate neck and features a counterbalance meant to improve the biofidelity of the headform's moment of inertia (compared to the BIPED Mk 1) by relocating the center of mass. The particular BIPED used for this paper was then modified to control and set the resting ICP as described in Chapter 2. A pair of Schrader valves were installed in the inferior side of the basilar skull, posterior to the nodding joint (Figure 3-1). This allowed for the use of a custom fill-tool with an isolating valve and a bourdon pressure gauge to fill and set the resting ICP of the headform when positioned supine.

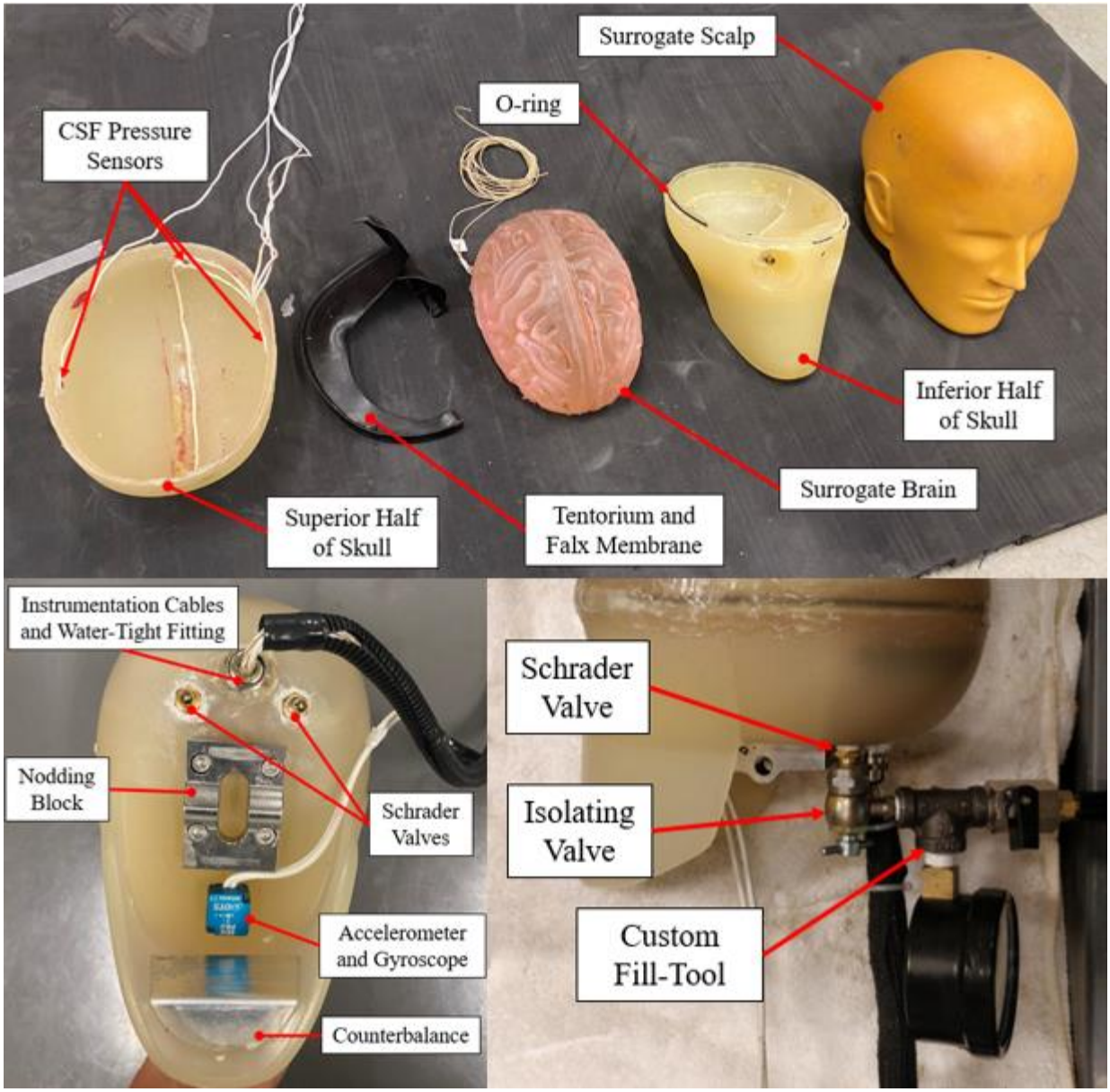

Figure 3-1: Components and instrumentation of the BIPED Mk. 2 and the custom fill-tool used to pressurize the intracranium.

The surrogate brain, shown in the x-ray image in Figure 3-2, is molded around two pressure sensors (XCL-072, Kulite Semiconductor Products, NJ USA) that capture front and back intraparenchymal pressure responses. Three additional pressure sensors (MS5407, TE Connectivity Ltd, CA USA) are embedded into the skull such that the sensing diaphragms are flush with the inner surface of the skull and thus could capture the ICP responses in the CSF layer. A fourth pressure sensor was installed at the posterior inner surface of the skull, but data were not collected from it due to a malfunction with the installation. Finally, a DTS 6DX sensor (DTS 6DX

PRO, DTS Inc, CA USA) is mounted underneath the chin to measure global head linear accelerations and angular velocities.

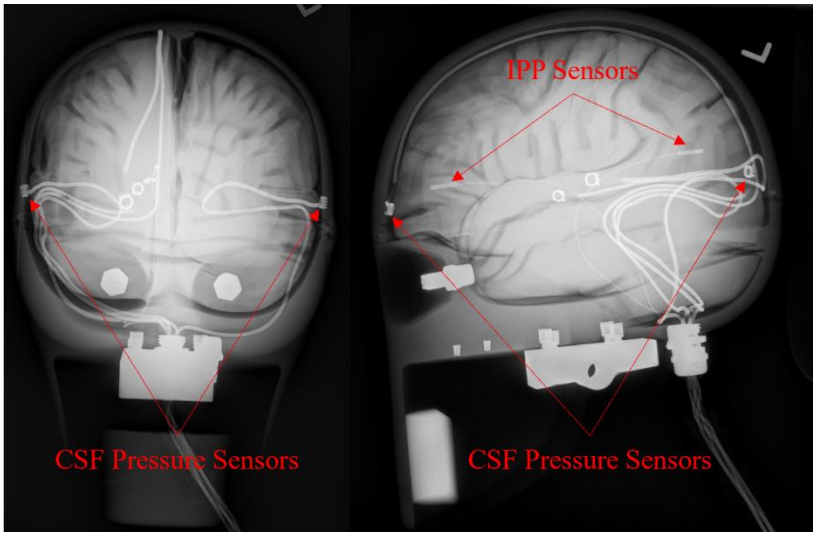

Figure 3-2: Anteroposterior and lateral x-ray images depicting locations of pressure sensors.

3.2 Pendulum Impact Setup

To conduct the current study, a pendulum impactor was selected to deliver the blunt impact to the headforms. Pendulum impact experiments not only offer a high degree of repeatability, but they can also closely simulate realistic impact events where the head is rapidly loaded from a horizontally directed impact. Moreover, the degree of impact can be controlled by the release height of the pendulum as well as its mass – this is an additional control parameter over the drop tower experiment. In addition to its practicality, a pendulum experiment was selected given the precedent set by Li et al. [18] for comparing the BIPED to cadaver data sets where the cadaver experiments featured stationary head models subjected to blunt impacts from an accelerated mass.

The pendulum impact experiment presented here follows the setup described in Li et al [18], which is based on Nahum and Smith [26], save for the substitution of a full body 50th percentile male Hybrid III surrogate for the neck gimbal and rail system. After attaching the desired headform, the surrogate was seated in a chair with backing foam that assisted in tilting the torso forward such that the headform's Frankfurt plane was at an angle of 45 degrees relative to the line of impact as shown in Figure 3-3. The pendulum was raised to predetermined heights such that it would impact the forehead of the selected headform with 18.8, 37.7, and 65.9 J of energy. These

energies were selected after determining that the 65.9 J impact would yield peak impact forces similar to that of Nahum and Smith [26]. This was set as the upper bound to not risk structurally damaging the BIPED before the completion of the experimental series. The lower two energy levels were selected to loosely represent head impacts of a 10 kg object striking the head between 2 and 3 m/s. Impact force was measured with a PCB C03 force transducer (PCB 208C05, PCB Piezotronics Inc., New York) mounted to the pendulum ram in a similar manner to the impact anvil in Li et al. [16].

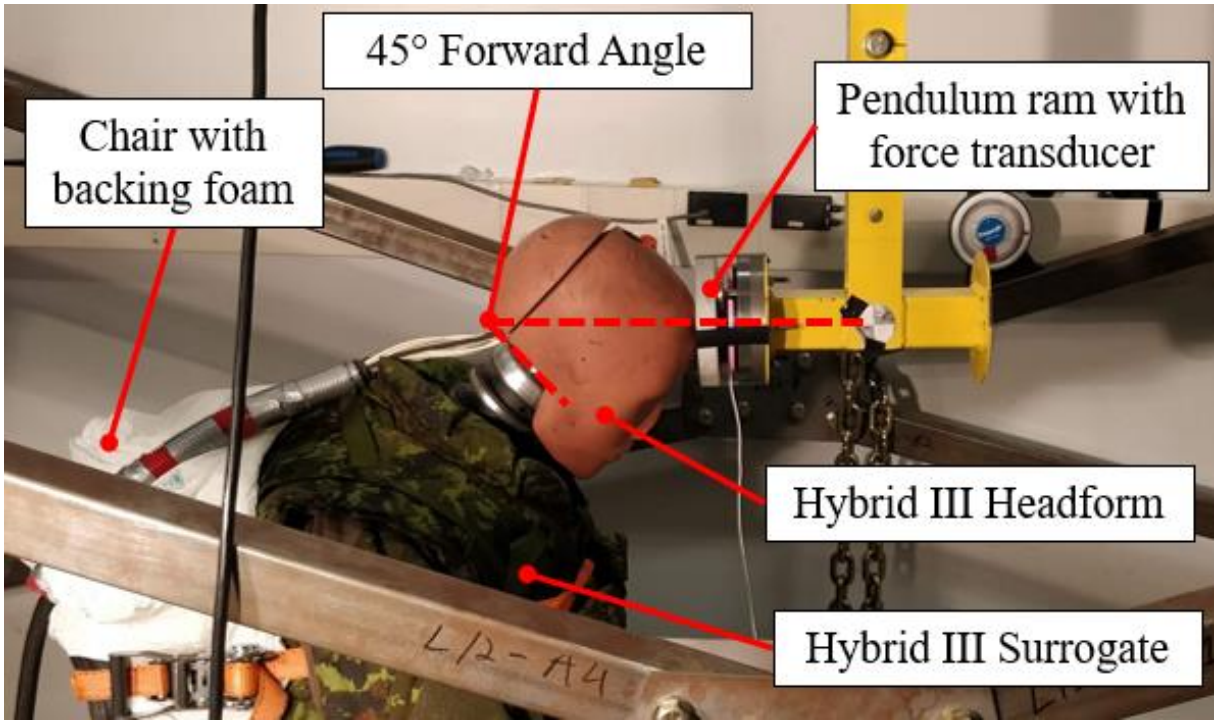

Figure 3-3: Pendulum impact experimental setup where a seated Hybrid III full body surrogate with its headform angled forward at 45° forward is subjected to a blunt impact. The force of impact is measured by a force transducer located in the ram of the pendulum. This setup was replicated after substituting the Hybrid III headform for the BIPED Mk. 2 headform.

Data were recorded following the coordinate system shown in **Figure 3-4**.

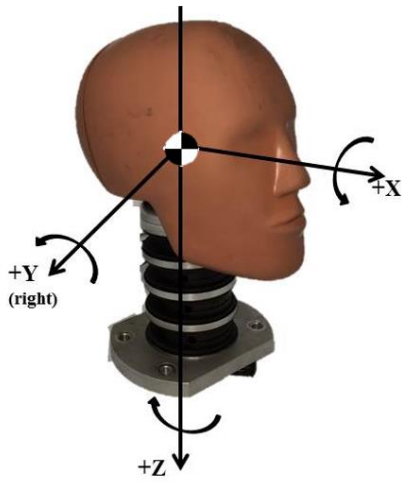

Figure 3-4: Headform coordinate system applied to recorded data. The *x*-axis represents the anterior-posterior axis, the *y*-axis represents the medial-lateral axis, and the *z*-represents the longitudinal axis. The positive directions are indicated by the arrow heads.

3.3 Data Acquisition and Post Processing

Data were collected at 25 kHz and using National Instruments hardware and software (PXI 6251 and LabVIEW 2020, Austin TX). A hardware anti-aliasing filter with a cutoff frequency of 4 kHz was used to filter the acceleration and pressure analog signals. A fourth-order digital Butterworth filter was used to filter signals from all sensors. In the case of the BIPED, angular velocities were filtered with a cutoff frequency of 300 Hz, while the pressure signals were filtered at 1650 Hz according to the j211 standard [57]. For both headforms, the acceleration and impact force signals were filtered with a cutoff frequency of 1650 Hz, following the j211 standard as well [57]. Specifically for the BIPED, accelerations at the sensor's location were then transformed to the head center of gravity with the following vector (obtained from a full 3D CAD model of the BIPED Mk. 2) and relative acceleration equation:

$$\vec{r}_{\mathrm{CoG/DTS}} = \langle -60.5, 0, -62.2 \rangle \cdot 10^{-3}\ \mathrm{m} \quad \textbf{(1)}$$

$$\vec{a}_{\mathrm{CoG}} = \vec{a}_{\mathrm{DTS}} + \vec{\alpha} \times \vec{r}_{\mathrm{CoG/DTS}} - \vec{\omega} \times (\vec{\omega} \times \vec{r}_{\mathrm{CoG/DTS}}) \quad \textbf{(2)}$$

where $\vec{r}_{\mathrm{CoG/DTS}}$ denotes the relative distance from the DTS sensor location to the head center of gravity (CoG), $\vec{a}_{\mathrm{CoG}}$ is the acceleration vector at the head CoG, $\vec{a}_{\mathrm{DTS}}$ is the acceleration vector at the DTS sensor, and $\vec{\alpha}$ and $\vec{\omega}$ denote the angular acceleration and velocity vectors of the head

respectively. The angular acceleration is obtained from cumulative trapezoidal integration of the angular velocity signal.

For the Hybrid III headform, acceleration signals from each of the nine accelerometers (Measurement Specialties Inc. Hampton VA, model 64C-2000-360) were transformed to provide both linear and angular global head kinematics [58].

3.4 Experimental Design and Methods of Analysis

Pilot experiments were first conducted with the Hybrid III headform. Again, it was struck on the forehead with 18.8, 37.7, and 65.9 J of energy, with five repetitions at each level in total. For the main experimental tests, the BIPED MK. 2 was impacted at each of the same energy levels after setting the resting ICP to 0, 3, 6, and 9 inH_2O gauge (0, 5.6, 11.2, and 16.8 mmHg or 0, 0.75, 1.5, 2.24 kPa). These resting ICP parameters were selected to span the anatomic range of 7-15 mmHg reported in section 1.2 This is a total of 15 impacts with the Hybrid III and 60 impacts with the BIPED.

The average peak kinematic and pressure responses from the impacts were grouped by impact energy and by resting ICP. Within each impact energy level, all BIPED configurations were then compared to each other and tested for statistical differences using student's *t*-test ($n = 5$ for each group) assuming unequal variances. For this multiple comparison, a significance level of 0.05 was chosen and then corrected to 0.008 according to the Bonferroni method when six comparisons are made. A statistical comparison of the peak global head linear accelerations and the peak impact forces between Hybrid III impacts and BIPED impacts was not performed since the Hybrid III only served as a representation of the current industry standard headform.

Chapter 4: Kinematic and Pressure Response of a Modified Surrogate Headform with Varying Resting ICPs Subjected to Pendulum Blunt Impacts

Chapter 4 presents the results of the experiments described in Chapter 3. A sample of the time series data is shown along with bar graphs of the key peak kinematics and pressure responses. The peak kinematics were compared using statistical methods and then effect sizes were tabulated.

4.1 Results of Blunt Impact Experiment

All of the experimental kinematic and pressure responses are characteristic of blunt impacts directed to the forehead: acceleration histories shown in Figure 4-1 show a rapid acceleration phase in the *x*- and *z*-components (anterior-posterior and longitudinal axes of the head respectively) followed by a deceleration phase; head rotation was predominantly about the *y*-axis (medial-lateral axis); impact force, recorded at the pendulum, rose and peaked in unison with head accelerations. Additionally, while the anterior (front) IPP and anterior (front) CSF-layer ICP rose to a positive maximum pressure, the posterior (back) IPP exhibited an initial corresponding drop in pressure followed by a rise in pressure prior to settling. Pressure histories at the left and right CSF-layer were nearly identical in magnitude across the entire window for the given impact event.

The smaller peaks that follow the initial impact force peak did not contribute to the head kinematics. They are attributable to the vibrations of the aluminium plate, that is part of the pendulum assembly, which transmits the force from the impact to the sensor itself.

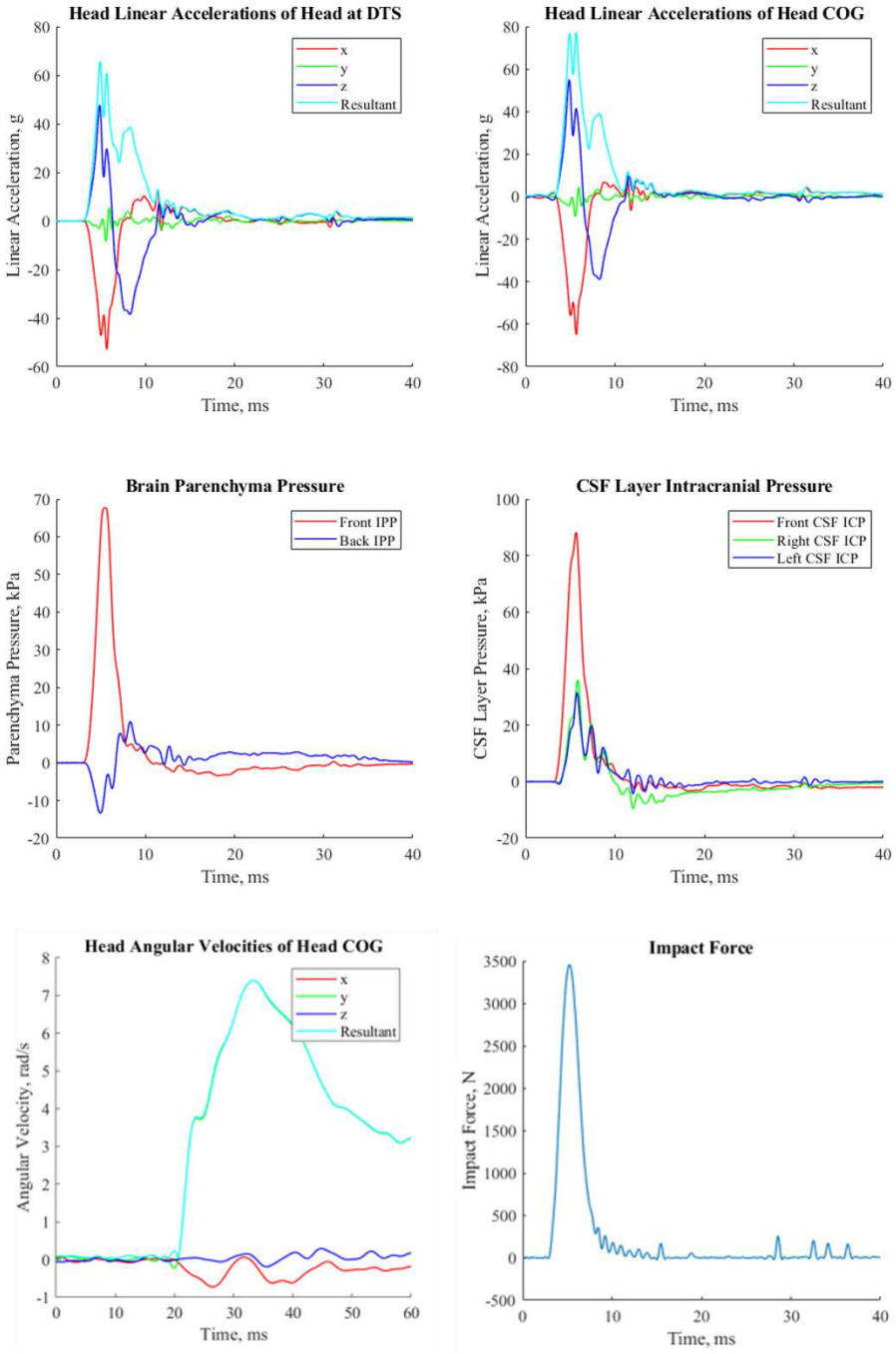

Figure 4-1: Time series traces of global head kinematics, intraparenchyma pressures, CSF-layer intracranial pressures, and impact force measured at the pendulum.

The average peak resultant head linear accelerations of each BIPED ICP configuration remained consistently within 3% of other configurations within each of the different impact energy levels. Figure 4-2a. shows that at 18.8 J impacts, the BIPED's average peak head accelerations

ranged from 79.0 to 80.6g (where g is the gravitational acceleration constant of 9.81 m/s^2). At 37.7 J, average peak accelerations ranged from 144.4 to 148.8g while the range for 65.9 J impacts was from 182.4 to 184.7g. The Hybrid III's average peak head linear accelerations were 97.0, 150.5, and 214.2g for 18.8, 37.7, and 65.9 J impacts, respectively. These accelerations are higher than the BIPED at each energy level. Comparison tests revealed that at 18.8 J of impact energy, peak accelerations between the 6 and 9 inH_2O resting ICP configurations were significantly different. At 37.7 J of impact energy, significant differences were observed between the 0 and 3, 0 and 6, 3 and 6, 3 and 9, and the 6 and 9 inH_2O resting ICP configurations. Lastly, no significant differences between resting ICP configurations for the impacts at 65.9 J. Significant differences are indicated with an asterisk (p-value < 0.008). The difference is between the groups at either end of each of the horizontal black lines in Figure 4-2.

Figure 4-2b. depicts a similar trend in consistency for the average peak force between each BIPED configuration. For impacts 18.8, 37.7, and 65.9 J of energy, the average peak impact force ranged from 3.4-3.5 kN, 5.9-6.3 kN, and 7.8-7.9 kN, respectively. The average peak impact force with the Hybrid III was again higher than the BIPED for each impact scenario. The impact forces applied to the Hybrid III were 4.7, 7.0, and 9.4 kN for impacts at 18.8, 37.7, and 65.9 J. Significant differences in the peak impact forces were found between the 0 and 3, 0 and 6, 0 and 9, and the 3 and 9 inH_2O resting ICP configurations at the 18.8 J impact energy level. For impacts at 37.7 J, significant differences were observed between the 0 inH_2O resting ICP configuration and all other resting ICP configurations while the only significant difference noted for 65.9 J impacts was between the 0 and 6 resting ICP configurations. Again, significant differences are indicated with an asterisk (p-value < 0.008).

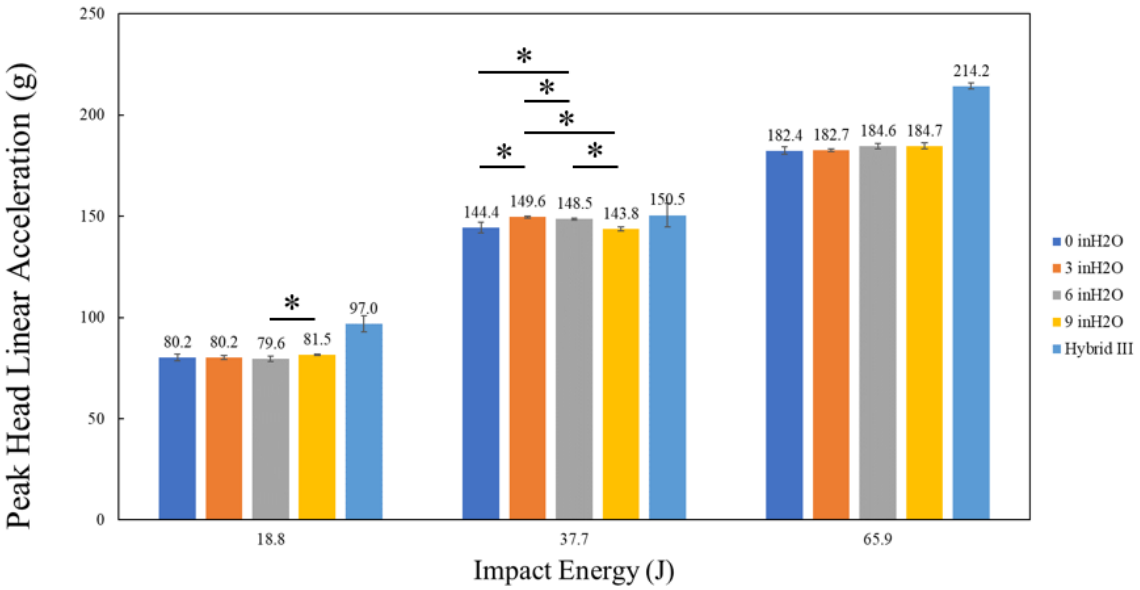

(a)

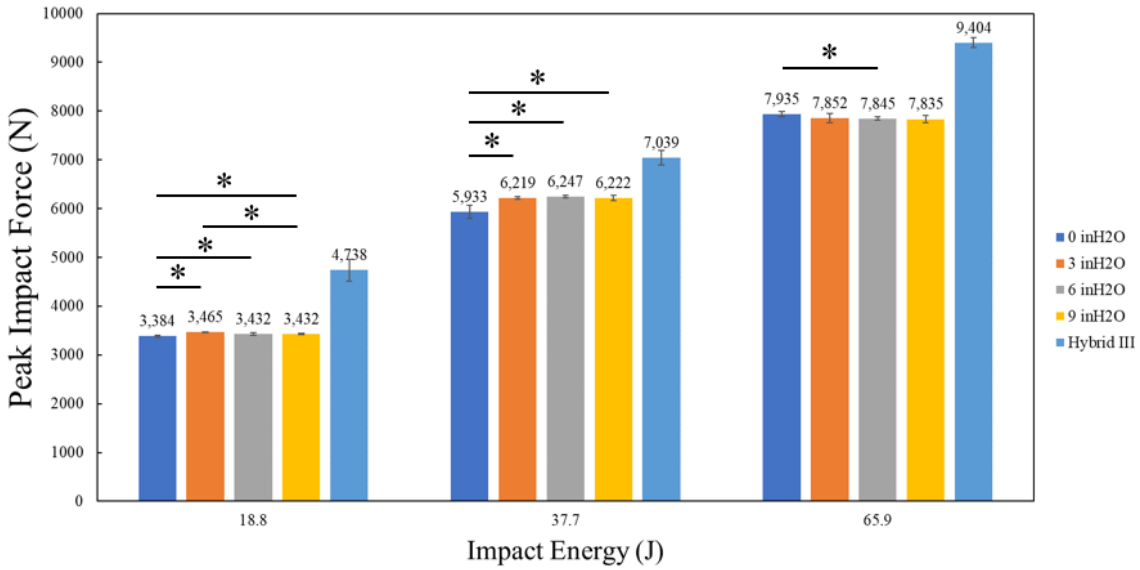

(b)

Figure 4-2: Average peak head linear accelerations (a) and peak impact forces (b) of the Hybrid III headform and the BIPED headform pressurized to 0, 3, 6, and 9 inH_2O-gauge. Error bars indicate one standard error assuming a t-distribution with α=0.008 and v=4. An asterisk (*) indicates a significant difference between the groups at the ends of the horizontal line (p-value <0.008, n=5). Comparison tests were only performed for BIPED configurations.

For each of the BIPED configurations, the average maximum intracranial and intraparenchymal pressures at the front of the headform, as well as the average maximum and minimum intraparenchymal pressures at the back of the headform were graphed in Figure 4-3 and Figure 4-5. Much like the average peak linear head accelerations, the frontal ICP and IPPs were

consistent across BIPED resting ICP configurations. At each impact energy level, the average peak front ICP for BIPED configurations with non-zero resting ICP deviated by as much as 4% from the 0-gauge resting ICP configuration. Likewise, the average peak front IPP deviated by as much as 4% between the non-zero and 0 gauge resting ICP configurations for each impact energy level. At both the 18.8 and 37.7 J impact energy levels, the 0 and 9, and the 3 and 9 inH_2O-gauge resting ICP configurations exhibited significant differences in peak front ICP. A significant difference was also observed in the peak front ICP between the 6 and 9 inH_2O-gauge resting ICP configurations for 37.7 J impacts. No significant differences were found at the 65.9 J impact level. For maximum front IPP, at the 18.8 J impact energy level, significant differences were only observed between the 0 and 9 inH_2O-gauge configurations. For the 37.7 J impacts, there were significant differences in maximum front IPP between the 0 and 9, 3 and 9, and 6 and 9 inH_2O-gauge configurations. Again, no differences were observed for 65.9 J impacts. Significant differences are indicated with an asterisk (p-value < 0.008) in Figure 4-3.

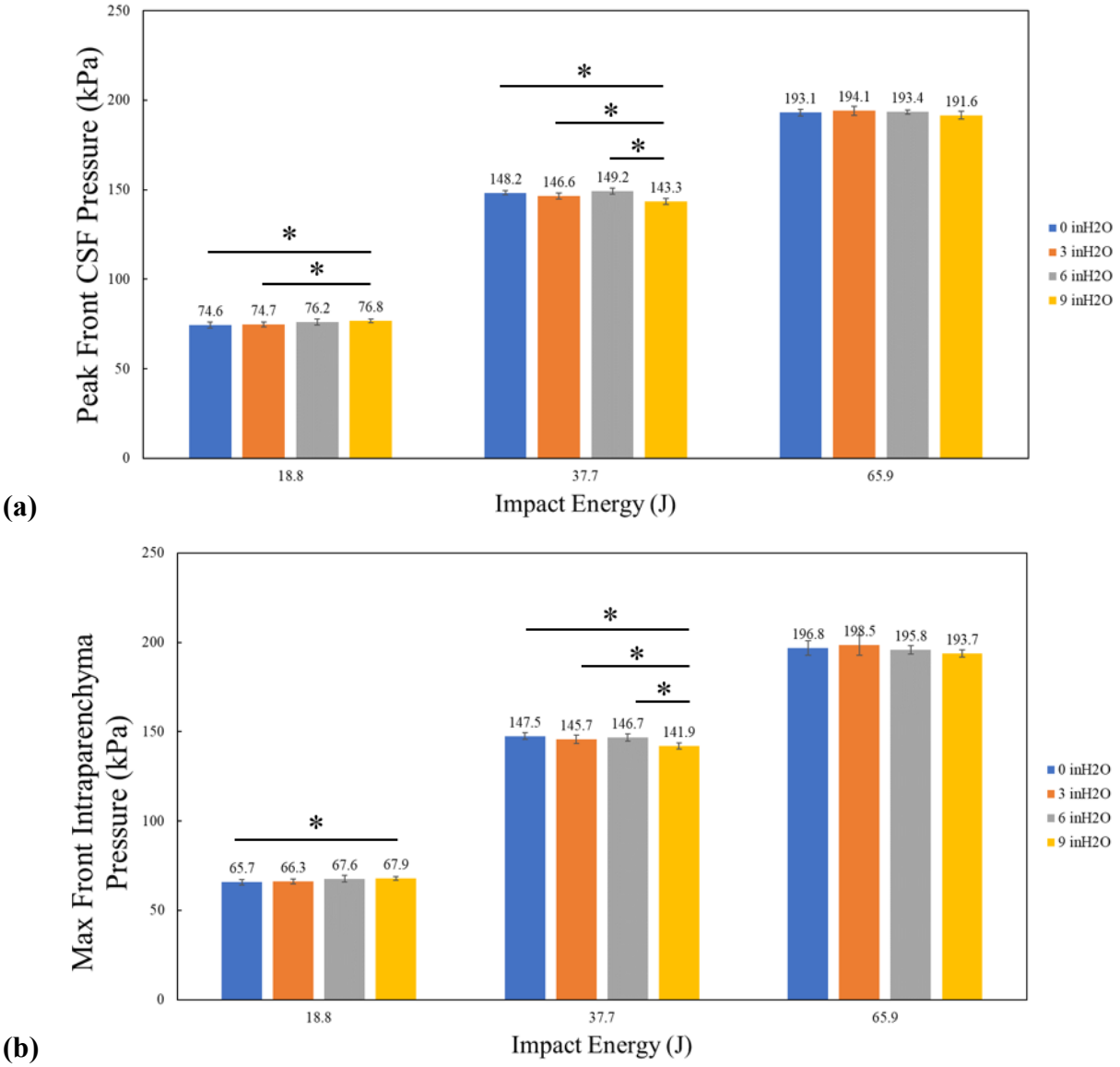

Figure 4-3: Average peak intracranial (a) and intraparenchymal (b) pressures measured at the front of the BIPED when pressurized to 0, 3, 6, and 9 inH_2O-gauge. Error bars indicate one standard error assuming a t-distribution with α=0.05 and ν=4. An asterisk (*) indicates a significant difference between the groups at the ends of the horizontal line (p-value <0.008, n=5).

The average peak left and right ICPs shown in Figure 4-4 present more variation between resting ICP configurations than the front ICP and IPP signals. At the lowest impact energy level, average peak left and right ICPs for non-zero gauge resting ICP configurations varied as much as 8 and 12%, respectively, from the 0 inH_2O-gauge configuration. For 37.7 J impacts, while increasing the resting ICP, the average peak left and right ICPs gradually increased by 4 and 6%, respectively, from the 0 inH_2O-gauge configuration to 6 inH_2O-gauge configuration. At 9 inH_2O-

gauge resting ICP, both the left and right average peak signals fell to approximately 1 to 2% lower than the average peaks recorded at the 0 inH_2O-gauge configuration. For 65.9 J impacts, while the average peak left ICP rose from 114.1 kPa to 121.0 kPa for increasing resting ICP, the average peak right ICP fell from 123.3 kPa to 110.3 kPa. At the 18.8 J impact energy level, significant differences in the average peak left ICPs were found between the 0 and 6, 0 and 9, 3 and 9, and the 6 and 9 inH_2O-gauge configurations. For the average peak right ICPs, differences were observed between all pairs of resting ICP configurations except for the 0 and 6 inH_2O-gauge configuration pair. At 37.7 J, the only average peak left ICPs that were significantly different from each other were the 6 and 9 inH_2O-gauge configurations. For the right side, differences were found between the 0 and 6, 3 and 6, 3 and 9, and the 6 and 9 inH_2O-gauge configurations. For 65.9 J impacts, the only significant difference observed was between the 0 and 9 inH_2O-gauge configurations for average peak ICPs on the right side.

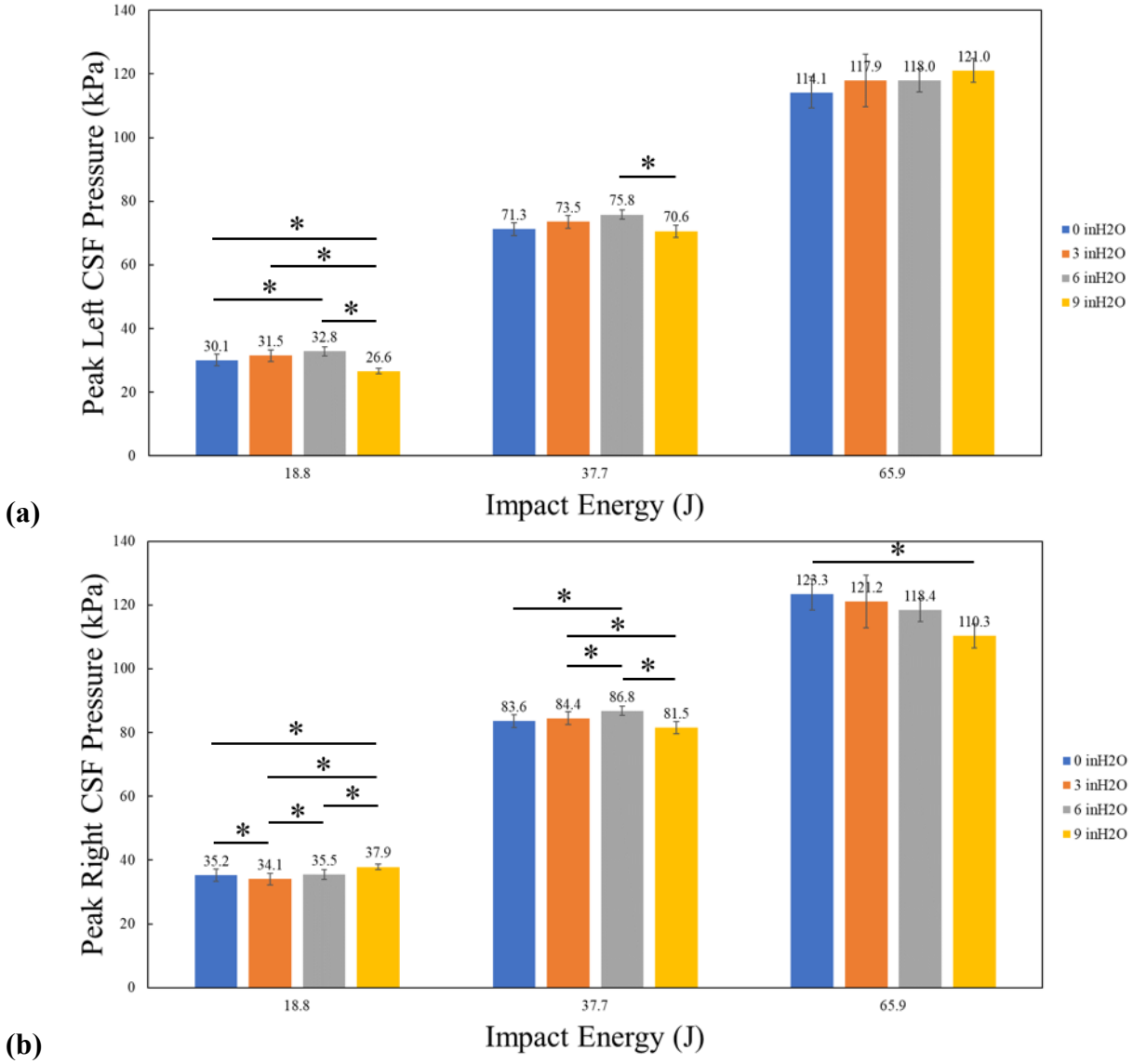

Figure 4-4: Average peak left (a) and right (b) intracranial pressures measured at the back of the the BIPED when pressurized to 0, 3, 6, and 9 inH_2O-gauge. Error bars indicate one standard error assuming a t-distribution with α=0.05 and ν=4. An asterisk (*) indicates a significant difference between the groups at the ends of the horizontal line (p-value <0.008, n=5).

The minimum and maximum back IPP present more variation between the headform configurations as shown in Figure 4-5. At the lowest impact energy level, average maximum and minimum back IPPs for the 3 and 6 inH_2O-gauge configurations deviated by as much as 2% from the 0 inH_2O-gauge headform configuration while a resting ICP of 9 inH_2O-gauge resulted in deviations as much as 8% from the 0 inH_2O-gauge configuration. For 37.7 J impacts, while increasing the resting ICP, the average minimum back IPP initially dropped by about 2 kPa between the 0 and 3 inH_2O-gauge configurations, did not change significantly from 3 and 6 inH_2O-

gauge, and finally increased by about 2 kPa at 9 inH_2O-gauge resting ICP. For 65.9 J impacts, the average minimum back IPP decreased from 19.3 kPa to 18.3 kPa when increasing the resting ICP. The average maximum back IPP increased from 24.6 to 33.1 kPa and 42.4 to 47.3 kPa for impacts of 37.7 and 65.9 J, when increasing the resting ICP. At the 37.7 J impact energy level, the average minimum back IPP for the 3 and 6 inH_2O-gauge configurations were significantly different from the 0 inH_2O-gauge resting ICP while at 65.9 J, only the 9 inH_2O-gauge resting ICP configuration was significantly different. The average maximum back IPP for each of the non-zero resting ICP configurations were all significantly different than the 0 inH_2O-gauge resting ICP for impacts at 37.7 and 65.9 J. For 18.8 J impacts, the average maximum back IPP for the 9 inH_2O-gauge configuration was the only configuration that was significantly different from the 0 inH_2O-gauge resting ICP configuration.

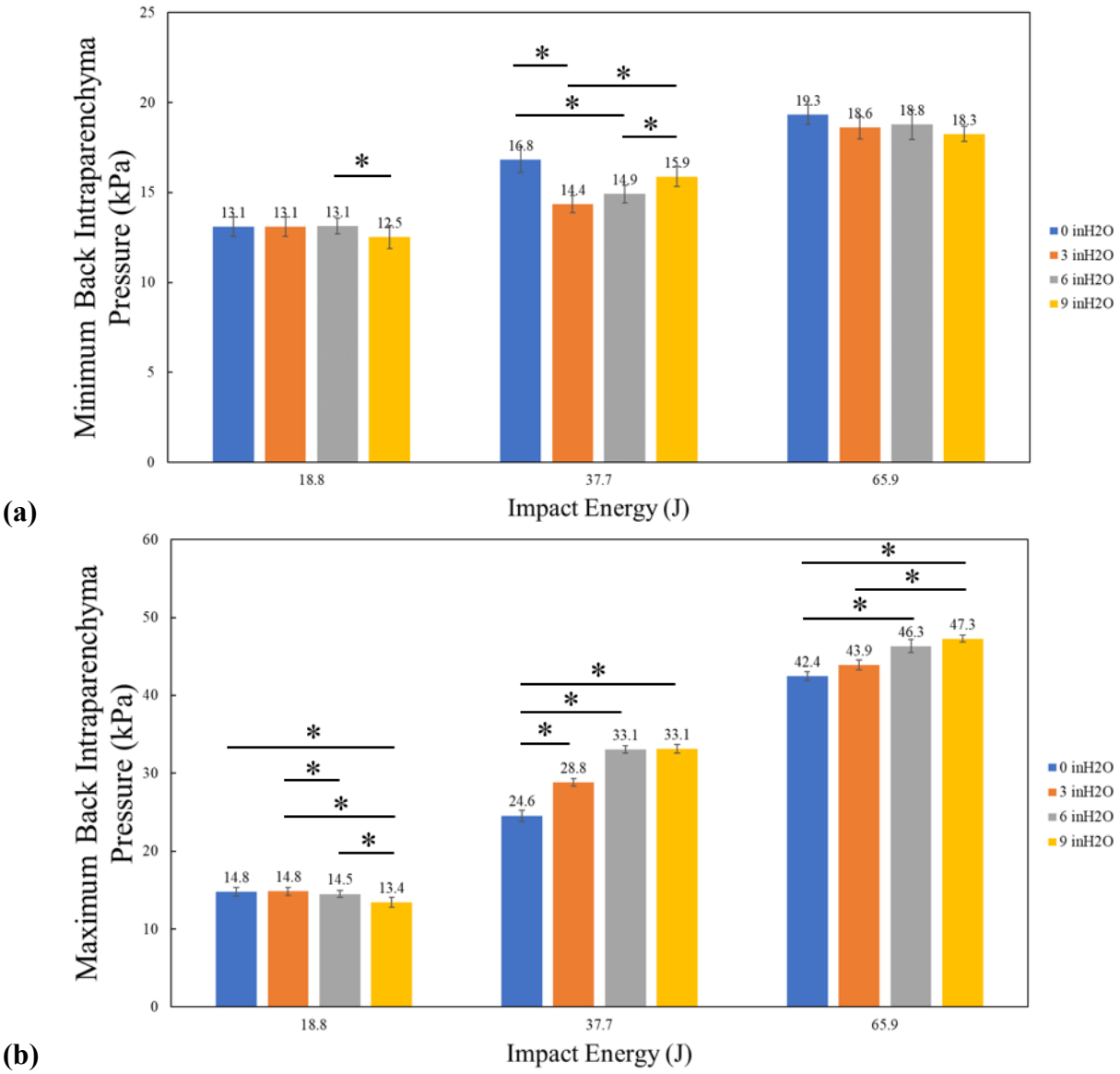

Figure 4-5: Average minimum (a) and maximum (b) intraparenchymal pressures measured at the back of the the BIPED when pressurized to 0, 3, 6, and 9 inH_2O-gauge. Error bars indicate one standard error assuming a t-distribution with α=0.05 and v=4. An asterisk (*) indicates a significant difference between the groups at the ends of the horizontal line (p-value <0.008, n=5).

Lastly, in addition to the kinematic and pressure histories, the time taken for the parenchyma pressure wave to travel from the front IPP sensor to the back IPP sensor was reported. This was calculated by taking the time difference between the respective sensors' maxima. The average times for this pressure wave propagation for each of the experiment configurations are tabulated in Figure 4 4. Overall, as the impact energy increased, the travel time for the wave decreased from as high as 2.36 ms to as low as 1.66 ms. For 18.8 J impacts, the travel times between each BIPED

configuration vary as much as 5%. For both the 37.7 and 65.9 J impacts, the average wave travel time gradually decreases as the resting ICP increases. The travel time decreased as much as 7% for the 37.7 J impacts. However, the only significant differences in travel time were found at the 18.8 and 37.7 J impacts, for the 9 inH2O-gauge configuration.

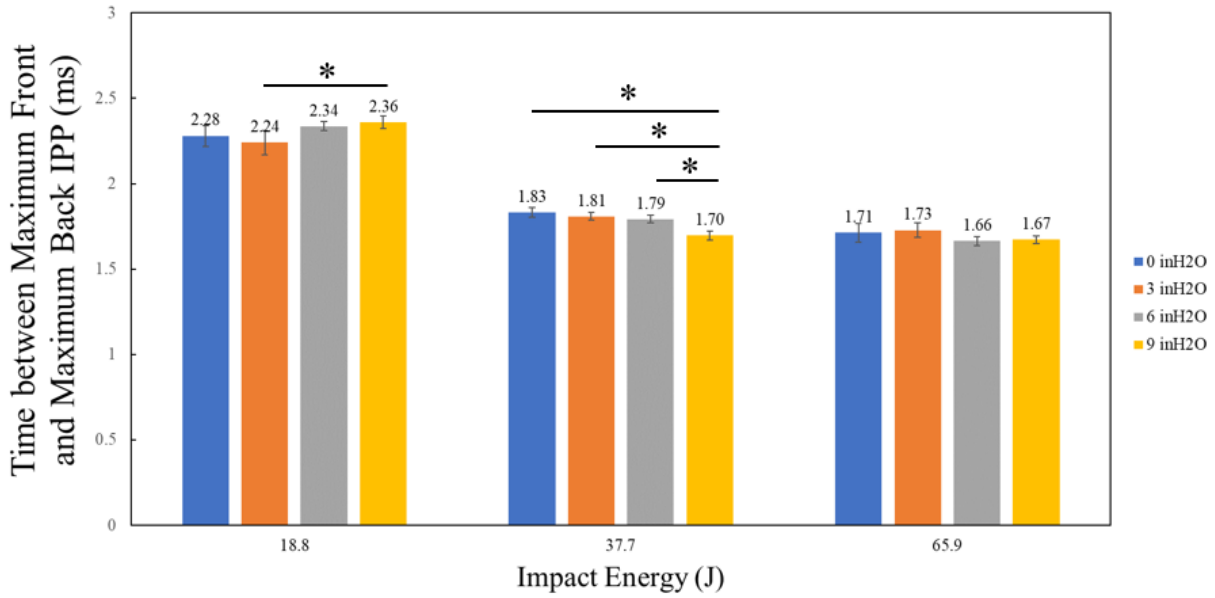

Figure 4-6: Average time taken for the parenchyma pressure wave to travel from the front IPP sensor to the back IPP sensor. Error bars indicate one standard error assuming a t-distribution with α=0.05 and v=4. An asterisk (*) indicates a significant difference from the BIPED pressurized to 0 inH$_2$O-gauge (p-value <0.05, n=5).

A summary of the Cohen's *d* effect sizes, standard deviations (assuming unequal variances), and the percent differences in the means only between the zero and each of the non-zero BIPED resting ICP configurations for each of the metrics, excluding the pressure wave travel time, were tabulated. The summary for the 18.8 J impacts is shown in Table 4-1 while the summaries for the 37.7 J impacts, and the 65.9 J impacts are shown in Table 4-2, and Table 4-3 respectively. Metrics with percent differences greater than 5% are highlighted in yellow and those that are greater than 10% are highlighted in red. Effect sizes greater than 10 are also highlighted in red.

Table 4-1: The effect sizes, standard deviations, and percent differences for each of the comparisons performed between the zero and non-zero BIPED resting ICP configurations for each of the metrics examined for 18.8 J impacts. Percent differences greater than 5% are highlighted in yellow. Those that are greater than 10% are highlighted in red. Effect sizes greater than 10 are also highlighted in red.

LOW ENERGY IMPACTS - EFFECT SIZE OF PARAM. COMPARED TO BIPED MK2 AT 0 INH2O

	BIPED Mk2 0 inH2O		BIPED Mk2 3 inH2O			BIPED Mk2 6 inH2O			BIPED Mk2 9 inH2O		
METRIC	Mean	Std.	Effect Size	Std.	% diff. in Mean	Effect Size	Std.	% diff. in Mean	Effect Size	Std.	% diff. in Mean
PEAK LIN. ACCEL. CoG (g)	80.2	1.4	-0.10	0.7	-0.1	0.78	0.7	0.7	-2.18	0.6	-1.7
MAX. FRONT IPP (kPa)	65.0	1.2	-0.45	0.8	-0.5	-1.13	0.7	-1.2	-3.85	0.6	-3.5
MAX. FRONT CSF-LAYER ICP (kPa)	84.3	1.5	-0.13	0.9	-0.1	-1.75	0.9	-1.8	-4.55	0.7	-4.0
MAX. LEFT CSF-LAYER ICP (kPa)	30.1	1.1	-2.47	0.6	-4.7	-5.19	0.5	-9.0	6.53	0.5	11.7
MAX. RIGHT CSF-LAYER ICP (kPa)	35.2	0.5	5.18	0.2	3.2	-0.99	0.3	-0.8	-3.53	0.8	-7.5
MAX. BACK IPP (kPa)	14.8	0.3	-1.59	0.2	-1.9	2.08	0.1	2.0	6.33	0.2	7.9
MIN. BACK IPP (kPa)	-12.8	0.4	0.36	0.2	0.7	-0.95	0.2	-1.6	2.55	0.2	3.8

Table 4-2: The effect sizes, standard deviations, and percent differences for each of the comparisons performed between the zero and non-zero BIPED resting ICP configurations for each of the metrics examined for 37.7 J impacts. Percent differences greater than 5% are highlighted in yellow. Those that are greater than 10% are highlighted in red. Effect sizes greater than 10 are also highlighted in red.

MEDIUM ENERGY IMPACTS - EFFECT SIZE OF PARAM. COMPARED TO BIPED MK2 AT 0 INH2O

	BIPED Mk2 0 inH2O		BIPED Mk2 3 inH2O			BIPED Mk2 6 inH2O			BIPED Mk2 9 inH2O		
METRIC	Mean	Std.	Effect Size	Std.	% diff. in Mean	Effect Size	Std.	% diff. in Mean	Effect Size	Std.	% diff. in Mean
PEAK LIN. ACCEL. CoG (g)	144.4	2.2	-5.30	1.0	-3.6	-4.22	1.0	-2.9	0.50	1.0	0.4
MAX. FRONT IPP(kPa)	147.1	1.4	1.57	0.8	0.9	2.00	0.7	1.0	7.31	0.8	4.1
MAX. FRONT CSF-LAYER ICP (kPa)	185.4	1.6	1.35	1.0	0.7	1.50	0.9	0.7	8.37	1.0	3.0
MAX. LEFT CSF-LAYER ICP (kPa)	71.3	3.4	-1.43	1.6	-3.2	-2.77	1.6	-6.4	0.36	1.8	-1.4
MAX. RIGHT CSF-LAYER ICP (kPa)	83.6	1.7	-0.96	0.9	-1.0	-3.90	0.8	-3.8	2.43	0.9	-1.1
MAX. BACK IPP (kPa)	24.2	0.3	-10.68	0.6	-26.0	-16.37	0.5	-32.5	-13.45	0.6	-35.4
MIN. BACK IPP (kPa)	-16.4	0.4	8.74	0.2	11.2	8.91	0.2	11.1	1.46	0.2	2.1

Table 4-3: The effect sizes, standard deviations, and percent differences for each of the comparisons performed between the zero and non-zero BIPED resting ICP configurations for each of the metrics examined for 65.9 J impacts. Percent differences greater than 5% are highlighted in yellow. Those that are greater than 10% are highlighted in red. Effect sizes greater than 10 are also highlighted in red.

HIGH ENERGY IMPACTS - EFFECT SIZE OF PARAM. COMPARED TO BIPED MK2 AT 0 INH2O

	BIPED Mk2 0 inH2O		BIPED Mk2 3 inH2O			BIPED Mk2 6 inH2O			BIPED Mk2 9 inH2O		
METRIC	Mean	Std.	Effect Size	Std.	% diff. in Mean	Effect Size	Std.	% diff. in Mean	Effect Size	Std.	% diff. in Mean
PEAK LIN. ACCEL. CoG (g)	182.4	1.5	-0.39	0.7	-0.2	-2.78	0.8	-1.2	-2.74	0.8	-1.3
MAX. FRONT IPP (kPa)	196.8	3.9	-0.55	3.1	-0.9	0.48	2.1	0.5	1.58	2.0	1.6
MAX. FRONT CSF-LAYER ICP (kPa)	246.1	3.9	-0.24	3.4	-0.3	1.16	2.2	1.0	2.55	2.2	2.3
MAX. LEFT CSF-LAYER ICP (kPa)	114.1	5.9	-1.15	3.3	-3.3	-1.34	2.9	-3.4	-2.55	2.7	-6.0
MAX. RIGHT CSF-LAYER ICP (kPa)	123.3	3.6	0.67	3.2	1.8	2.13	2.3	4.0	5.27	2.5	10.6
MAX. BACK IPP (kPa)	42.4	1.0	-2.72	0.5	-3.4	-5.28	0.7	-9.1	-9.11	0.5	-11.4
MIN. BACK IPP (kPa)	-19.3	0.5	1.93	0.4	3.7	1.25	0.4	2.9	3.45	0.3	5.5

4.2 Discussion of the Blunt Impact Experiment

The purpose of this study was to explore the effects of changing the resting ICP in a surrogate headform subjected to pendulum impacts. The kinematic and pressure responses were measured and recorded for impacts at 18.8, 37.7, and 65.9 J of energy while the BIPED was pressurized to resting ICPs of 0, 3, 6, and 9 inH_2O-gauge. Additional impacts were performed on a Hybrid III headform – the current industry standard headform used for evaluating sport, defense, and automotive safety equipment.

When compared to the BIPED, the Hybrid III exhibited larger peak global head accelerations and peak impact forces for the same impact energy levels (Figure 4-2). This is expected since the Hybrid III headform features a skull constructed from metal alloys that are much less compliant than the BIPED's two-piece polyurethane skull. Assuming equivalent transfers of kinetic energy from the pendulum to either the BIPED or the Hybrid III, the Hybrid III's lower compliance allows for less skull deformation during impact than the BIPED, resulting in a higher peak impact force.

At each of the impact energy levels, the peak global head linear accelerations shown in Figure 4-2a, as well as the peak impact forces shown in Figure 4-2b, remained fairly consistent – within 3% – across all configurations of resting ICPs despite the noted significant differences. Based on these two metrics alone, altering the resting ICP does not demonstrate a clear effect on the BIPED's response – particularly, its compliance. Even though some significant differences in peak accelerations and peak impact forces were observed between the resting ICP configurations at each of the impact energy levels, it is difficult to attribute these differences solely to the altered resting ICP. It is possible however, that these differences arose from a systematic error caused by the (in)consistency of the impact location. Between each series of trials for each of the resting ICP configuration, the headform was removed from the surrogate body in order to be pressurized. After replacing the headform, the head was realigned with the pendulum and trials resumed. Because the headform was not mounted on a rigid fixture that can tightly constrain the impact location, some variations in the responses to identical impact conditions were expected. In previous experiments where the headform was nearly completely unconstrained [16], standard deviations of the head accelerations were as high as 11% of the average. In the work presented here, the standard errors for the peak accelerations for each resting ICP configuration remained relatively low (around 1-2% of the corresponding average) suggesting that, once set up, the experiment was

highly repeatable. However, when adjustments were made to alter the resting ICP, the mean differences between the responses of each of the configurations rose up to 4%. Furthermore, the observed significant differences were not consistent for all impact energy levels and that they did not demonstrate a particular trend (i.e. increasing accelerations for increasing resting ICP) Considering the potential for the systematic error and the noted observations together, they suggest that the variation due to altered resting ICP is perhaps not uniquely distinguishable from variations due to inconsistent impact locations when examining peak linear head accelerations and peak impact forces. Essentially, this suggests that any additional internal pressure exerted on the inside of the surrogate skull is not substantial enough to alter its compliance to an extent that is distinguishable – by linear head accelerations and impact forces alone – from slight changes in impact alignment for frontal impacts. As such, global surrogate headform motions in response to a blunt impact, are not substantially affected by increasing the internal pressure of the surrogate headform to anatomically relevant levels. Moreover, the consistency in the peak impact force across resting ICP configurations also suggests that increasing the internal pressure of the surrogate headform does not lead to the skull gaining any substantial resistance to material failures (fractures) caused by blunt impacts.

For impacts at 65.9 J, the peak left and right ICP responses presented in Figure 4-4 might suggest that increasing the resting ICP influences the pressures measured at the left and right sides of the headform. However, while the peak ICPs increased for the left side, the ICPs decreased on the right side. This behaviour is unexpected considering the sensors were mounted symmetrically; the pressures experienced at either location were expected to be identical. This inverse relationship between the peak pressures on either side of the headform might instead suggest that the impact point on the headform shifted from right to left. This was confirmed after examining the component head angular velocity time series. Although head rotation was predominantly about the *y*-axis, the *z*-axis angular velocity is briefly non-zero during the impact. For impacts at 65.9 J, at the 0 inH_2O-gauge resting ICP, the *z*-axis angular velocity was initially negative indicating an impact location anatomically right of the head CoG. The opposite occurred at the 9 inH_2O-gauge resting ICP. This is consistent with the peak left ICP response being less than that of the right for the 0 inH_2O-gauge configuration and greater than the right for the 9 inH_2O-gauge configuration.

Although several statistically significant differences were found between the zero and non-zero resting ICP configurations across the metrics that were recorded, the percent differences in the average metrics between the zero and non-zero resting ICP configurations were nearly all less than 5%. Table 4-1, Table 4-2, and Table 4-3 show that largest percent differences, other than those for the peak left and right ICPs, were found in the maximum IPP recorded at the back parenchyma pressure sensor for 37.7 J impacts. Additionally, as the resting ICP increased, the maximum IPP at the back parenchyma pressure appeared to increase as well. The cause of this observation is not abundantly clear. The complex nature of the pressure wave that develops during impact leads to two of possibly many potential reasons. Here, it is hypothesized that changing the resting ICP of the BIPED may have either (1) affected the shell stiffness enough to alter the flexural wave speed in the skull and/or (2) affected the longitudinal wave speed in the brain itself since it is also under elevated stress.

In the context of both theories, recall that Ganpule et al. discussed the intracranial pressure response during impact and how it is a culmination of several stress waves either directly or indirectly caused by the flexural wave generated in the skull [10], [44]. They also demonstrated that the amplitudes of this response can vary spatially within the brain [10], [44]. If the flexural wave in the skull were to be affected by a change in the shell (skull) stiffness (theory 1), Kopecky and Ripperger analytically demonstrated that such changes affect the pressure responses within a closed container when subjected to an impact [43]. Alternatively – or perhaps additionally – the added static compressive stress on the brain was enough to change the longitudinal wave speed (theory 2). Such a phenomenon has been described by Zhang et al., Ottenio et al., and Destrade and Ogden [50], [51], [52]. If this is the case, again, the cumulative pressure response for a given location within the skull would be affected. Any evidence to the possibility of these altered wave speeds can be seen in the changes in the travel time from the front to the back parenchyma sensors shown in Figure 4-6. These results suggest that the speeds of some wave components may have indeed changed as the resting ICP was increased. Altogether, this would give rise to the differences observed in the maximum pressure recorded at the back parenchyma sensor shown in Figure 4-5.

Wave mechanics aside, these findings must ultimately be considered within the context of evaluating the performance of head protection devices and equipment. If Azar et al. were to replicate their experiments that subjected the BIPED to a free-field blast, but instead used an

internally pressurized BIPED, the attenuation that they observed at the front ICP (IPP) sensor for helmeted blasts vs. non-helmeted, is not expected to vary significantly [15]. Any notable differences that correspond to a change in the resting ICP from the present experimental series are observed at the back sensor, away from the coup site. The parenchyma pressure response and any corresponding brain deformations in region of the back sensor are not expected to be the most severe compared to the rest of the brain for the given impact. Therefore, achieving a more accurate biofidelic response in this region than what is already possible without needing to pressurize the BIPED above 0 inH_2O-gauge may not be necessary. Attention can instead be focused on locations where absolute maximum stress and strain are more likely to occur.

Contrary to recent studies that suggest that an increased resting ICP will reduce the relative motion of the brain during impacts [40], [41], [42], the results of the parenchymal pressures presented in this study demonstrate that the brain does not experience any less energy from the impact due to an increase in the resting ICP. The responses measured at the back of the brain better suggest that increasing the resting ICP may, in fact, increase the stresses experienced due to blunt impacts. These findings do not support the theory that the brain experiences any less relative motion between it and the skull, and thus does not sustain any less energy from the impact as a result of increasing the resting ICP. It is more likely that the protective effect observed in these studies due to the elevated resting ICPs is, instead, a physiological effect in nature. The present surrogate model does not possess any vascularity, ventricles, or any living tissue that regulates CSF production and absorption that *in-vivo* animal models otherwise would possess. As such, the discrepancy between the animal models and the present BIPED model could be attributed to a physiological response to the elevated pressure that causes a change in the brain tissue's mechanical properties, such as increased tissue rigidity. Increasing the pressure alone (as was done in this study) has very little effect on physical properties relevant to the fluid mechanics that govern the brain's motion within the CSF since the peak global head kinematic, ICP, and IPP responses do not indicate any reductions in impact severity. If the viscosity could be changed without affecting the other purposes of CSF, then perhaps additional "shock absorption" could be achieved.

If higher resting ICP levels than those presented here (and higher than typical anatomical levels) were considered, the results would be uncertain. The present results, and the possible theories that were presented to explain them, suggest that even higher resting ICP levels would

lead to higher positive pressures observed in the rear parenchyma. Before exploring these ranges beyond normal anatomical levels, one should consider the applicability of such a scenario and its implications.

Chapter 5: Comparison of the CSF ICP-Acceleration Response and Time Series Analysis of a Modified Surrogate Headform to a Cadaver Model's Response for a Pendulum Blunt Impact Scenario

Chapter 5 presents a limited biofidelity assessment of the pressurized BIPED Mk. 2 configurations. A time series analysis and a simplistic evaluation of the relationship between the CSF ICP and the resultant global head linear acceleration responses of the BIPED Mk. 2 were compared to a cadaver model that exists in literature [25], [26]. The time series of the BIPED's responses at different resting ICPs were compared against a single cadaver experiment using CORrelation and Analysis to assess the congruency of the surrogate model with the cadaver model. Following this, the CSF ICP-acceleration relationships for the BIPED at different resting ICPs were compared to two separate series of published cadaver models [25], [26] using statistical methods. The results are shown and discussed within.

5.1 Background

In previous studies, the BIPED Mk. 1 has been compared to various cadaver head models in order evaluate its biofidelity for use in blunt impact scenarios [16], [18]. These studies focused on replicating the impact parameters used in the respective cadaver studies and then scaling the magnitudes of the kinematic and pressure responses based on the scaling required to match the cadaver global head accelerations where required [16], [18]. From there, headform biofidelity was assessed by using *t*-tests to compare the accuracy and repeatability of peak kinematic and pressure responses with cadaver data, and by using CORrelation and Analysis (CORA) to compare the time histories of the responses with cadaver data [16], [18], [59]. For an *ad hoc* analysis, these comparisons require that the applied insult to the surrogate headform be similar (within reason) to that which was applied in the cadaver study i.e., matching impact parameters such as impulse duration and peak impact force. In this study however, a *post hoc* analysis was performed to assess the biofidelity of the BIPED Mk. 2 relative to the cadaver pendulum impact experiments presented by Nahum and Smith [26] in an attempt to avoid scaling the measured responses. Of the cadaver experiments, the trial(s) with an applied insult(s) most comparable to the experiment presented in the previous chapters, based on peak input force and time duration, are selected for analysis. Biofidelity is assessed by analyzing the time series characteristics of the kinematic and pressure

responses using CORA. Next we compare the CSF ICP-acceleration relationships obtained from the different resting ICP BIPED configurations to the relationships presented by Nahum and Smith [26]. The underlying premise with this assessment is to investigate the effect of changing the resting ICP and evaluate its efficacy as a tool to tune the BIPED's responses towards cadaveric responses.

5.2 Methods

The peak input force for Experiment 37 from Nahum and Smith [26] most closely matched the peak input forces measured for the 65.9 J impacts performed for this work. The input force for Experiment 37 is shown in Figure 5-1 which was originally published in Nahum and Smith [26]. The recorded peak input force was 7.90 kN while the average peak force for the 65.9 J impacts was 7.87 kN. The time durations between the cadaver experiment and the BIPED experiments, however, were different. The time duration was defined as the difference between the first two instances at which the force is equivalent to 20% of the peak force. For the cadaver experiment, the time history of the input force was first extracted from Figure 5-1 using an online plot digitizer [60]. The output from the digitizer was resampled at 17 kHz using MATLAB (R2020b, MathWorks Inc., MA, USA). From there, the time duration was found to be 4.8 ms. For the BIPED experiments, time durations were found to be approximately 3 ms (see Figure 4-1). Although surrogate kinematic and pressure response magnitudes have been scaled in previous studies to match the cadaver data in order to assess the surrogate's biofidelity, time durations have yet to be scaled, and therefore were not manipulated here [14], [18], [61], [62]. Nonetheless, the limited assessment of the BIPED's biofidelity here can still provide valuable insights, particularly in understanding the impact of pressurizing the BIPED Mk. 2 on kinematic and pressure time series responses, as well as the CSF ICP-acceleration relationship, when compared to a similar cadaver experiment.

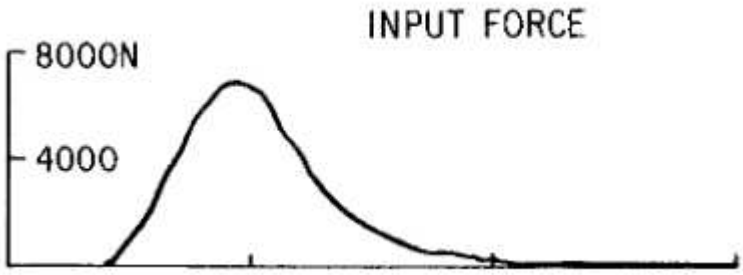

Figure 5-1: Representative plot of input forces measured from the pendulum impacts performed by Nahum and Smith [26].

5.2.1 CORA

After extracting the remaining time histories reported for Experiment 37, using the same plot digitization method and resampling in MATLAB as described above, the time series analysis was performed using CORA [59]. The time histories of the resultant global head linear acceleration, and front and left CSF ICPs for the BIPED Mk. 2 at resting ICPs of 0, 3, 6, and 9 inH_2O-gauge during 65.9 J impacts were compared to the resultant acceleration, frontal, and parietal ICP histories recorded for Experiment 37 from Nahum and Smith. Each BIPED resting ICP configuration was set up as a loadcase with each of the five repetitions designated as a sub-loadcase for a total of 20 sub-loadcases. The time histories of each sensor for each sub-loadcase were directly compared to their corresponding cadaver counterpart from Experiment 37 and evaluated with two methods: cross-correlation (CC) and corridor [59]. The CC method assesses the shape, size, and phase shift between the compared time histories [59]. The corridor method evaluates the distance between the compared signals relative to the default corridor width [59]. Each criterion is quantified with a rating between 0 and 1 [59]. The rating for the CC method is the weighted sum of the shape, 50%, size, 25%, and phase shift, 25% [16], [18], [59]. The overall rating for the signal is the weighted average of the CC method, 50%, and the corridor method, 50%[16], [18], [59]. The rating for the entire trial (sub-loadcase) is the weighted average of the of all the signals: 33% each for the resultant acceleration, the front CSF ICP, and the left CSF ICP [59]. The overall rating for the BIPED resting ICP configuration (loadcase) is the weighted average of all the sub-loadcases: 20% each [59].

The BIPED's right CSF ICP was excluded because the parietal sensor used in the cadaver study was mounted on the left side of the specimens. Furthermore, CORA was originally performed including the right sensor and the results revealed a misleading overall improvement of ratings for increasing resting ICPs due to the right CSF ICP signal of the BIPED. The right CSF ICP signal rating artificially improved, showing greater consistency with the cadaver's left parietal reference signal. Despite the anticipated symmetry between the left and right ICP sensors, they exhibited more consistent signals at higher resting ICPs, suggesting improved positioning of the impact site relative to the sagittal plane as the experimental series progressed. This subtle but noticeable systematic bias became evident when comparing ICP signals using CORA. Following this identification, the CORA test was reconfigured to exclude the right ICP signal which then showed no apparent relationship between resting ICP and the CORA ratings.

After further considering that the reference side ICP signal was derived from the left parietal bone of the cadaver model, the left ICP signal from the BIPED was chosen to remain in the analysis while the right ICP signal was removed. These results and the conclusions are shown in Appendix B.

5.2.2 CSF ICP-Acceleration Comparison

In their findings, Nahum and Smith presented linear relationships between the peak global head accelerations and the peak measured CSF ICPs at the frontal, parietal, and occipital bones, and the posterior fossa for a range of impacts performed on a single specimen [26]. The impacts performed on this single specimen were defined as the Series II impacts. These are shown in Figure 5-2. The Series I impacts, however, were conducted with a different specimen for each trial. Although Nahum and Smith did not analyze the peak pressure-head acceleration responses for Series I, the results can still be plotted. Utilizing the data obtained from the experiment detailed in the preceding chapters, similar relationships between peak ICP and peak head acceleration were established by performing a regression of least squares on the average peak ICP responses at each sensor location for each impact severity level. The front ICP responses collected in the BIPED experiments were compared to the cadaver results from both Series I and II while the left and right BIPED ICP responses were compared to the parietal pressure responses from the cadaver series' as well.

By gathering the ICP-acceleration relationships for both the surrogate headform and each cadaver series, it becomes possible to compare the BIPED's responses with those of the cadaver models. This comparison aims to ascertain whether adjusting the resting ICP of the surrogate headform can enhance its consistency with the cadaver models. To assess the congruency between surrogate and cadaver responses, a statistical comparison of their slopes was conducted. This involved applying linear regression to the combined data from both surrogate and cadaver models at each measurement location. This analysis incorporated a categorical variable for each model type, along with an interaction effect between the categorical variable and head acceleration. The significance of this interaction effect was then determined based on a significance level of 0.05. If the interaction effect could not be deemed significant, the ICP-acceleration response of the BIPED at that given resting ICP would not be significantly different from the cadaver response. Conversely, a significant interaction effect would indicate that the BIPED responds differently than the cadaver series.

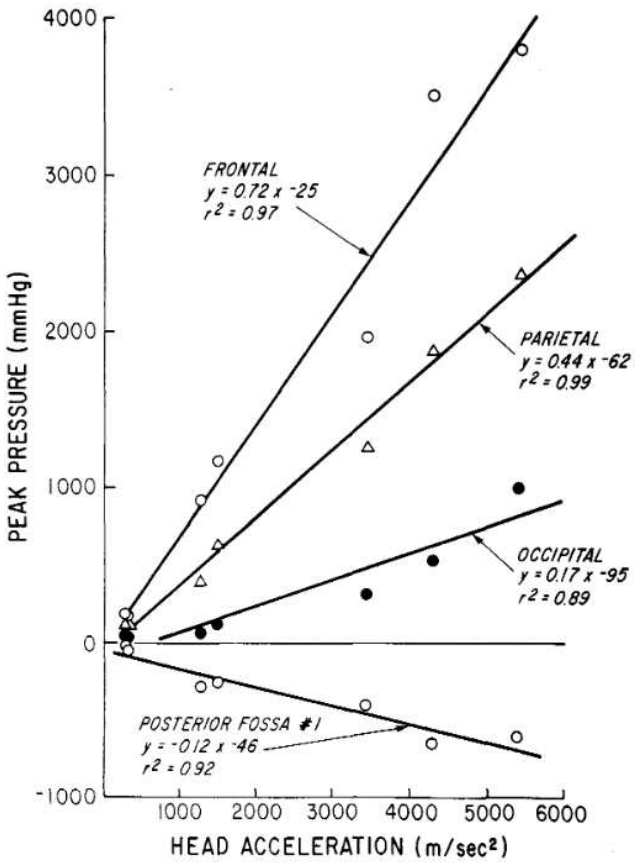

Figure 5-2: Linear relationships between global head acceleration and ICP at various locations in cadaver models as performed by Nahum and Smith [26].

5.3 Results

The average ratings for each of the time histories across all of the sub-loadcases for each of the BIPED configurations (loadcases) are shown in Table 5-1. The overall ratings for each BIPED configuration remained relatively similar as they ranged from 0.612 to 0.617 which were the 6 and 9 inH_2O-gauge configurations respectively. CC and corridor ratings were generally highest for the resultant linear acceleration signals while they were generally lower for the front CSF ICP signals. Front CSF ICP phase shift ratings were 0 for all loadcases indicating too large a phase shift was required to match the cadaver reference signal.

Table 5-1: Average CORA ratings for each sensor for each of the BIPED resting ICP configurations (loadcases). Each loadcase possesses five (*n*=5) trials (sub-loadcases).

BIPED Configuration	Sensor	Shape	Size	Phase	CC	Corridor	Total Rating
0 inH_2O	Res. Accel.	0.734	0.772	0.491	0.682	0.659	0.671
	Front CSF ICP	0.888	0.504	0.000	0.565	0.516	0.540
	Left CSF ICP	0.726	0.747	0.327	0.631	0.628	0.630
	Total Rating						**0.614**
3 inH_2O	Res. Accel.	0.737	0.772	0.500	0.687	0.657	0.672
	Front CSF ICP	0.888	0.477	0.000	0.563	0.517	0.540
	Left CSF ICP	0.738	0.699	0.327	0.625	0.647	0.636
	Total Rating						**0.616**
6 inH_2O	Res. Accel.	0.734	0.780	0.482	0.683	0.651	0.667
	Front CSF ICP	0.896	0.477	0.000	0.567	0.523	0.545
	Left CSF ICP	0.761	0.656	0.318	0.624	0.628	0.626
	Total Rating						**0.612**
9 inH_2O	Res. Accel.	0.731	0.780	0.500	0.685	0.654	0.670
	Front CSF ICP	0.899	0.483	0.000	0.570	0.528	0.549
	Left CSF ICP	0.773	0.614	0.355	0.628	0.636	0.632
	Total Rating						**0.617**

The average ICP-acceleration responses for each BIPED resting ICP configuration for each impact severity, and for each of the cadaver series are plotted in Figure 5-3, Figure 5-4, and Figure 5-5. To determine if there was a significant difference between the slopes of the responses for the BIPED configurations and each of the cadaver series, the test statistics for the interaction effect of the combined models and their significance were calculated and are shown in Table 5-2. As expected, based on the results from Chapter 4, the ICP-acceleration responses for each BIPED configuration shown in Figure 5-3 largely overlap each other. The slopes for the front CSF ICP for the BIPED range from 1.48 to 1.58 kPa/g while the right and left CSF ICP-acceleration slopes range from 0.70 to 0.85 and 0.79 to 0.90 kPa/g respectively. The interaction effects summarized in Table 5-2 show that none of the slopes of the BIPED ICP-acceleration responses at each sensor location for all resting ICP configurations were significantly different than Nahum and Smith's cadaver Series I. Conversely, all slopes of the responses for each resting ICP configuration did significantly differ from cadaver Series II.

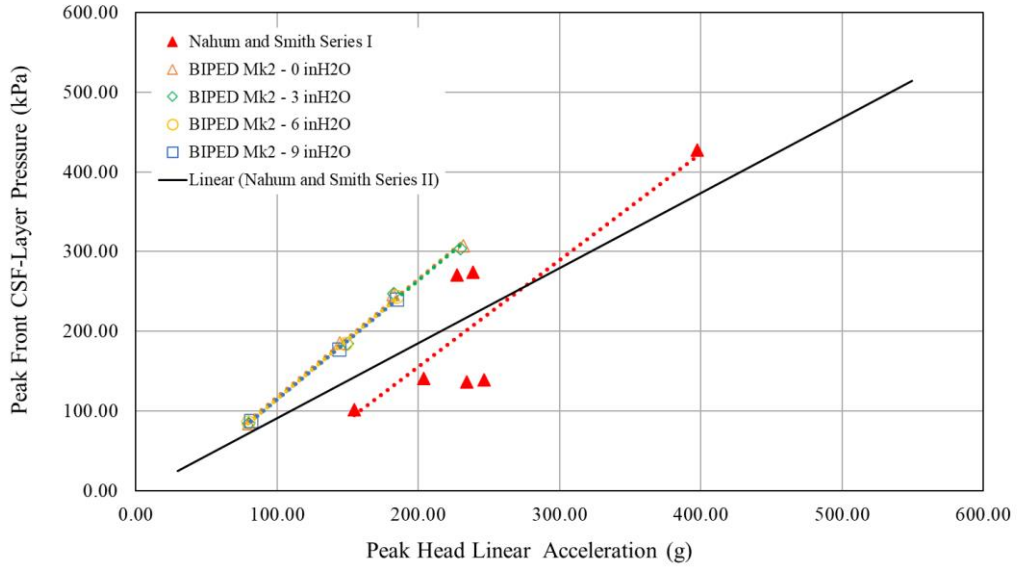

Figure 5-3: Regressions of peak ICP-peak head accelerations for each BIPED resting ICP for pressures recorded at the front of the headform. The frontal pressure responses for Nahum and Smith cadaver Series I and II are plotted as well [26].

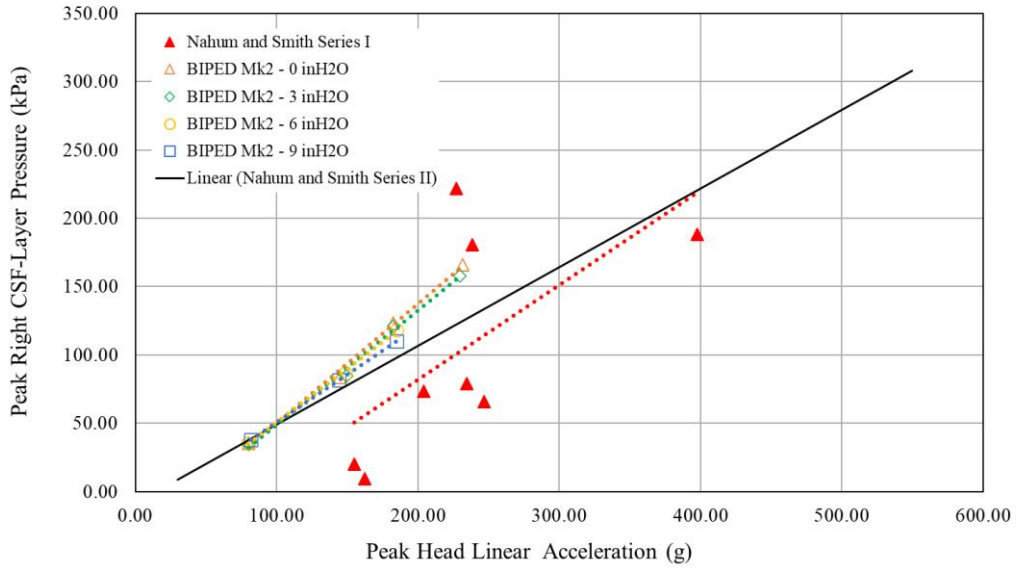

Figure 5-4: Regressions of peak ICP-peak head accelerations for each BIPED resting ICP for pressures recorded at the right side of the headform. The parietal pressure responses for Nahum and Smith cadaver Series I and II are plotted as well [26].

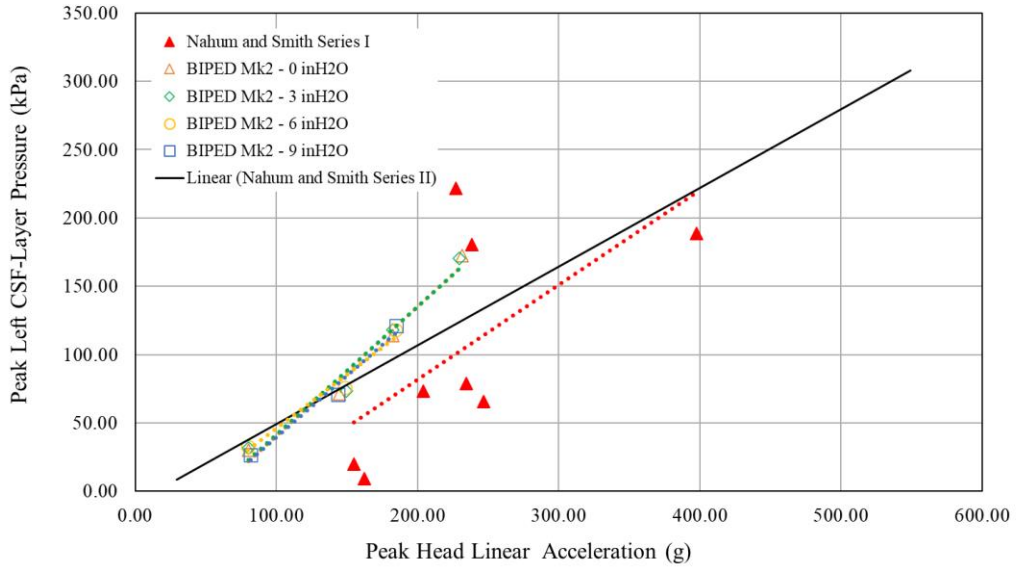

Figure 5-5: Regressions of peak ICP-peak head accelerations for each BIPED resting ICP for pressures recorded at the left side of the headform. The parietal pressure responses for Nahum and Smith cadaver Series I and II are plotted as well [26].

Table 5-2: Test statistics and significance of the interaction effect of the combined data between each BIPED resting ICP configuration and each cadaver series. A significant interaction effect indicates that the BIPED's ICP-acceleration response is significantly different from the corresponding cadaver model.

SIGNIFICANCE OF INTERACTION EFFECT FOR PEAK ICP RESPONSES

	Front ICP		**Right ICP**		**Left ICP**	
	Cadaver Series 1					
	***t*-stat**	***p*-val.**	***t*-stat**	***p*-val.**	***t*-stat**	***p*-val.**
BIPED - 0 INH_2O	0.24	0.81	0.47	0.66	0.58	0.58
BIPED - 3 INH_2O	0.25	0.81	0.41	0.70	0.56	0.59
BIPED - 6 INH_2O	0.17	0.87	0.22	0.83	0.22	0.83
BIPED - 9 INH_2O	0.15	0.88	0.13	0.90	0.34	0.75
	Cadaver Series 2					
	***t*-stat**	***p*-val.**	***t*-stat**	***p*-val.**	***t*-stat**	***p*-val.**
BIPED - 0 INH_2O	16.4	0.00	14.2	0.00	6.4	0.00
BIPED - 3 INH_2O	14.0	0.00	10.7	0.00	5.5	0.00
BIPED - 6 INH_2O	23.9	0.00	15.2	0.00	3.7	0.01
BIPED - 9 INH_2O	42.0	0.00	313.5	0.00	5.4	0.00

5.4 Discussion

In this chapter, a limited *post hoc* assessment of the BIPED's biofidelity was performed with the intent to explore the potential use of altering the resting ICP of a headform as a tool for aligning its kinematic and pressure responses more closely with cadaveric responses. Utilizing the data derived from the experiment detailed in the preceding chapters, our initial analysis involved examining the time series characteristics using CORA. Subsequently, we compared the CSF ICP-acceleration relationships obtained from various resting ICP configurations of the BIPED to those presented by Nahum and Smith.

The previous studies that evaluated the BIPED's biofidelity compared the headform to the cadaver responses to pendulum impacts performed by Nahum and Smith [16], [18], [26]. While the experiment detailed in the preceding chapters was designed based on this cadaver study, impacts with identical force magnitudes in the two datasets do not share matching time durations. Nahum and Smith indicated the use of a soft cushioning material between the cadaver heads and the pendulum which served to prevent the skull from shattering on impact [26]. Because the material was not specified, the experiment presented in this work proceeded with only the bare pendulum ram impacting the unprotected BIPED headform. Without the use of an intermediate material to soften the impact, the time durations for the experiment presented in this work were much shorter.

Despite the dissimilarity in input force duration between the reference impact data and the BIPED experiments, increasing the resting ICP did not bring significant changes to the time histories of the responses. The overall shape of the signals, indicative of their progression and alignment with the reference curve, remained unaltered. All signals exhibited a distinctive monotone wave pattern peaking and returning to zero within a comparable timeframe to the applied input forces. Size ratings for the BIPED signals were consistently larger than the cadaver reference, possibly influenced by the differing input force durations and variations in pressure sensor locations. As was discussed in the previous chapter, different pressure sensor locations can certainly lead to different responses given the complexity of the development of the pressure wave within the skull [9], [10], [44], [47], [48], [49]. The phase ratings were consistently low likely due to the shorter impulses in the responses that arose from the short-duration input force. Again, this

short-duration input force is attributed to the un-cushioned nature of the surrogate impacts. Furthermore, corridor ratings were generally consistent for each signal across various BIPED resting ICP configurations.

It is noteworthy that previous studies have often considered a CORA rating of 0.7 or greater as indicative of "good" biofidelity [18], [63], [64], [65]. Under these comparison conditions, the BIPED Mk. 2 fell short of this threshold. However, it is crucial to recognize the limitations of directly assessing its biofidelity against the cadaver experiment due to differences in input parameters that were not identical or scaled to match in the two experiments. As such, it is more appropriate to comment on the influence the resting ICP might have on altering the time series characteristics of the kinematic and pressure responses of the BIPED during impacts.

Overall, the time histories of the signals were not significantly affected by changes in resting ICP, and responses in each loadcase remained within the defined cadaver reference corridors for similar durations. Understandably, altering the static pressure within the skull does little to affect the development of each of the kinematic and pressure responses. Although implicitly measured from the pressure responses within the cranium and brain, the resultant brain motion was not significantly altered due to the increased resting ICP. This is because the change in static pressure does not alter the viscosity of the CSF layer and therefore does not affect the motion of the brain within the skull during impact events. However, the increased static pressure in the CSF layer may affect the effective stiffness of the skull and the brain such that the propagation of the combined stress waves that develop within are also affected. In the previous chapter, different resting ICPs yielded different maximum pressures recorded within the brain parenchyma measured in the posterior region. Unfortunately, the CSF-layer ICP sensor malfunctioned after the BIPED was assembled so no data were obtained from this location. Based on the results from the previous chapter, perhaps differences may have been observed in the time histories recorded at this back CSF ICP sensor for increased resting ICPs. Further research is required to examine this theory.

The results from the CSF ICP-acceleration response analysis also revealed that changing the resting ICP did not yield a substantial change in the headform's response to blunt impacts. The interaction effects for each BIPED resting ICP configuration, in Table 5-2, were observed to be non-significant for cadaver Series I – tests involving different cadaver specimens – while the

interaction effects compared with cadaver Series II – a single specimen – were indeed significantly different. This finding is consistent with the nature of the BIPED, which does not align with a specific specimen's characteristics, rather it represents an aggregate response not significantly different from a diverse collection of specimens. Moreover, it was noted that resting ICP did not yield discernable differences in the observed outcomes. This suggests that manipulating the resting ICP did not markedly influence the relationship between head acceleration and ICP within the BIPED experiments. Again, changing the static pressure of the headform may only be able to marginally alter the effective stiffness of either (or both) the skull and/or the brain. As such, most peak responses recorded nearest the coup site will go unaffected as was discussed in the previous chapter. It may be informative to investigate the CSF ICP-acceleration relationship for pressure responses measured at the back of the skull since the previous chapter presented different pressure maxima in the posterior region of the brain.

When compared to the ICP-acceleration responses from Li et al., the magnitudes of the slopes for this responses in the current study were similar, if not, larger than those in their work [18]. Li et al. demonstrated in this particular publication that altering the intermediate impact materials does result in a change in the magnitude of the ICP-acceleration response slope. Given that the experiment performed in this study lacked any cushioning between the pendulum ram, the “stiffer” impacts can certainly result in higher pressure magnitudes for a given resultant linear acceleration if a similar peak force is achieved in a shorter time duration. This is because the shorter time duration yields a shorter impulse meaning that less energy is devoted to gross head kinematics and thus more energy is transferred to the pressure wave that develops within the skull.

The results of CORA and the CSF ICP-acceleration response analysis that compose the limited biofidelity assessment presented here, suggest that the BIPED Mk. 2 is moderately biofidelic for forehead blunt impact scenarios. Although the BIPED fell short of a “good” biofidelic threshold with regards to its CORA ratings, again the limitations of the comparison must be recognized. Without scaling the responses proportionally to what is required to match the input forces between the two models, a reasonably similar applied input force is crucial to make an appropriate comparison. With a 20% difference in the time duration of the input force, it is difficult to attribute any discrepancies in the surrogate responses to the model itself rather than to the difference in the impact conditions. That said, the CSF ICP-acceleration response of the BIPED followed similar

trends to that of an aggregate set of diverse cadaver specimens rather than that of a single specimen. This is ideal when the goal is to construct a surrogate model that is representative of the average male.

When taken together, the two analyses above suggest that altering the BIPED's resting ICP does not improve or degrade its overall consistency with published cadaver literature. Altering the resting ICP did not alter the progression and development of the resultant global head linear acceleration, the front CSF ICP, and the left CSF ICP. This is likely because the brain motion during impact was not affected by the different resting ICPs. Similarly, the increased static pressure did not affect the CSF ICP-acceleration response. This characteristic is likely more dependent on the solid structures of the headform and how they interact during impacts. However, it is possible that the increased static pressure may affect pressure signals recorded in the posterior regions of the brain and skull so further work would be required to examine both the time histories and ICP-acceleration relationships relative to cadaver models.

Chapter 6: Conclusions

This thesis explored the influence of a pressurized CSF-layer on the kinematic and pressure responses of a surrogate headform subjected to blunt impacts. First, an instrumented surrogate headform was modified to enable it to establish and maintain a positive, non-zero gauge pressure. It was then subsequently subjected to blunt impacts directed to the forehead with a pendulum apparatus. The analysis that followed examined peak global head accelerations, peak impact forces, peak pressure responses at the front and sides of the CSF layer, and at the anterior and posterior regions of the brain parenchyma. These results were further compared to a cadaver experiment to determine if the changing resting ICPs affected the time histories of the head responses as well as the ICP-acceleration relationship.

The effect of changing the resting ICP in a surrogate headform has very little relevant effect on the global head kinematic and the intracranial and intraparenchymal pressure responses in the context of evaluating the energy attenuating and injury prevention capabilities of head protection devices. Differences in the maximum intraparenchymal pressure (IPP) at the location of the back IPP sensor, opposite the impact site, were observed with the changes in the resting ICP. These differences could be a result of altered wave interactions that govern the developing pressure field in the brain during an impact. Small changes in the mechanical properties of the components of the surrogate head, caused by small changes in the resting ICP, could be enough to alter these wave interactions and create regions of elevated pressure.

The analyses that compared the results from this work to a cadaver study suggest that the BIPED Mk. 2 is moderately biofidelic. While its CSF ICP response scaled with its global head acceleration in a manner that was statistically indistinguishable from that of a collection of several different cadaver specimens, the agreement of the time histories of the kinematic and pressure responses between the BIPED and a single cadaver specimen were below the accepted threshold for “good” biofidelity. This biofidelity assessment is primarily limited by differences in the impact conditions between the two models and the lack of repeated trials for the same impact condition among the cadaver data. Because of this, it is difficult to determine if the properties of the surrogate headform are solely responsible for the discrepancy in the responses or if the source of the variation comes from the dissimilar impact conditions.

Despite the aforementioned limitations, the results from the analysis still indicate that modifying the BIPED's resting ICP does not enhance or diminish its overall alignment with published cadaver literature. The alteration in resting ICP did not influence the progression and development of resultant global head linear acceleration, front CSF ICP, and left CSF ICP. This lack of effect is likely because the varied resting ICPs did not impact the motion of the brain during impact. Moreover, the increased static pressure did not impact the CSF ICP-acceleration response, suggesting that this characteristic is more dependent on the solid structures of the headform and their interactions during impacts. Nevertheless, it is plausible that the heightened static pressure may influence pressure signals recorded in the posterior regions of the brain and skull as noted with the experiments described in this study. Further investigations would be necessary to scrutinize both the time histories and ICP-acceleration relationships concerning cadaver models.

Overall, although changing the resting ICP may alter the intracranial and intraparenchymal pressure wave interactions, the absolute maximum pressures the brain experiences during a blunt impact are not expected to deviate significantly. This is because the hypothesized effect that changing the resting ICP has on the head would primarily affect the high frequency pressure waves (0.5 to 2 ms duration) that are generated in the head and not the lower frequency waves (5 to 10 ms duration). These lower frequency waves are generated when the brain impacts the inside of the skull, and they heavily dominate pressure signals measured at the front of the brain where pressures are typically the highest. The contribution of the higher frequency waves is thought to be more prominent away from the coup site where pressures are typically much lower. The results presented in this study do not suggest that increasing the resting ICP leads to any less relative brain motion during impact and therefore will not significantly affect the global kinematic and pressure response of the headform when subjected to blunt impacts.

These findings must ultimately be considered within the context of evaluating the performance of head protection devices and equipment. The amount of attenuation that has been observed at the coup site of a headform when comparing protected blunt impacts to unprotected impacts is not expected to vary significantly if the headform were instead pressurized to anatomical levels. Plainly speaking, altering the resting ICP of a surrogate headform used to evaluate head protection devices and risk of brain injury due to impact is not expected to significantly affect this evaluation. Discernible variations linked to alterations in resting ICP within the current experimental series

are noticeable primarily at the rear sensor, positioned away from the coup site. The anticipated pressure response in the parenchyma and associated brain deformations in the region of the rear sensor are not expected to be the most severe in comparison to the rest of the brain during the impact. Consequently, establishing a more precise biofidelic environment and thus a more biofidelic response in this specific region may not be imperative. It might be more beneficial to direct attention to locations where absolute maximum pressures are more likely to occur.

That said, within the context of developing a surrogate headform capable of simulating the actual responses of a human head during impact events, biofidelity remains key. The present study demonstrates that perhaps not all anatomical features are relevant to headform biofidelity when used in particular scenarios such as blunt impact. However, this should not detract from the fact that continuous improvements in the biofidelity of head models over the past several decades have, overall, unlocked deeper insights into the biomechanics of impacts and the mechanisms of brain injury. This has led to the continued enhancement of head protection devices in hopes of mitigating the burden of traumatic brain injury.

References

[1] "Traumatic brain injury: Epidemiology, classification, and pathophysiology - UpToDate." Accessed: Sep. 25, 2023. [Online]. Available: https://www.uptodate.com/contents/traumatic-brain-injury-epidemiology-classification-and-pathophysiology/print

[2] GBD 2016 Traumatic Brain Injury and Spinal Cord Injury Collaborators, "Global, regional, and national burden of traumatic brain injury and spinal cord injury, 1990-2016: a systematic analysis for the Global Burden of Disease Study 2016," *Lancet Neurol*, vol. 18, no. 1, pp. 56–87, Jan. 2019, doi: 10.1016/S1474-4422(18)30415-0.

[3] M. C. Dewan *et al.*, "Estimating the global incidence of traumatic brain injury," *J Neurosurg*, vol. 130, no. 4, pp. 1080–1097, Apr. 2018, doi: 10.3171/2017.10.JNS17352.

[4] J. Seifert, "Incidence and economic burden of injuries in the United States," *J Epidemiol Community Health*, vol. 61, no. 10, p. 926, Oct. 2007, doi: 10.1136/jech.2007.059717.

[5] D. W. Wright, A. Kellermann, L. C. McGuire, B. Chen, and T. Popovic, "CDC Grand Rounds: Reducing Severe Traumatic Brain Injury in the United States," *MMWR Morb Mortal Wkly Rep*, vol. 62, no. 27, pp. 549–552, Jul. 2013.

[6] J. R. Crandall *et al.*, "Human surrogates for injury biomechanics research," *Clin Anat*, vol. 24, no. 3, Art. no. 3, Apr. 2011, doi: 10.1002/ca.21152.

[7] V. R. Hodgson, M. W. Mason, and L. M. Thomas, "Head Model for Impact," SAE International, 1972. [Online]. Available: https://doi.org/10.4271/720969

[8] Eyitejumade A. Sogbesan, "Design and Analysis of Blast Induced Traumatic Brain Injury Mechanism Using a Surrogate Headform: Instrumentation and Outcomes," University of Nebraska-Lincoln, Nebraska, USA, 2011. [Online]. Available: https://apps.dtic.mil/dtic/tr/fulltext/u2/a537846.pdf

[9] S. G. Ganpule, "Mechanics of blast loading on post-mortem human and surrogate heads in the study of Traumatic Brain Injury (TBI) using experimental and computational approaches," p. 289.

[10] S. Ganpule, A. Alai, E. Plougonven, and N. Chandra, "Mechanics of blast loading on the head models in the study of traumatic brain injury using experimental and computational approaches," *Biomech Model Mechanobiol*, vol. 12, no. 3, pp. 511–531, Jun. 2013, doi: 10.1007/s10237-012-0421-8.

[11] E. A. Kennedy, "The Development and Validation of a Biofidelic Synthetic Eye for the Facial and Ocular CountermeasUre Safety (FOCUS) Headform," Aug. 2007, Accessed: Feb. 27, 2023. [Online]. Available: https://vtechworks.lib.vt.edu/handle/10919/28618

[12] S Ouellet, A. Bouamoul, R. Gauvin, J. S. Binette, K.V. Williams, and L. Martineau, "Development of a Biofidelic Head Surrogate for Blast-Induced Traumatic Brain Injury Assessment." Defence Research and Development Canada (DRDC), 2012.

[13] N. Petrone, G. Carraro, S. D. Castello, L. Broggio, A. Koptyug, and M. Bäckström, "A Novel Instrumented Human Head Surrogate for the Impact Evaluation of Helmets," *Proceedings*, vol. 2, no. 6, p. 269, Feb. 2018, doi: 10.3390/proceedings2060269.

[14] N. Petrone *et al.*, "Feasibility of using a novel instrumented human head surrogate to measure helmet, head and brain kinematics and intracranial pressure during multidirectional impact tests," *Journal of Science and Medicine in Sport*, vol. 22, pp. S78–S84, Aug. 2019, doi: 10.1016/j.jsams.2019.05.015.

[15] A. Azar, K. B. Bhagavathula, J. Hogan, S. Ouellet, S. Satapathy, and C. R. Dennison, "Protective Headgear Attenuates Forces on the Inner Table and Pressure in the Brain Parenchyma During Blast and Impact: An Experimental Study Using a Simulant-Based

Surrogate Model of the Human Head," *J Biomech Eng*, vol. 142, no. 4, Apr. 2020, doi: 10.1115/1.4044926.
[16] Y. Li, S. Ouellet, A. H. Vette, D. Raboud, A. Martin, and C. R. Dennison, "Evaluation of the Kinematic Biofidelity and Inter-Test Repeatability of Global Accelerations and Brain Parenchyma Pressure for a Head–Brain Physical Model," *Journal of Biomechanical Engineering*, vol. 143, no. 9, p. 091006, Sep. 2021, doi: 10.1115/1.4050752.
[17] Y. Li *et al.*, "Influence of surrogate scalp material and thickness on head impact responses: Toward a biofidelic head-brain physical model," *Journal of the Mechanical Behavior of Biomedical Materials*, vol. 142, p. 105859, Jun. 2023, doi: 10.1016/j.jmbbm.2023.105859.
[18] Y. Li *et al.*, "Evaluating the Intracranial Pressure Biofidelity and Response Repeatability of a Physical Head-Brain Model in Frontal Impacts," *Ann Biomed Eng*, vol. 51, no. 8, pp. 1816–1833, Aug. 2023, doi: 10.1007/s10439-023-03198-x.
[19] R. Chauvet *et al.*, "Development of a Detailed Finite Element Model of the BIPED MK2 and Verification of Fidelity in Two Cases of Blunt Impact," *Pending Submission*.
[20] A. MacAlister, "Surrogate Head Forms for the Evaluation of Head Injury Risk," 2013.
[21] T. Whyte *et al.*, "A Review of Impact Testing Methods for Headgear in Sports: Considerations for Improved Prevention of Head Injury Through Research and Standards," *Journal of Biomechanical Engineering*, vol. 141, no. 7, p. 070803, Jul. 2019, doi: 10.1115/1.4043140.
[22] J. S. Giudice, G. Park, K. Kong, A. Bailey, R. Kent, and M. B. Panzer, "Development of Open-Source Dummy and Impactor Models for the Assessment of American Football Helmet Finite Element Models," *Ann Biomed Eng*, vol. 47, no. 2, pp. 464–474, Feb. 2019, doi: 10.1007/s10439-018-02155-3.
[23] A. Azar *et al.*, "An optical fibre transducer for measuring kinetics of skull-brain interaction in a surrogate model of the human head subjected to blast overpressure," *IEEE Sensors Journal*, pp. 1–1, 2018, doi: 10.1109/JSEN.2018.2872392.
[24] R. L. Stalnaker, J. W. Melvin, G. S. Nusholtz, N. M. Alem, and J. B. Benson, "Head Impact Response," *SAE Transactions*, vol. 86, pp. 3156–3170, 1977.
[25] A. M. Nahum and R. W. Smith, "An Experimental Model for Closed Head Impact Injury," *SAE Transactions*, vol. 85, pp. 2638–2651, 1976.
[26] A. M. Nahum, R. Smith, and C. C. Ward, "Intracranial Pressure Dynamics During Head Impact," presented at the 21st Stapp Car Crash Conference, Feb. 1977, p. 770922. doi: 10.4271/770922.
[27] W. N. Hardy *et al.*, "A Study of the Response of the Human Cadaver Head to Impact," *Stapp Car Crash J*, vol. 51, pp. 17–80, Oct. 2007.
[28] A. Alshareef *et al.*, "Biomechanics of the Human Brain during Dynamic Rotation of the Head," *Journal of Neurotrauma*, vol. 37, no. 13, pp. 1546–1555, Jul. 2020, doi: 10.1089/neu.2019.6847.
[29] C. Got, A. Patel, and G. Walfisch, "Results of Experimental Head Impacts on Cadavers: The Various Data Obtained and Their Relations to Some Measured Physical Parameters," *STAPP CAR CRASH CONFERENCE*, vol. 22, p. 44.
[30] K. Engelborghs, J. Verlooy, J. Van Reempts, B. Van Deuren, M. Van de Ven, and M. Borgers, "Temporal changes in intracranial pressure in a modified experimental model of closed head injury," *J Neurosurg*, vol. 89, no. 5, pp. 796–806, Nov. 1998, doi: 10.3171/jns.1998.89.5.0796.

[31] H. Bolouri, A. Säljö, D. C. Viano, and A. Hamberger, “Animal model for sport-related concussion; ICP and cognitive function,” *Acta Neurologica Scandinavica*, vol. 125, no. 4, pp. 241–247, 2012, doi: 10.1111/j.1600-0404.2011.01614.x.
[32] H. Bolouri and H. Zetterberg, “Animal Models for Concussion: Molecular and Cognitive Assessments—Relevance to Sport and Military Concussions,” in *Brain Neurotrauma: Molecular, Neuropsychological, and Rehabilitation Aspects*, F. H. Kobeissy, Ed., in Frontiers in Neuroengineering. , Boca Raton (FL): CRC Press/Taylor & Francis, 2015. Accessed: Apr. 10, 2023. [Online]. Available: http://www.ncbi.nlm.nih.gov/books/NBK299196/
[33] E. G. Takhounts, R. H. Eppinger, J. Q. Campbell, R. E. Tannous, E. D. Power, and L. S. Shook, “On the Development of the SIMon Finite Element Head Model,” *Stapp Car Crash Journal*, vol. 47, pp. 107–133, 2003.
[34] H. Mao *et al.*, “Development of a Finite Element Human Head Model Partially Validated with Thirty Five Experimental Cases,” *Journal of Biomechanical Engineering*, vol. 135, no. 11, 2013.
[35] R. Chauvet, A. Martin, L. Westover, S. Ouellet, and C. R. Dennison, “Brain Injury Prevention Evaluation Device Finite Element Simulation,” presented at the Alberta Biomedical Engineering Conference, 2022.
[36] L. N. Telano and S. Baker, “Physiology, Cerebral Spinal Fluid,” in *StatPearls*, Treasure Island (FL): StatPearls Publishing, 2023. Accessed: Aug. 04, 2023. [Online]. Available: http://www.ncbi.nlm.nih.gov/books/NBK519007/
[37] L. Chen, G. Elias, M. P. Yostos, B. Stimec, J. Fasel, and K. Murphy, “Pathways of cerebrospinal fluid outflow: a deeper understanding of resorption,” *Neuroradiology*, vol. 57, no. 2, pp. 139–147, Feb. 2015, doi: 10.1007/s00234-014-1461-9.
[38] K. Oshio, H. Watanabe, Y. Song, A. S. Verkman, and G. T. Manley, “Reduced cerebrospinal fluid production and intracranial pressure in mice lacking choroid plexus water channel Aquaporin-1,” *The FASEB Journal*, vol. 19, no. 1, pp. 76–78, 2005, doi: https://doi.org/10.1096/fj.04-1711fje.
[39] D. HODGSON, J. SHIPPEN, and R. SUNDERLAND, “Protective role of cerebrospinal fluid in brain injuries,” *Arch Dis Child*, vol. 84, no. 2, p. 187, Feb. 2001, doi: 10.1136/adc.84.2.187a.
[40] R. Mannix *et al.*, “Internal Jugular Vein Compression Collar Mitigates Histopathological Alterations after Closed Head Rotational Head Impact in Swine: A Pilot Study,” *Neuroscience*, vol. 437, pp. 132–144, Jun. 2020, doi: 10.1016/j.neuroscience.2020.04.009.
[41] D. W. Smith, J. E. Bailes, J. A. Fisher, J. Robles, R. C. Turner, and J. D. Mills, “Internal Jugular Vein Compression Mitigates Traumatic Axonal Injury in a Rat Model by Reducing the Intracranial Slosh Effect:,” *Neurosurgery*, vol. 70, no. 3, pp. 740–746, Mar. 2012, doi: 10.1227/NEU.0b013e318235b991.
[42] R. C. Turner, Z. J. Naser, J. E. Bailes, D. W. Smith, J. A. Fisher, and C. L. Rosen, “Effect of slosh mitigation on histologic markers of traumatic brain injury: Laboratory investigation,” *Journal of Neurosurgery*, vol. 117, no. 6, pp. 1110–1118, Dec. 2012, doi: 10.3171/2012.8.JNS12358.
[43] J. A. Kopecky and E. A. Ripperger, “Closed brain injuries: An engineering analysis,” *Journal of Biomechanics*, vol. 2, no. 1, pp. 29–34, Mar. 1969, doi: 10.1016/0021-9290(69)90039-6.
[44] S. Ganpule and N. Chandra, “Mechanics of Interaction of Blast Waves on Surrogate Head: Effect of Head Orientation,” presented at the ASME 2013 Summer Bioengineering

Conference, American Society of Mechanical Engineers Digital Collection, Jan. 2014. doi: 10.1115/SBC2013-14754.
[45] S. Ouellet, C. Bir, and A. Bouamoul, "Direct comparison of the primary blast response of a physical head model with post-mortem human subjects," in *PASS 2014, Cambridge UK*, Sep. 2014.
[46] S. Ouellet and M. Philippens, "The multi-modal responses of a physical head model subjected to various blast exposure conditions," *Shock Waves*, vol. 28, no. 1, pp. 19–36, Jan. 2018, doi: 10.1007/s00193-017-0771-3.
[47] C. W. Pearce and P. G. Young, "On the Pressure Response in the Brain due to Short Duration Blunt Impacts," *PLOS ONE*, vol. 9, no. 12, p. e114292, Dec. 2014, doi: 10.1371/journal.pone.0114292.
[48] P. A. Taylor and C. C. Ford, "Simulation of Blast-Induced Early-Time Intracranial Wave Physics leading to Traumatic Brain Injury," *Journal of Biomechanical Engineering*, vol. 131, no. 6, Apr. 2009, doi: 10.1115/1.3118765.
[49] M. Grujicic, W. C. Bell, B. Pandurangan, and P. S. Glomski, "Fluid/Structure Interaction Computational Investigation of Blast-Wave Mitigation Efficacy of the Advanced Combat Helmet," *J. of Materi Eng and Perform*, vol. 20, no. 6, pp. 877–893, Aug. 2011, doi: 10.1007/s11665-010-9724-z.
[50] L. Zhang, Z. Zhang, R. Zhang, M. Gao, and J. Xie, "The Ultrasonic P-Wave Velocity-Stress Relationship and Energy Evolution of Sandstone under Uniaxial Loading-Unloading Conditions," *Advances in Materials Science and Engineering*, vol. 2021, p. e9921716, Jun. 2021, doi: 10.1155/2021/9921716.
[51] M. Otténio, M. Destrade, and R. W. Ogden, "Acoustic waves at the interface of a pre-stressed incompressible elastic solid and a viscous fluid," *International Journal of Non-Linear Mechanics*, vol. 42, no. 2, pp. 310–320, Mar. 2007, doi: 10.1016/j.ijnonlinmec.2006.10.001.
[52] M. Destrade and R. W. Ogden, "On stress-dependent elastic moduli and wave speeds," *IMA Journal of Applied Mathematics*, vol. 78, no. 5, pp. 965–997, Oct. 2013, doi: 10.1093/imamat/hxs003.
[53] F. Frank, "Inflation valve," US2600862A, Jun. 17, 1952 Accessed: Nov. 01, 2023. [Online]. Available: https://patents.google.com/patent/US2600862/en
[54] G. H. F. Schrader, "UNITED STATES PATENT OFFICE.".
[55] "Brass tire Valve Core | Shengshi Weiye." Accessed: Nov. 02, 2023. [Online]. Available: https://www.tyre-valves.com/brass-tire-valve-core.html
[56] A. S. Iwaskiw *et al.*, "The measurement of intracranial pressure and brain displacement due to short-duration dynamic overpressure loading," *Shock Waves*, vol. 28, no. 1, pp. 63–83, Jan. 2018, doi: 10.1007/s00193-017-0759-z.
[57] S. of A. Engineers, "J211 - (R) Instrumentation for impact test - Part 1 - electronic instrumentation," Society of Automotive Engineers, 2003.
[58] A. J. Padgaonkar, K. W. Krieger, and A. I. King, "Measurement of Angular Acceleration of a Rigid Body Using Linear Accelerometers," *J. Appl. Mech*, vol. 42, no. 3, Art. no. 3, Sep. 1975, doi: 10.1115/1.3423640.
[59] C. Thunert, "CORAplus Release 4.0.4 User's Manual." pdb – Partnership for Dummy Technology and Biomechanics, May 2017. Accessed: Nov. 22, 2023. [Online]. Available: https://www.pdb-org.com/en/information/18-cora-download.html
[60] "PlotDigitizer: Version 3.1.5." 2023. [Online]. Available: https://plotdigitizer.com

[61] E. S. Gurdjian, H. R. Lissner, F. G. Evans, L. M. Patrick, and W. G. Hardy, “Intracranial pressure and acceleration accompanying head impacts in human cadavers,” *Surg Gynecol Obstet*, vol. 113, pp. 185–190, Aug. 1961.
[62] S. Fujiwara, Y. Yanagida, and Y. Mizoi, “Impact-induced intracranial pressure caused by an accelerated motion of the head or by skull deformation; an experimental study using physical models of the head and neck, and ones of the skull,” *Forensic Science International*, vol. 43, no. 2, pp. 159–169, Oct. 1989, doi: 10.1016/0379-0738(89)90132-1.
[63] C. Gehre and S. Stahlschmidt, “Assessment of Dummy Models by Using Objective Rating Methods,” presented at the 22nd International Technical Conference on the Enhanced Safety of Vehicles (ESV)National Highway Traffic Safety Administration, 2011. Accessed: Aug. 24, 2022. [Online]. Available: https://trid.trb.org/view/1365453
[64] “ISO 15830-1:2013, Road vehicles — Design and performance specifications for the WorldSID 50th percentile male side-impact dummy,” ISO Standard 2, 2013.
[65] “ISO TR 9790 - Road Vehicles - Anthropomorphic Side Impact Dummy - Lateral Impact Response Requirements to Assess the Biofidelity of the Dummy.”

Appendix A: The Paper in Full

Appendix A contains the current draft (at time of writing) of the manuscript that will be submitted to the ASME Journal of Biomechanical Engineering.

SEE FULL TEXT BELOW

A laboratory study on the kinematic and pressure responses of an internally pressurized novel surrogate headform subjected to blunt impacts

Ashton A. Martin
Department of Mechanical Engineering
University of Alberta
116 St and 85 Ave Edmonton, Alberta T6G 2R3
ashton3@ualberta.ca

Robert Chauvet
Department of Mechanical Engineering
University of Alberta
116 St and 85 Ave Edmonton, Alberta T6G 2R3
rchauvet@ualberta.ca

Aaron Brice
Department of Mechanical Engineering
University of Victoria
3800 Finnerty Rd, Victoria, BC V8P 5C2
aaronbrice@uvic.ca

Lindsey Westover
Department of Mechanical Engineering
Department of Biomedical Engineering
University of Alberta
116 St and 85 Ave Edmonton, Alberta T6G 2R3
lwestove@ualberta.ca

Simon Ouellet
Defence Research and Development Canada – Valcartier Research Centre
2459 de la Bravoure Road, Québec, Québec, G3J 1X5

Christopher R. Dennison
Department of Mechanical Engineering
University of Victoria
3800 Finnerty Rd, Victoria, BC V8P 5C2
dennison@uvic.ca

1 Introduction

Mild traumatic brain injury (mTBI) remains an ever-prevalent issue and leading cause of global disease burden [1], [2]. Advances in the technology used to study mTBI have allowed researchers to gain a deeper understanding of the mechanisms that lead to injury. Such advances include the development of several types of head models that can be more ethically used in place of *in-vivo* human subjects. In particular, artificial surrogate headforms serve as a robust and cost-effective substitute that allows for extensive testing when studying the biomechanics of head injury [3]–[5].

Artificial surrogate headforms have been widely used in the field of biomechanics to study the response of the human head to blunt impacts. These models serve as simplified representations of the human head and are used to simulate real-world scenarios to understand the mechanisms of injury. In order to record accurate responses, the devices themselves must be as anatomically biofidelic as possible so as to not disrupt the response during injury/loading scenarios [5].

At present, researchers have developed (or are developing) several surrogate headforms, each with varying levels of complexity and detail lent to mimicking the anatomy of the head. Models such as the Hybrid III possess a surrogate skull made of metal alloys enveloped by a soft vinyl skin but lacks a surrogate brain among all other intra-cranial anatomy [3], [4]. The head model developed by Hodgeson et al. at Wayne State University sought to improve the biofidelity of available headforms, at the time, that could be used for impact safety standards compliance tests in automotive contexts [6]. Although the skull of this particular headform is made of a self-hardening urethane foam that contains a cranial cavity, in which a surrogate gel brain was cast, the model lacks any instrumentation that measures intra-cranial responses aside from a triaxial accelerometer located at the head center-of-gravity (CoG) [6]. The Realistic Explosive Dummy (RED) Head developed at the University of Nebraska by Sogbesan and Ganpule, however, did possess such instrumentation. The RED head was based on the Facial and Ocular Countermeasure Safety (FOCUS) headform and is meant to replicate the 50^{th} percentile male soldier [7]–[10]. It possesses a polyurethane skull and an instrumented cranial cavity for a surrogate brain and cerebrospinal fluid simulant (CSF-simulant). However, the intra-cranial instruments were abandoned in favor of using an accompanying Finite Element model (FE model) to predict intra-cranial responses. This was accomplished by physically simulating a loading scenario (blast),

measuring the applied load with externally-mounted pressure sensors, and applying this measured input to the FE model [7]–[9].

More recently developed models finally make use of their intra-cranial instruments. Examples include the Brain Injury Protection Evaluation Device (BIPED) and the Instrumented Human Head Surrogate (IHHeadS_1) which feature a plastic skull, a urethane or gel skin, a gel brain, and can contain a cerebrospinal fluid simulant (CSF-simulant) [11]–[13]. Not only did these features serve to improve the anatomical likeness of either head model, they were carefully instrumented to record the responses in each of the head models' components [11], [14]–[16], [12], [13]. The BIPED's surrogate brain contains pressure sensors that measure intraparenchymal stresses while the surrogate skull can be modified to measure external pressure waves and internal stresses and pressures at the CSF layer [11], [14]–[16]. Meanwhile, the IHHeadS_1 features nine triaxial accelerometers and ten pressure sensors to measure head kinematics and intracranial pressures at various local regions throughout the head model [12], [13].This allowed researchers to gain a deeper understanding of the mechanisms that lead to brain injury as a result of several loading scenarios.

Although these more anatomically correct artificial surrogate headforms possess many biofidelic features, the accurate representation of the resting intracranial pressure (ICP) in these models has remained a challenge. In practice, artificial headforms that contain CSF-simulant are filled with simulant while simultaneously evacuating the cavity of air until the fluid composition within the cranial cavity is nearly 100% CSF-simulant. However, no additional steps are taken to pressurize the cavity to known *in-vivo* levels [11]–[13].

The average resting ICP in healthy humans is approximately between 7 and 15 mmHg when measured via spinal tap while subjects are supine. This is the pressure that can be measured in the space occupied by the CSF. In general, it has been more practical to account for this pressurization inhuman cadaver, animal, and finite element head models used for injury biomechanics research. In the case of the cadaver models, head models were generally perfused via the ventricular duct to a consistent pressure through the course of the experiments. In particular, Nahum and smith pressurized their cadaveric models to 74 mmH_2O (5 mmHg) at the ventricular level while Hardy et al. maintained a perfusion pressure of 75 mmHg at the carotid artery [17], [18]. Following Stalnaker et al., Got and Patel also recognized the importance of pressurizing their cadaver models.

As such, they pressurized their specimens until they obtained a reading of 120 mmHg at the carotid artery [19], [20]. Despite pressurizing their respective head models, none of the aforementioned investigators reported any explorations into the effects of altering this cranial pressure. Most studies that utilize animal models are *in-vivo* experiments, therefore ICP may only be measured rather than controlled. Moreover, ICP is not necessarily measured during the impact event, rather, it is measured before impact and at several instances post-impact to allow for comparison of between-subject ICP and cognitive performance [21]–[23].

In-silico finite element (FE) models, present a much easier opportunity to implement changes in material properties. Pressure changes in the CSF can be reflected by simple material changes to the CSF bulk modulus. However, the extent of the changes that an increased CSF pressure will effect remains largely unknown *in-vivo*. Because of this, it is difficult to assume that FE models can accurately and completely represent the physical and mechanical effects of the increase in CSF pressure especially since FE models are limited in how they model the CSF layer. Even industry standard models of the human head, such as the SIMON and GHBMC, use a Lagrangian solid to represent the fluid layer rather than a multiphysics fluid approach [24], [25]. This poses difficulties in changing the properties of a solid in order to represent the changes to a fluid. A FE model of the BIPED has also been created, but it also relies on a Lagrangian solid for its fluid layer. While the opportunity to implement changes in CSF pressure are greatest in FE models, the lack of advances in modelling a multiphysics fluid layer limit the confidence that blunt impact experiments accurately represent the physiological response in the human head. To gain confidence in the biofidelity of these experiments, the role of CSF must first be considered before the mechanical responses and the underlying physiological responses that present after blunt head impacts following changes in CSF pressure can be understood.

The CSF is primarily generated in the ventricular system and occupies this space as well as the subarachnoid space surrounding the brain and the spinal cord [26]–[28]. It is composed of about 99% water while the rest is proteins and minerals. CSF serves three primary functions: (1) nourishment, (2) waste removal, and (3) protection. The former two purposes are achieved by allowing nutrients to pass to the brain and removing waste excreted by the brain. CSF offers chemical/molecular protection to the brain by disallowing harmful molecules to pass. When immersed in CSF, the brain and spinal cord gain a form of mechanical protection since they are

neutrally buoyant. Moreover, the CSF serves as a shock absorber to lessen the severity of brain-skull impacts [26]–[28]. Based on this, some researchers conducted further studies on the CSF's shock-absorbing abilities. These studies suggest that increasing this resting intra-cranial pressure can reduce relative motion between the brain and skull during a head impact through a phenomenon coined as "slosh mitigation" [29]–[31]. It is thought that the added pressure forces the CSF to occupy previously empty space thus limiting the volume for which the brain can move [29]–[31].

The present study considers another potential effect of increasing the resting ICP in the CSF-layer that would be observed during blunt impacts to the head. As mentioned previously, pressure changes in the CSF can be represented by minute changes to the bulk modulus of the CSF-layer assuming the volume available for the CSF remained unchanged. Although small, this change may affect the overall shell stiffness of the skull which may have a cascading effect on the pressure wave that develops during an impact event. Kopecky and Ripperger demonstrated that different pressure amplitudes are observed after impacting a fluid-filled closed shell by changing either the fluid bulk modulus or the shell stiffness [32]. This phenomenon has been implicitly explored by previous researchers when investigating the pressure waves that develop in head models that are subjected to blunt impacts or to blasts.

It is well known that the pressure wave that forms within the brain during an impact or blast is caused and affected by several factors. The most obvious and largest contributor to this pressure wave is the component generated by the brain slamming against the skull at the coup site. This produces a longitudinal and a shear stress wave with a duration of 5 to 10 ms as seen in Nahum and Smith, Hardy et al. and in Pearce et al. [17], [18], [33]. Prior to this brain-skull impact, however, is when another contributing pressure wave is generated. At impact, the skull deforms which generates a flexural wave that propagates through the skull (or surrogate skull) itself. Along the way, the rippling flexural waves generate further stress waves in the CSF that are then passed onto the brain and culminate into a resultant stress wave in the parenchyma [34], [35], [33], [8], [36]. This stress wave has a duration of approximately 0.5 to 2 ms as seen in blast experiments and blunt impact experiments with smaller objects traveling at high velocities [8], [15], [36]–[38]. Ganpule et al. discuss the complex nature of the pressure (stress) field within the brain and how the intracranial response to injury largely depends on the interactions of all these wave

components. Therefore, if changing the resting pressure of the CSF affects the effective shell stiffness of the skull, any flexural waves generated or transmitted through the skull may indeed be affected.

In addition to the flexural waves, wave speeds in and around the brain, itself, may be affected by increasing the resting ICP. Zhang et al. demonstrated that the longitudinal wave speed within an object under a compressive load increases logarithmically [39], while Ottenio et al. and Destrade and Ogden analytically demonstrated that compressing a hyperelastic object ultimately leads to altered wave speeds [40], [41].As such, under different compressive loads, the brain may transmit some or all of the components of the pressure wave at different speeds. Altogether, these changes may be enough to significantly affect the locations and magnitudes of the maximum stresses experienced within the brain.To deepen our understanding of the role of the CSF – in particular, the role of the positive pressure of the CSF – we performed an experimental series to explore the effects of changing the internal resting ICP of a surrogate headform (the BIPED). In this study, a surrogate headform is subjected to blunt impacts while measuring global head kinematic, intraparenchymal pressure (IPP), and intracranial pressure (ICP) responses. The goal of this study is to understand the role of resting ICP in the biomechanics of head injury. The results from this study will provide valuable insight into the biomechanics of head injury and may aid in the development of more accurate injury prediction models.

2 Methods

The effects of changing the resting ICP of a head model were explored with the Brain Injury Protection Evaluation Device (BIPED) surrogate headform developed by Defense Research and Development Canada, Valcartier Research Centre (DRDC – VRC). The second version dubbed the BIPED Mk. 2, shown in Figure 1**,** features a two-part skull meant to encase a surrogate brain, the falx and tentorium membranes, and a cerebrospinal fluid (CSF) simulant layer [42]. The top and bottom halves of the skull are then sealed with an o-ring and with a urethane adhesive (AP-2220 Armor-Bond SEMI-FLEX, BJB Materials, CA USA). The inferior side of the BIPED Mk. 2 still possess a nodding block to attach to a surrogate neck, but it also features a counterbalance meant to improve the biofidelity of the headform's moment of inertia by relocating the center of mass. The particular BIPED used for this paper was then modified to control and set the resting

ICP. A pair of Schrader valves were installed in the inferior side of the basilar skull, posterior to the nodding joint (Figure 1). This allowed for the use of a custom fill-tool with an isolating valve and a bourdon pressure gauge to fill and set the resting ICP of the headform when positioned supine. For this experimental series, the headform was set to resting ICPs of 0, 3, 6, and 9 inH_2O gauge (0, 5.6, 11.2, and 16.8 mmHg or 0, 0.75, 1.5, 2.24 kPa).

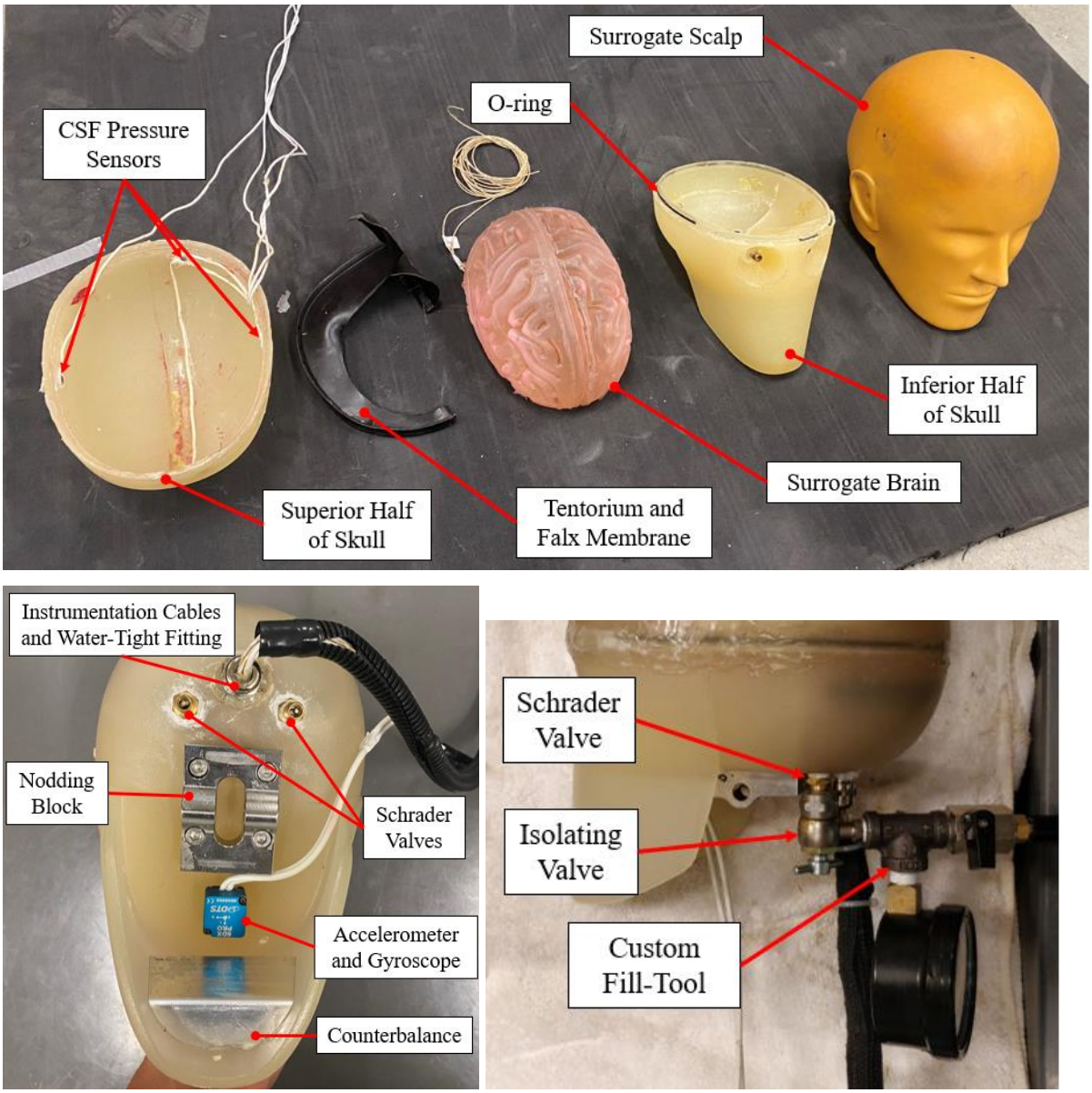

Figure 1: Components and instrumentation of the BIPED Mk. 2 and the custom fill-tool used to pressurize the intra-cranium.

The surrogate brain, shown in the x-ray image in Figure 2, is molded around two pressure sensors (XCL-072, Kulite Semiconductor Products, NJ USA) that capture front and back

intraparenchymal pressure responses. An additional three pressure sensors (MS5407, TE Connectivity Ltd, CA USA) are embedded into the skull such that the sensing diaphragms are flush with the inner surface of the skull and thus could capture the ICP responses in the CSF layer. A fourth pressure sensor was installed at the posterior inner surface of the skull, but data were not collected from it due to a malfunction with the installation. Finally, a DTS 6DX sensor (DTS 6DX PRO, DTS Inc, CA USA) is mounted underneath the chin to measure global head linear accelerations and angular velocities.

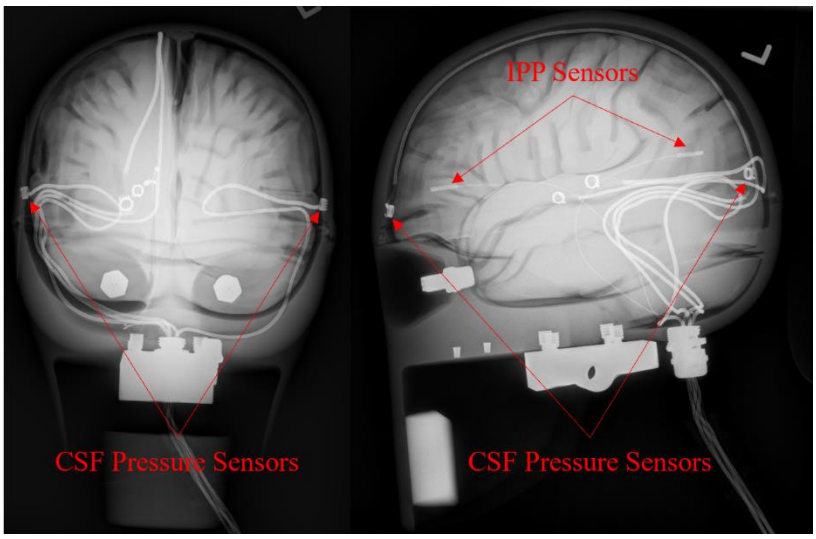

Figure 2: Anteroposterior and lateral x-ray images depicting locations of pressure sensors.

A fourth-order digital Butterworth filter was used to filter signals from all sensors. Angular velocities were filtered with a cutoff frequency of 300 Hz, while the pressure signals were filtered at 1650 Hz. The acceleration and impact force signals were filtered with a cutoff frequency of 1650 Hz as well, according to the j211 standard [43]. Accelerations at the sensor's location were then transformed to the head center of gravity with the following vector and relative acceleration equation:

$$\vec{r}_{\mathrm{CoG/DTS}} = \langle -60.5, 0, -62.2 \rangle \cdot 10^{-3}\ \mathrm{m} \quad \textbf{(1)}$$

$$\vec{a}_{\mathrm{CoG}} = \vec{a}_{\mathrm{DTS}} + \vec{\alpha} \times \vec{r}_{\mathrm{CoG/DTS}} - \vec{\omega} \times (\vec{\omega} \times \vec{r}_{\mathrm{CoG/DTS}}) \quad \textbf{(2)}$$

where $\vec{r}_{\mathrm{CoG/DTS}}$ denotes the relative distance from the DTS sensor location to the head center of gravity (CoG), $\vec{a}_{\mathrm{CoG}}$ is the acceleration vector at the head CoG, $\vec{a}_{\mathrm{DTS}}$ is the acceleration vector at the DTS sensor, and $\vec{\alpha}$ and $\vec{\omega}$ denote the angular acceleration and velocity vectors of the head respectively. The angular acceleration is obtained from cumulative trapezoidal integration of the angular velocity signal.

The experimental series followed the setup presented in Li et al, which is based on Nahum and Smith, save for the substitution of a full body 50th percentile male Hybrid III surrogate for the neck gimbal and rail system[16], [17]. Following internal pressurization, the headform was attached to the surrogate body. The surrogate was seated in a chair with its torso tilted forward such that the headform's Frankfurt plane was at an angle of 45 degrees relative to the line of impact Figure 3.

A pendulum was used to impact the forehead of the headform five times each with 18.8, 37.7, and 65.9 J of energy, for each of the four different resting ICPs. Impact force was measured with a PCB C03 force transducer (PCB 208C05, PCB Piezotronics Inc., NY USA) mounted to the pendulum ram in a similar manner to the impact anvil in Li et al. [42]. The average peak kinematic and pressure responses from the impacts were grouped by impact energy and by resting ICP. Within each impact energy level, all BIPED configurations with a non-zero resting ICP were then compared against the zero resting ICP configuration for statistical differences using student's t-test assuming unequal variances given the small sample size (n = 5) at each resting ICP and impact energy level combination. A significance level of 0.05 was chosen for these comparisons.

The impacts were then repeated with a Hybrid III headform to offer a kinematic comparison to the current industry standard headform.

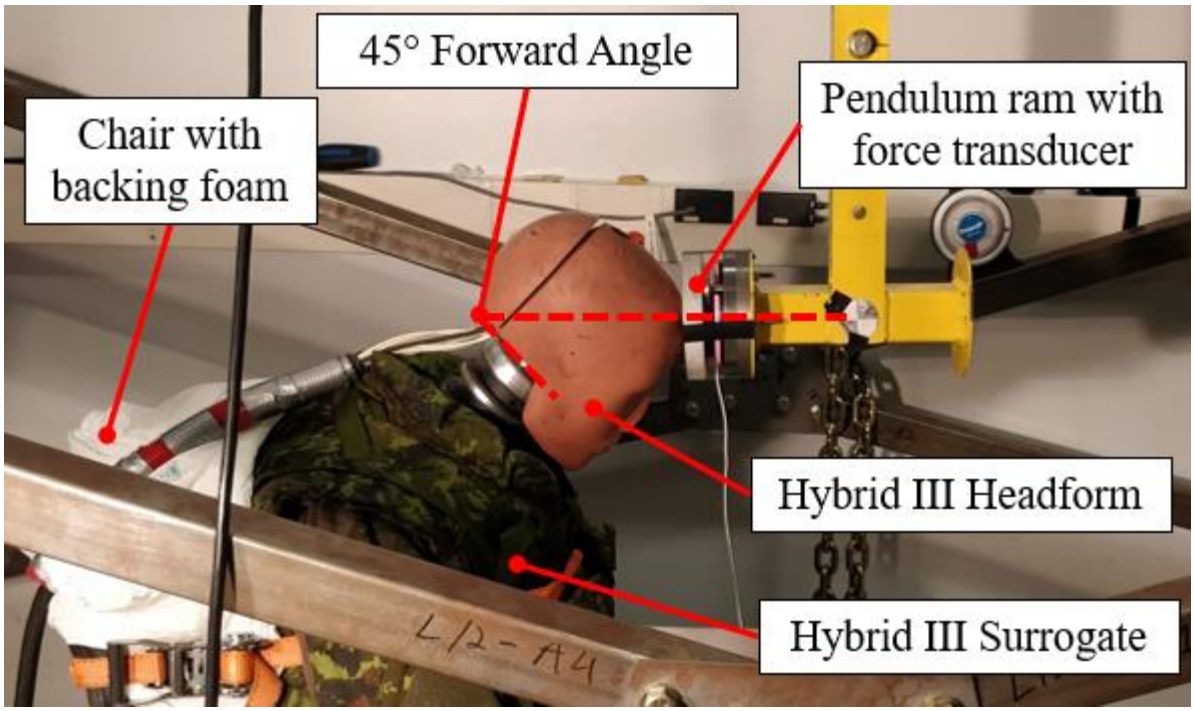

Figure 3: Pendulum impact experimental setup where a seated Hybrid III full body surrogate with its headform angled forward at 45° forward is subjected to a blunt impact. The force of impact is measured by a force transducer located in the ram of the pendulum. This setup was replicated after substituting the Hybrid III headform for the BIPED Mk. 2 headform.

Data were recorded following the coordinate system shown in Figure 4.

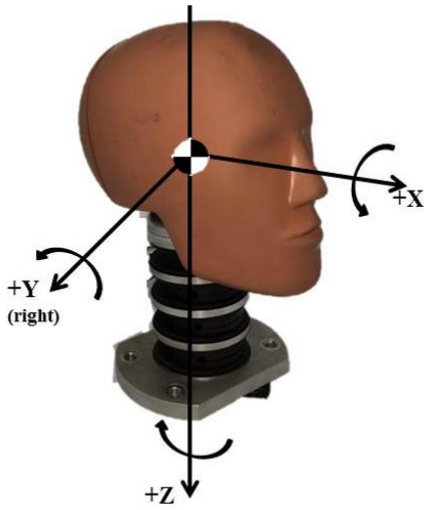

Figure 4: Headform coordinate system applied to recorded data. The *x*-axis represents the sagittal axis, the *y*-axis represents the frontal axis, and the *z*-represents the longitudinal axis. The positive directions are indicated by the arrow heads.

3 Results

All of the experimental kinematic and pressure responses are characteristic of blunt impacts directed to the forehead: acceleration histories shown in Figure 5 show a rapid acceleration phase in the *x*- and *z*-components (sagittal and longitudinal axes of the head respectively) followed by a deceleration phase; head rotation was predominantly about the *y*-axis (frontal axis); impact force, recorded at the pendulum, rose and peaked in unison with head accelerations. Additionally, while the anterior (front) IPP and anterior (front) CSF-layer ICP rose to a positive maximum pressure, the posterior (back) IPP exhibited an initial corresponding drop in pressure followed by a rise in pressure prior to settling. Pressure histories at the left and right CSF-layer were nearly identical in magnitude across the entire window for the given impact event.

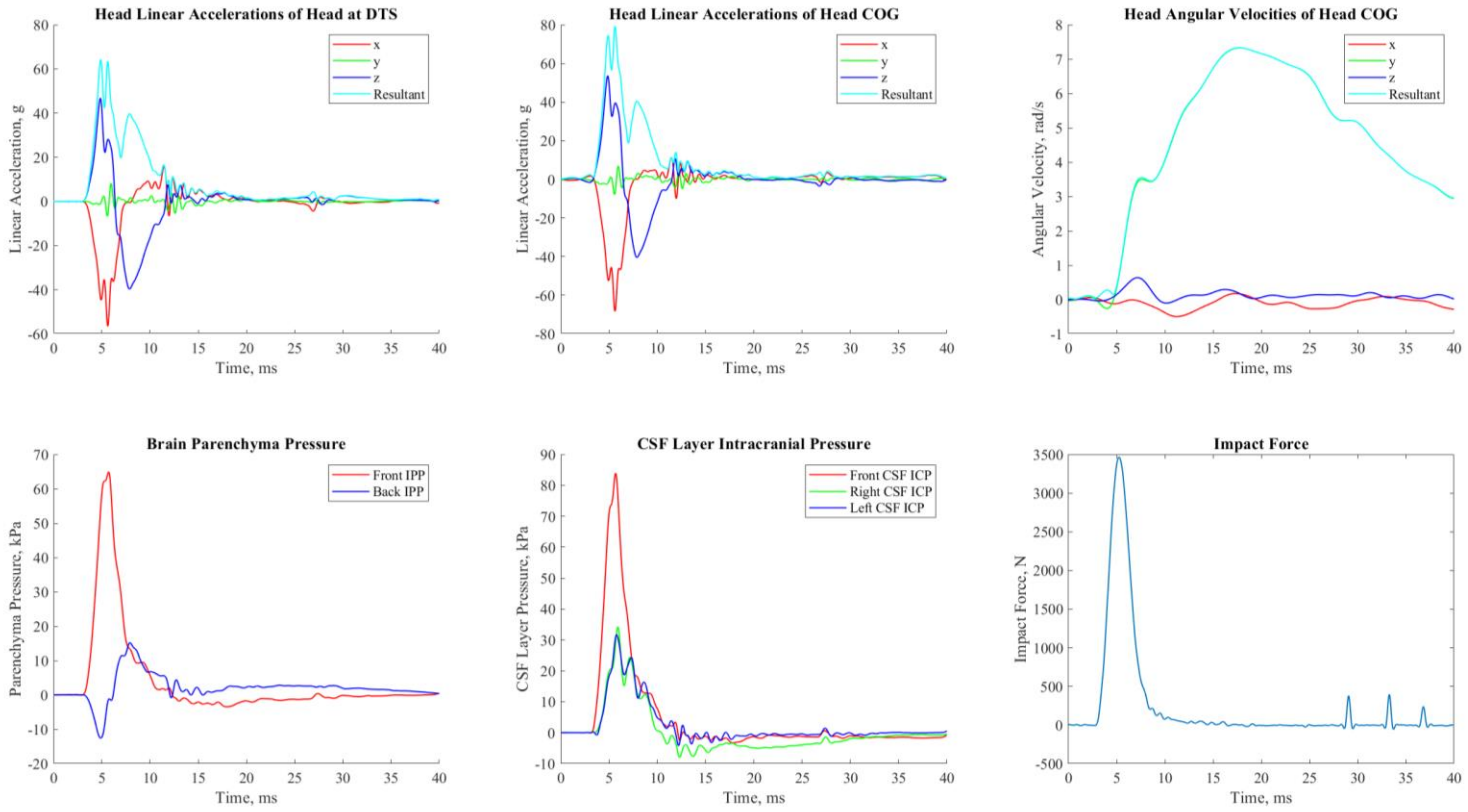

Figure 5: Time series traces of global head kinematics, intraparenchyma pressures, CSF-layer intracranial pressures, and impact force measured at the pendulum.

The average peak resultant head linear accelerations of each BIPED ICP configuration remained consistently within 3% of other configurations within each of the different impact energy levels. Figure 6a. shows that at 18.8 J impacts, the BIPED's average peak head accelerations ranged from 79.0 to 80.6g (where g is the gravitational acceleration constant of 9.81 m/s^2). At 37.7 J, average peak accelerations ranged from 144.4 to 148.8g while the range for 65.9 J impacts was from 182.4 to 184.7g. The Hybrid III's average peak head linear accelerations were 97.0, 150.5, and 214.2g for 18.8, 37.7, and 65.9 J impacts, respectively. These accelerations are higher than the BIPED at each energy level. Comparison tests revealed that at 37.7 J of impact energy, peak accelerations experienced by the BIPED when pressurized to 3 and 6 inH_2O were significantly different from the BIPED at 0 inH_2O. For 65.9 J impacts, the 6 and 9 inH_2O BIPED configurations were significantly different from the 0 inH_2O configuration. Significant differences are indicated with an asterisk (p-value < 0.05).

Figure 6b. depicts a similar trend in consistency for the average peak force between each BIPED configuration. For impacts 18.8, 37.7, and 65.9 J of energy, the average peak impact force ranged from 3.4-3.5 kN, 5.9-6.3 kN, and 7.8-7.9 kN, respectively. The average peak impact force with the Hybrid III was again higher than the BIPED for each impact scenario. The impact forces applied to the Hybrid III were 4.7, 7.0, and 9.4 kN for impacts at 18.8, 37.7, and 65.9 J.

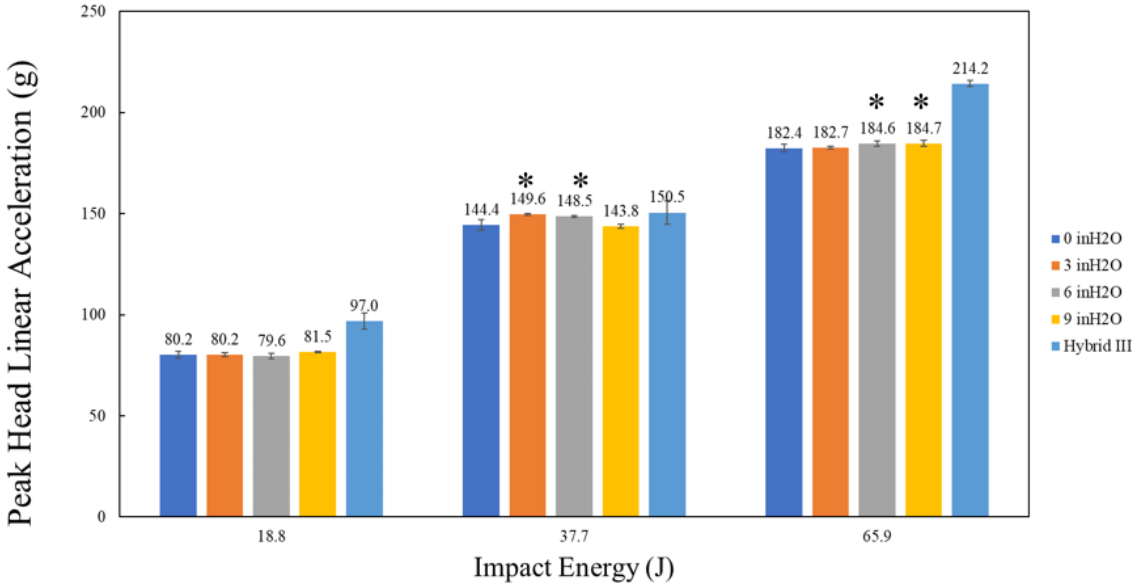

(a)

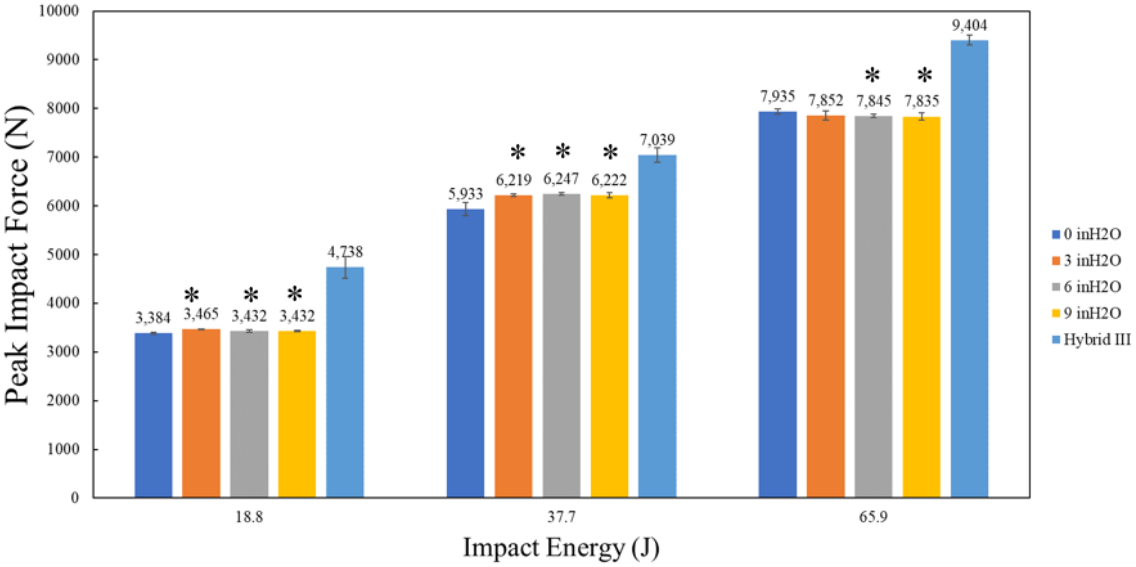

(b)

Figure 6: Average peak head linear accelerations (a) and peak impact forces (b) of the Hybrid III headform and the BIPED headform pressurized to 0, 3, 6, and 9 inH_2O-gauge. Error bars indicate one standard error assuming a t-distribution with α=0.05 and v=4. An asterisk (*) indicates a significant difference from the BIPED pressurized to 0 inH_2O (p-value <0.05, n=5). Comparison tests were only performed for BIPED configurations.

For each of the BIPED configurations, the average maximum intra-cranial and intraparenchymal pressures at the front of the headform, as well as the average maximum and minimum intraparenchymal pressures at the back of the headform were graphed below in Figure

7. Much like the average peak linear head accelerations, the frontal ICP and IPPs were consistent across BIPED resting ICP configurations. At each impact energy level, the average peak front ICP for BIPED configurations with non-zero resting ICP deviated by as much as 4% from the 0-gauge resting ICP configuration. Likewise, the average peak front IPP deviated by as much as 4% between the non-zero and 0 gauge resting ICP configurations for each impact energy level. At all impact energy levels, the peak front CSF ICP of only the 9 inH_2O configuration was significantly different from the 0 inH_2O configuration. For maximum front IPP, the 9 inH_2O configuration was again the only configuration that was significantly different from the BIPED set to a resting ICP of 0 inH_2O at each of the impact levels except for 65.9 J impacts. Significant differences are indicated with an asterisk (p-value < 0.05).

The minimum and maximum back IPP present more variation between the headform configurations. At the lowest impact energy level, average maximum and minimum back IPPs for the 3 and 6 inH_2O-gauge configurations deviated by as much as 2% from the 0 inH_2O-gauge headform configuration while a resting ICP of 9 inH_2O-gauge resulted in deviations as much as 8% from the 0 inH_2O-gauge configuration. For 37.7 J impacts, while increasing the resting ICP, the average minimum back IPP initially dropped by about 2 kPa between the 0 and 3 inH_2O-gauge configurations, did not change from 3 and 6 inH_2O-gauge, and finally increased by about 2 kPa at 9 inH_2O-gauge resting ICP. For 65.9 J impacts, the average minimum back IPP decreased from 19.3 kPa to 18.3 kPa when increasing the resting ICP. The average maximum back IPP increased from 24.6 to 33.1 kPa and 42.4 to 47.3 kPa for impacts of 37.7 and 65.9 J, when increasing the resting ICP. At the 37.7 J impact energy level, the average minimum back IPP for the 3 and 6 inH_2O configurations were significantly different from the 0 inH_2O-gauge resting ICP while at 65.9 J, only the 9 inH_2O-gauge resting ICP configuration was significantly different. The average maximum back IPP for each of the non-zero resting ICP configurations were all significantly different than the 0 inH_2O-gauge resting ICP for impacts at 37.7 and 65.9 J. For 18.8 J impacts, the average maximum back IPP for the 9 inH_2O-gauge configuration was the only configuration that was significantly different from the 0 inH_2O-gauge resting ICP configuration.

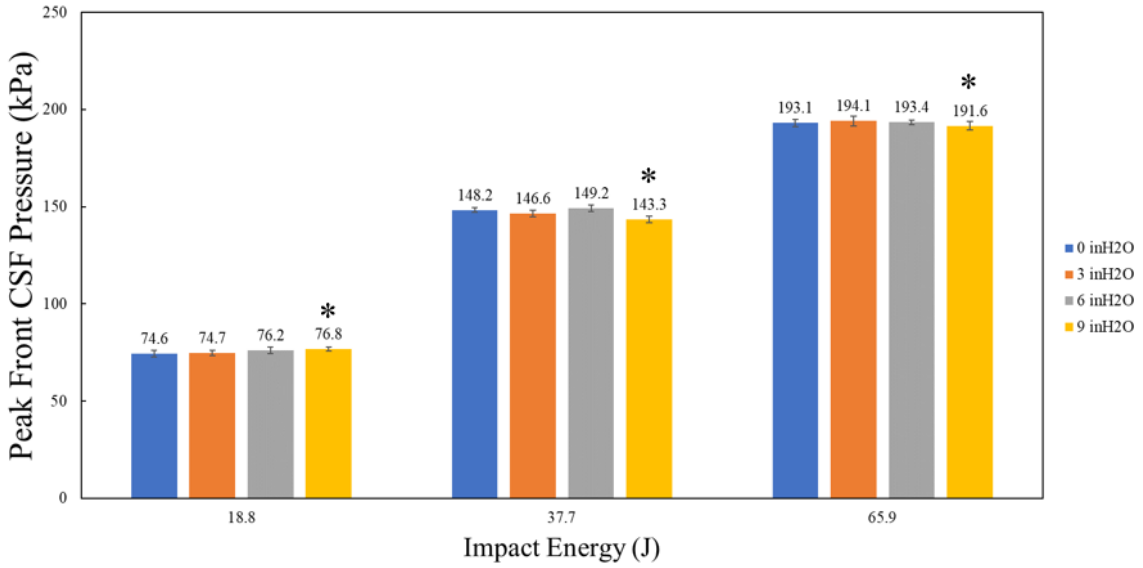
Peak Front CSF Pressure (kPa)
250
200
150
100
50
0
74.6
74.7
76.2
76.8
148.2
146.6
149.2
143.3
193.1
194.1
193.4
191.6
*
*
*
18.8
37.7
65.9
Impact Energy (J)
0 inH2O
3 inH2O
6 inH2O
9 inH2O

(a)

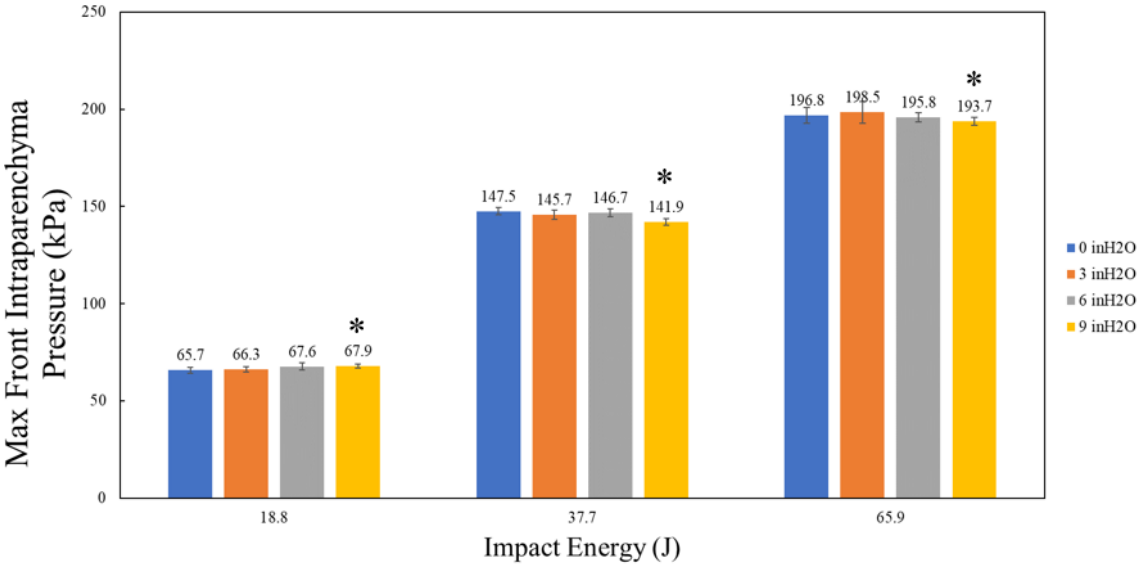
Max Front Intraparenchyma Pressure (kPa)
250
200
150
100
50
0
65.7
66.3
67.6
67.9
147.5
145.7
146.7
141.9
196.8
198.5
195.8
193.7
*
*
*
18.8
37.7
65.9
Impact Energy (J)
0 inH2O
3 inH2O
6 inH2O
9 inH2O

(b)

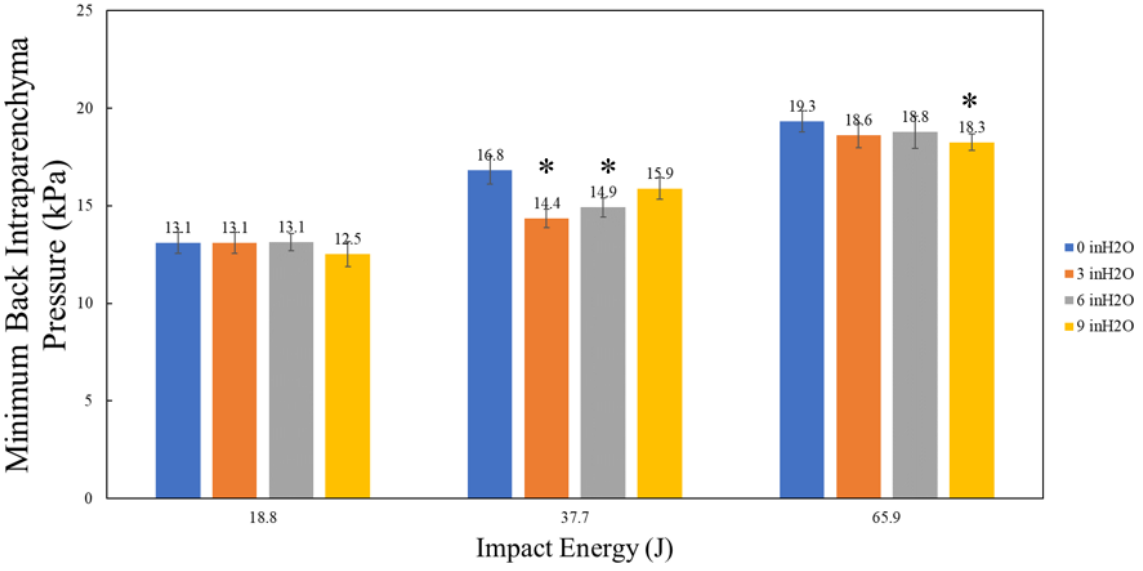
Minimum Back Intraparenchyma Pressure (kPa)
25
20
15
10
5
0
13.1
13.1
13.1
12.5
16.8
14.4
14.9
15.9
19.3
18.6
18.8
18.3
*
*
*
18.8
37.7
65.9
Impact Energy (J)
0 inH2O
3 inH2O
6 inH2O
9 inH2O

(c)

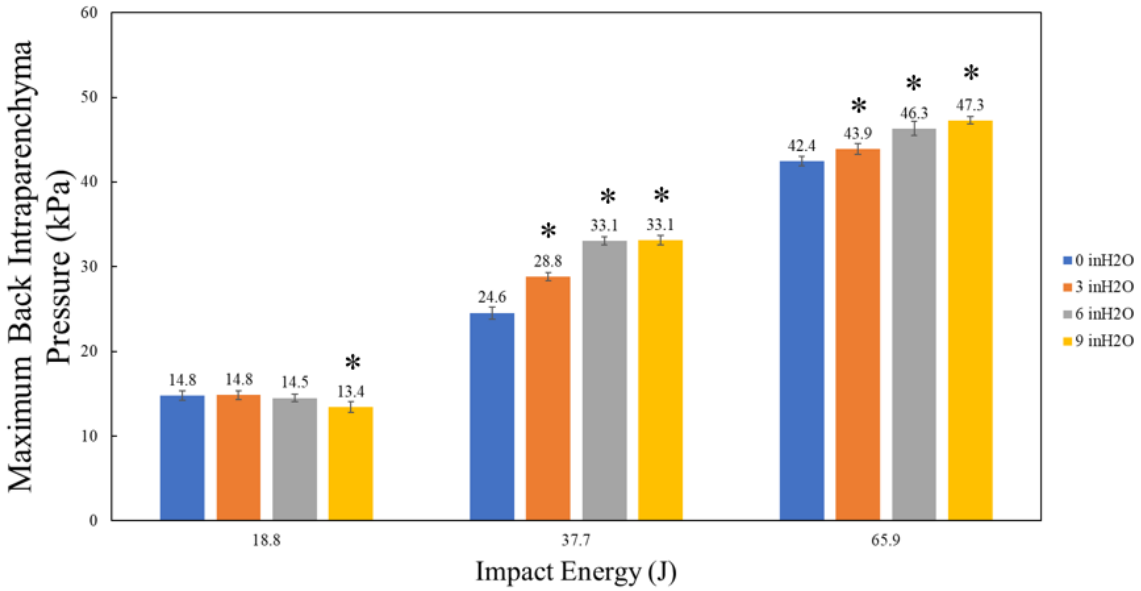

(d)

Figure 7: Average peak intra-cranial (a) and intraparenchymal (b) pressures measured at the front of the BIPED and average minimum (c) and maximum (d) intraparenchymal pressures measured at the back of the the BIPED when pressurized to 0, 3, 6, and 9 inH_2O-gauge. Error bars indicate one standard error assuming a t-distribution with α=0.05 and v=4. An asterisk (*) indicates a significant difference from the BIPED pressurized to 0 inH_2O (p-value <0.05, n=5).

Lastly, in addition to the kinematic and pressure histories, the time taken for the parenchyma pressure wave to travel from the front IPP sensor to the back IPP sensor was calculated by taking the time difference between the respective sensors' maxima. The average times for this pressure wave propagation for each of the experiment configurations are tabulated in Figure 4 4. Overall, as the impact energy increased, the travel time for the wave decreased from as high as 2.36 ms to as low as 1.66 ms. For 18.8 J impacts, the travel times between each BIPED configuration vary as much as 5%. For both the 37.7 and 65.9 J impacts, the average wave travel time gradually decreases as the resting ICP increases. The travel time decreased as much as 7% for the 37.7 J impacts. However, the only significant differences in travel time were found at the 18.8 and 37.7 J impacts, for the 9 inH2O-gauge configuration.

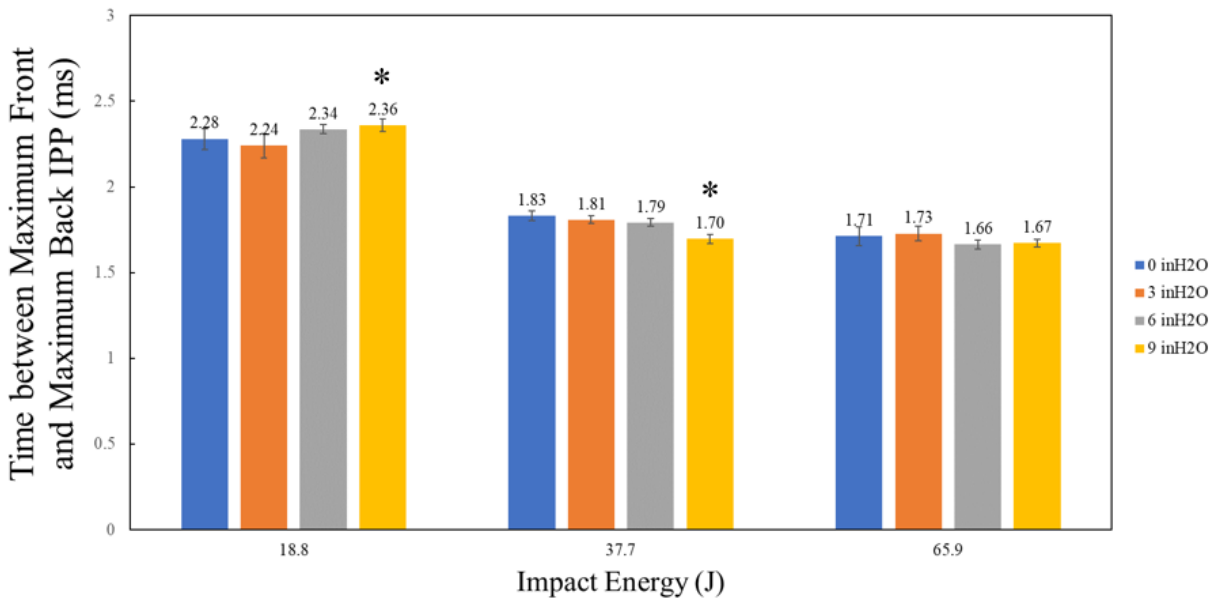

Figure 8: Average time taken for the parenchyma pressure wave to travel from the front IPP sensor to the back IPP sensor. Error bars indicate one standard error assuming a t-distribution with α=0.05 and v=4. An asterisk (*) indicates a significant difference from the BIPED pressurized to 0 inH_2O (p-value <0.05, n=5).

A summary of the Cohen's *d* effect sizes, standard deviations (assuming unequal variances), and the percent differences in the means between the zero and each of the non-zero BIPED resting ICP configurations for each of the metrics, excluding the pressure wave travel time, were tabulated. The summary for the 18.8 J impacts is shown in Table 1 while the summaries for the 37.7 J impacts, and the 65.9 J impacts are shown in Table 2 and Table 3 respectively. Metrics with percent differences greater than 5% are highlighted in yellow and those that are greater than 10% are highlighted in red. Effect sizes greater than 10 are also highlighted in red.

Table 1: The effect sizes, standard deviations, and percent differences for each of the comparisons performed between the zero and non-zero BIPED resting ICP configurations for each of the metrics examined at the for 18.8 J impacts. Percent differences greater than 5% are highlighted in yellow. Those that are greater than 10% are highlighted in red. Effect sizes greater than 10 are also highlighted in red.

LOW ENERGY IMPACTS - EFFECT SIZE OF PARAM. COMPARED TO BIPED MK2 AT 0 INH2O

	BIPED Mk2 0 inH2O		BIPED Mk2 3 inH2O			BIPED Mk2 6 inH2O			BIPED Mk2 9 inH2O		
METRIC	**Mean**	**Std.**	**Effect Size**	**Std.**	**% diff. in Mean**	**Effect Size**	**Std.**	**% diff. in Mean**	**Effect Size**	**Std.**	**% diff. in Mean**
PEAK LIN. ACCEL. CoG (g)	80.2	1.4	-0.10	0.7	-0.1	0.78	0.7	0.7	-2.18	0.6	-1.7
MAX. FRONT IPP (kPa)	65.0	1.2	-0.45	0.8	-0.5	-1.13	0.7	-1.2	-3.85	0.6	-3.5
MAX. FRONT CSF-LAYER ICP (kPa)	84.3	1.5	-0.13	0.9	-0.1	-1.75	0.9	-1.8	-4.55	0.7	-4.0
MAX. BACK IPP (kPa)	14.8	0.3	-1.59	0.2	-1.9	2.08	0.1	2.0	6.33	0.2	7.9
MIN. BACK IPP (kPa)	-12.8	0.4	0.36	0.2	0.7	-0.95	0.2	-1.6	2.55	0.2	3.8

Table 2: The effect sizes, standard deviations, and percent differences for each of the comparisons performed between the zero and non-zero BIPED resting ICP configurations for each of the metrics examined at the for 37.7 J impacts. Percent differences greater than 5% are highlighted in yellow. Those that are greater than 10% are highlighted in red. Effect sizes greater than 10 are also highlighted in red.

MEDIUM ENERGY IMPACTS - EFFECT SIZE OF PARAM. COMPARED TO BIPED MK2 AT 0 INH2O

	BIPED Mk2 0 inH2O		BIPED Mk2 3 inH2O			BIPED Mk2 6 inH2O			BIPED Mk2 9 inH2O		
METRIC	**Mean**	**Std.**	**Effect Size**	**Std.**	**% diff. in Mean**	**Effect Size**	**Std.**	**% diff. in Mean**	**Effect Size**	**Std.**	**% diff. in Mean**
PEAK LIN. ACCEL. CoG (g)	144.4	2.2	-5.30	1.0	-3.6	-4.22	1.0	-2.9	0.50	1.0	0.4
MAX. FRONT IPP (KPA)	147.1	1.4	1.57	0.8	0.9	2.00	0.7	1.0	7.31	0.8	4.1
MAX. FRONT CSF-LAYER ICP (KPA)	185.4	1.6	1.35	1.0	0.7	1.50	0.9	0.7	8.37	1.0	3.0
MAX. BACK IPP (KPA)	24.2	0.3	-10.68	0.6	-26.0	-16.37	0.5	-32.5	-13.45	0.6	-35.4
MIN. BACK IPP (KPA)	-16.4	0.4	8.74	0.2	11.2	8.91	0.2	11.1	1.46	0.2	2.1

Table 3: The effect sizes, standard deviations, and percent differences for each of the comparisons performed between the zero and non-zero BIPED resting ICP configurations for each of the metrics examined at the for 65.9 J impacts. Percent differences greater than 5% are highlighted in yellow. Those that are greater than 10% are highlighted in red. Effect sizes greater than 10 are also highlighted in red.

HIGH ENERGY IMPACTS - EFFECT SIZE OF PARAM. COMPARED TO BIPED MK2 AT 0 INH2O

	BIPED Mk2 0 inH2O		BIPED Mk2 3 inH2O			BIPED Mk2 6 inH2O			BIPED Mk2 9 inH2O		
METRIC	**Mean**	**Std.**	**Effect Size**	**Std.**	**% diff. in Mean**	**Effect Size**	**Std.**	**% diff. in Mean**	**Effect Size**	**Std.**	**% diff. in Mean**
PEAK LIN. ACCEL. CoG (g)	182.4	1.5	-0.39	0.7	-0.2	-2.78	0.8	-1.2	-2.74	0.8	-1.3
MAX. FRONT IPP (KPA)	196.8	3.9	-0.55	3.1	-0.9	0.48	2.1	0.5	1.58	2.0	1.6
MAX. FRONT CSF-LAYER ICP (KPA)	246.1	3.9	-0.24	3.4	-0.3	1.16	2.2	1.0	2.55	2.2	2.3
MAX. BACK IPP (KPA)	42.4	1.0	-2.72	0.5	-3.4	-5.28	0.7	-9.1	-9.11	0.5	-11.4
MIN. BACK IPP (KPA)	-19.3	0.5	1.93	0.4	3.7	1.25	0.4	2.9	3.45	0.3	5.5

4 Discussion

The purpose of this study was to explore the effects of changing the resting ICP in a surrogate headform subjected to pendulum impacts. The kinematic and pressure responses were measured and recorded for impacts at 18.8, 37.7, and 65.9 J of energy while the BIPED was pressurized to resting ICPs of 0, 3, 6, and 9 inH_2O-gauge. Additional impacts were performed on a Hybrid III headform – the current industry standard headform used for evaluating sport, defense, and automotive safety equipment.

At each of the impact energy levels, the peak global head linear accelerations shown in Figure 4a, as well as the peak impact force shown in Figure 6b, remained fairly consistent across all configurations of resting ICPs. This suggests that any additional internal pressure exerted on the inside of the surrogate skull is not substantial enough to alter its compliance. As such, global head motions in response to a blunt impact, are negligibly affected by increasing the internal pressure of the surrogate headform to anatomically relevant levels. Moreover, the consistency in the peak impact force also suggests that increasing the internal pressure of the surrogate headform does not lead to the skull gaining any substantial resistance to material failures (fractures) caused by blunt impacts.

When compared to the BIPED, the Hybrid III exhibited larger peak global head accelerations and peak impact forces for the same impact energy levels (Figure 6). This is expected since the Hybrid III headform features a skull constructed from metal alloys that are much less compliant than the BIPED's two-piece polyurethane skull. Assuming equivalent transfers of kinetic energy from the pendulum to either the BIPED or the Hybrid III, the Hybrid III's lower compliance allows for less skull deformation during impact than the BIPED, resulting in a higher peak impact force.

Although several statistically significant differences were found between the zero and non-zero resting ICP configurations for all metrics that were recorded, the percent differences in the average metrics between the zero and non-zero resting ICP configurations were nearly all less than 5%. Table 1, Table 2, and Table 3 show that largest percent differences were found in the maximum IPP recorded at the back parenchyma pressure sensor for 37.7 J impacts. This observation may further lament the complexity of the pressure wave that develops inside the skull as a result of a blunt impact.

As previously discussed, changing the resting ICP of the BIPED may have affected the shell stiffness enough to alter the flexural wave speed in the skull or it may have affected the longitudinal wave speed in the brain itself since it is also under elevated stress. The changes in the travel time from the front to the back parenchyma sensors shown in Figure 8 suggest that the arrival of some wave components to the location of the back parenchyma sensor may have indeed changed as the resting ICP was increased. This would give rise to the differences observed in the maximum pressure recorded at the back parenchyma sensor shown in Figure 7.

Wave mechanics aside, these findings must ultimately be considered within the context of evaluating the performance of head protection devices and equipment. If Azar et al. were to replicate their experiments that subjected the BIPED to a free-field blast, but instead used an internally pressurized BIPED, the attenuation that they observed at the front ICP (IPP) sensor for helmeted blasts vs. non-helmeted, is not expected to vary significantly [15]. Any notable differences that correspond to a change in the resting ICP from the present experimental series are observed at the back sensor, away from the coup site. The parenchyma pressure response and any corresponding brain deformations in region of the back sensor are not expected to be the most severe compared to the rest of the brain for the given impact. Therefore, achieving a more accurate biofidelic response in this region than what is already possible without needing to pressurize the BIPED above 0 inH_2O-gauge may not be necessary. Attention can instead be focused on locations where absolute maximum stress and strain are more likely to occur.

Contrary to recent studies that suggest that an increased resting ICP will reduce the relative motion of the brain during impacts, the results of the parenchymal pressures presented in this study demonstrate that the brain does not experience any less energy from the impact due to an increase in the resting ICP [29]–[31]. The responses measured at the back of the brain better suggest that increasing the resting ICP may, in fact, increase the stresses experienced due to blunt impacts. These findings do not support the theory that the brain experiences any less relative motion between it and the skull, and thus does not sustain any less energy from the impact as a result of increasing the resting ICP. It is more likely that the protective effect observed in these studies due to the elevated resting ICPs is, instead, a physiological effect in nature. The present surrogate model does not possess any vascularity, ventricles, or any living tissue that regulates CSF production and absorption that *in-vivo* animal models otherwise would possess. As such, the

discrepancy between the animal models and the present BIPED model could be attributed to a physiological response to the elevated pressure that causes a change in the brain tissue's mechanical properties, such as increased tissue rigidity. Increasing the pressure alone (as was done in this study) has very little effect on physical properties relevant to the fluid mechanics that govern the brain's motion within the CSF since the peak global head kinematic, ICP, and IPP responses do not indicate any reductions in impact severity. If the viscosity could be changed without affecting the other purposes of CSF, then perhaps additional "shock absorption" could be achieved.

5 Conclusions

The effect of changing the resting ICP in a surrogate headform has very little relevant effect on the global head kinematic and the intracranial and intraparenchymal pressure responses in the context of evaluating the energy attenuating and injury prevention capabilities of head protection devices. Differences in the maximum IPP at the location of the back sensor, opposite the impact site, were observed with the changes in the resting ICP. These differences could be a result of altered wave interactions that govern the developing pressure field in the brain during an impact. Small changes in the mechanical properties of the components of the surrogate head, caused by small changes in the resting ICP, could be enough to alter these wave interactions and create regions of elevated pressure. Although changing the resting ICP may alter the intracranial and intraparenchymal pressure wave interactions, the absolute maximum stress and strains the brain experiences during a blunt impact are not expected to deviate significantly. This is because the hypothesized effect that changing the resting ICP has on the head would primarily affect the high frequency pressure waves (0.5 to 2 ms duration) that are generated in the head and not the lower frequency waves (5 to 10 ms duration). These lower frequency waves are generated when the brain impacts the inside of the skull, and they heavily dominate pressure signals measured at the front of the brain where stresses and strains are typically the highest. The results presented in this study do not suggest that increasing the resting ICP leads to any less relative brain motion during impact.

6 References

[1] C. Lefevre-Dognin, M. Cogné, V. Perdrieau, A. Granger, C. Heslot, and P. Azouvi, "Definition and epidemiology of mild traumatic brain injury," *Neurochirurgie*, vol. 67, no. 3, pp. 218–221, May 2021, doi: 10.1016/j.neuchi.2020.02.002.

[2] D. H. Daneshvar, C. J. Nowinski, A. C. McKee, and R. C. Cantu, "The Epidemiology of Sport-Related Concussion," *Clinics in Sports Medicine*, vol. 30, no. 1, pp. 1–17, Jan. 2011, doi: 10.1016/j.csm.2010.08.006.

[3] A. MacAlister, "Surrogate Head Forms for the Evaluation of Head Injury Risk," 2013.

[4] T. Whyte *et al.*, "A Review of Impact Testing Methods for Headgear in Sports: Considerations for Improved Prevention of Head Injury Through Research and Standards," *Journal of Biomechanical Engineering*, vol. 141, no. 7, p. 070803, Jul. 2019, doi: 10.1115/1.4043140.

[5] J. R. Crandall *et al.*, "Human surrogates for injury biomechanics research," *Clin Anat*, vol. 24, no. 3, Art. no. 3, Apr. 2011, doi: 10.1002/ca.21152.

[6] V. R. Hodgson, M. W. Mason, and L. M. Thomas, "Head Model for Impact," SAE International, 1972. [Online]. Available: https://doi.org/10.4271/720969

[7] Eyitejumade A. Sogbesan, "Design and Analysis of Blast Induced Traumatic Brain Injury Mechanism Using a Surrogate Headform: Instrumentation and Outcomes," University of Nebraska-Lincoln, Nebraska, USA, 2011. [Online]. Available: https://apps.dtic.mil/dtic/tr/fulltext/u2/a537846.pdf

[8] S. G. Ganpule, "Mechanics of blast loading on post-mortem human and surrogate heads in the study of Traumatic Brain Injury (TBI) using experimental and computational approaches," p. 289.

[9] S. Ganpule, A. Alai, E. Plougonven, and N. Chandra, "Mechanics of blast loading on the head models in the study of traumatic brain injury using experimental and computational

approaches," *Biomech Model Mechanobiol*, vol. 12, no. 3, pp. 511–531, Jun. 2013, doi: 10.1007/s10237-012-0421-8.

[10] E. A. Kennedy, "The Development and Validation of a Biofidelic Synthetic Eye for the Facial and Ocular CountermeasUre Safety (FOCUS) Headform," Aug. 2007, Accessed: Feb. 27, 2023. [Online]. Available: https://vtechworks.lib.vt.edu/handle/10919/28618

[11] S Ouellet, A. Bouamoul, R. Gauvin, J. S. Binette, K.V. Williams, and L. Martineau, "Development of a Biofidelic Head Surrogate for Blast-Induced Traumatic Brain Injury Assessment." Defence Research and Development Canada (DRDC), 2012.

[12] N. Petrone, G. Carraro, S. D. Castello, L. Broggio, A. Koptyug, and M. Bäckström, "A Novel Instrumented Human Head Surrogate for the Impact Evaluation of Helmets," *Proceedings*, vol. 2, no. 6, p. 269, Feb. 2018, doi: 10.3390/proceedings2060269.

[13] N. Petrone *et al.*, "Feasibility of using a novel instrumented human head surrogate to measure helmet, head and brain kinematics and intracranial pressure during multidirectional impact tests," *Journal of Science and Medicine in Sport*, vol. 22, pp. S78–S84, Aug. 2019, doi: 10.1016/j.jsams.2019.05.015.

[14] A. Azar *et al.*, "An optical fibre transducer for measuring kinetics of skull-brain interaction in a surrogate model of the human head subjected to blast overpressure," *IEEE Sensors Journal*, pp. 1–1, 2018, doi: 10.1109/JSEN.2018.2872392.

[15] A. Azar, K. B. Bhagavathula, J. Hogan, S. Ouellet, S. Satapathy, and C. R. Dennison, "Protective Headgear Attenuates Forces on the Inner Table and Pressure in the Brain Parenchyma During Blast and Impact: An Experimental Study Using a Simulant-Based Surrogate Model of the Human Head," *J Biomech Eng*, vol. 142, no. 4, Apr. 2020, doi: 10.1115/1.4044926.

[16] Y. Li *et al.*, "Evaluating the Intracranial Pressure Biofidelity and Response Repeatability of a Physical Head-Brain Model in Frontal Impacts," *Ann Biomed Eng*, vol. 51, no. 8, pp. 1816–1833, Aug. 2023, doi: 10.1007/s10439-023-03198-x.

[17] A. M. Nahum, R. Smith, and C. C. Ward, “Intracranial Pressure Dynamics During Head Impact,” presented at the 21st Stapp Car Crash Conference, Feb. 1977, p. 770922. doi: 10.4271/770922.

[18] W. N. Hardy *et al.*, “A Study of the Response of the Human Cadaver Head to Impact,” *Stapp Car Crash J*, vol. 51, pp. 17–80, Oct. 2007.

[19] R. L. Stalnaker, J. W. Melvin, G. S. Nusholtz, N. M. Alem, and J. B. Benson, “Head Impact Response,” *SAE Transactions*, vol. 86, pp. 3156–3170, 1977.

[20] C. Got, A. Patel, and G. Walfisch, “Results of Experimental Head Impacts on Cadavers: The Various Data Obtained and Their Relations to Some Measured Physical Parameters,” *STAPP CAR CRASH CONFERENCE*, vol. 22, p. 44.

[21] K. Engelborghs, J. Verlooy, J. Van Reempts, B. Van Deuren, M. Van de Ven, and M. Borgers, “Temporal changes in intracranial pressure in a modified experimental model of closed head injury,” *J Neurosurg*, vol. 89, no. 5, pp. 796–806, Nov. 1998, doi: 10.3171/jns.1998.89.5.0796.

[22] H. Bolouri, A. Säljö, D. C. Viano, and A. Hamberger, “Animal model for sport-related concussion; ICP and cognitive function,” *Acta Neurologica Scandinavica*, vol. 125, no. 4, pp. 241–247, 2012, doi: 10.1111/j.1600-0404.2011.01614.x.

[23] H. Bolouri and H. Zetterberg, “Animal Models for Concussion: Molecular and Cognitive Assessments—Relevance to Sport and Military Concussions,” in *Brain Neurotrauma: Molecular, Neuropsychological, and Rehabilitation Aspects*, F. H. Kobeissy, Ed., in Frontiers in Neuroengineering. , Boca Raton (FL): CRC Press/Taylor & Francis, 2015. Accessed: Apr. 10, 2023. [Online]. Available: http://www.ncbi.nlm.nih.gov/books/NBK299196/

[24] E. G. Takhounts, R. H. Eppinger, J. Q. Campbell, R. E. Tannous, E. D. Power, and L. S. Shook, “On the Development of the SIMon Finite Element Head Model,” *Stapp Car Crash Journal*, vol. 47, pp. 107–133, 2003.

[25] H. Mao *et al.*, “Development of a Finite Element Human Head Model Partially Validated with Thirty Five Experimental Cases,” *Journal of Biomechanical Engineering*, vol. 135, no. 11, 2013.

[26] L. N. Telano and S. Baker, “Physiology, Cerebral Spinal Fluid,” in *StatPearls*, Treasure Island (FL): StatPearls Publishing, 2023. Accessed: Aug. 04, 2023. [Online]. Available: http://www.ncbi.nlm.nih.gov/books/NBK519007/

[27] L. Chen, G. Elias, M. P. Yostos, B. Stimec, J. Fasel, and K. Murphy, “Pathways of cerebrospinal fluid outflow: a deeper understanding of resorption,” *Neuroradiology*, vol. 57, no. 2, pp. 139–147, Feb. 2015, doi: 10.1007/s00234-014-1461-9.

[28] K. Oshio, H. Watanabe, Y. Song, A. S. Verkman, and G. T. Manley, “Reduced cerebrospinal fluid production and intracranial pressure in mice lacking choroid plexus water channel Aquaporin-1,” *The FASEB Journal*, vol. 19, no. 1, pp. 76–78, 2005, doi: https://doi.org/10.1096/fj.04-1711fje.

[29] R. Mannix *et al.*, “Internal Jugular Vein Compression Collar Mitigates Histopathological Alterations after Closed Head Rotational Head Impact in Swine: A Pilot Study,” *Neuroscience*, vol. 437, pp. 132–144, Jun. 2020, doi: 10.1016/j.neuroscience.2020.04.009.

[30] D. W. Smith, J. E. Bailes, J. A. Fisher, J. Robles, R. C. Turner, and J. D. Mills, “Internal Jugular Vein Compression Mitigates Traumatic Axonal Injury in a Rat Model by Reducing the Intracranial Slosh Effect:,” *Neurosurgery*, vol. 70, no. 3, pp. 740–746, Mar. 2012, doi: 10.1227/NEU.0b013e318235b991.

[31] R. C. Turner, Z. J. Naser, J. E. Bailes, D. W. Smith, J. A. Fisher, and C. L. Rosen, “Effect of slosh mitigation on histologic markers of traumatic brain injury: Laboratory investigation,” *Journal of Neurosurgery*, vol. 117, no. 6, pp. 1110–1118, Dec. 2012, doi: 10.3171/2012.8.JNS12358.

[32] J. A. Kopecky and E. A. Ripperger, “Closed brain injuries: An engineering analysis,” *Journal of Biomechanics*, vol. 2, no. 1, pp. 29–34, Mar. 1969, doi: 10.1016/0021-9290(69)90039-6.

[33] C. W. Pearce and P. G. Young, “On the Pressure Response in the Brain due to Short Duration Blunt Impacts,” *PLOS ONE*, vol. 9, no. 12, p. e114292, Dec. 2014, doi: 10.1371/journal.pone.0114292.

[34] P. A. Taylor and C. C. Ford, “Simulation of Blast-Induced Early-Time Intracranial Wave Physics leading to Traumatic Brain Injury,” *Journal of Biomechanical Engineering*, vol. 131, no. 6, Apr. 2009, doi: 10.1115/1.3118765.

[35] M. Grujicic, W. C. Bell, B. Pandurangan, and P. S. Glomski, “Fluid/Structure Interaction Computational Investigation of Blast-Wave Mitigation Efficacy of the Advanced Combat Helmet,” *J. of Materi Eng and Perform*, vol. 20, no. 6, pp. 877–893, Aug. 2011, doi: 10.1007/s11665-010-9724-z.

[36] S. Ganpule and N. Chandra, “Mechanics of Interaction of Blast Waves on Surrogate Head: Effect of Head Orientation,” presented at the ASME 2013 Summer Bioengineering Conference, American Society of Mechanical Engineers Digital Collection, Jan. 2014. doi: 10.1115/SBC2013-14754.

[37] S. Ouellet, C. Bir, and A. Bouamoul, “Direct comparison of the primary blast response of a physical head model with post-mortem human subjects,” in *PASS 2014, Cambridge UK*, Sep. 2014.

[38] S. Ouellet and M. Philippens, “The multi-modal responses of a physical head model subjected to various blast exposure conditions,” *Shock Waves*, vol. 28, no. 1, pp. 19–36, Jan. 2018, doi: 10.1007/s00193-017-0771-3.

[39] L. Zhang, Z. Zhang, R. Zhang, M. Gao, and J. Xie, “The Ultrasonic P-Wave Velocity-Stress Relationship and Energy Evolution of Sandstone under Uniaxial Loading-Unloading Conditions,” *Advances in Materials Science and Engineering*, vol. 2021, p. e9921716, Jun. 2021, doi: 10.1155/2021/9921716.

[40] M. Otténio, M. Destrade, and R. W. Ogden, “Acoustic waves at the interface of a pre-stressed incompressible elastic solid and a viscous fluid,” *International Journal of Non-Linear Mechanics*, vol. 42, no. 2, pp. 310–320, Mar. 2007, doi: 10.1016/j.ijnonlinmec.2006.10.001.

[41] M. Destrade and R. W. Ogden, “On stress-dependent elastic moduli and wave speeds,” *IMA Journal of Applied Mathematics*, vol. 78, no. 5, pp. 965–997, Oct. 2013, doi: 10.1093/imamat/hxs003.

[42] Y. Li, S. Ouellet, A. H. Vette, D. Raboud, A. Martin, and C. R. Dennison, “Evaluation of the Kinematic Biofidelity and Inter-Test Repeatability of Global Accelerations and Brain Parenchyma Pressure for a Head–Brain Physical Model,” *Journal of Biomechanical Engineering*, vol. 143, no. 9, p. 091006, Sep. 2021, doi: 10.1115/1.4050752.

[43] S. of A. Engineers, “J211 - (R) Instrumentation for impact test - Part 1 - electronic instrumentation,” Society of Automotive Engineers, 2003.

Appendix B: Results of CORA

The results from the CORA are summarized below. On the first attempt, the parietal pressure signal from the cadaver data was compared to both the left and right CSF ICP signals of the BIPED. The results indicated that increasing the resting intracranial pressure (ICP) improved the biofidelity rating of the BIPED Mk. 2. Upon examination, the right ICP signal of the BIPED seemed to improve while the others remained consistent. Following this identification, the CORA run was reconfigured to exclude the right ICP signal which then showed no apparent relationship between resting ICP and the CORA rating.

A closer look revealed that the right ICP signal appeared to be improving its rating because the phase shift and pressure amplitudes were more consistent with the cadaver's *left* parietal reference signal. Considering that the left and right ICP sensors on the BIPED were mounted symmetrically and the intended impact site was directly in line with the sagittal plane, the left and right sensors should yield nearly identical signals, yet they did not. It was found that the left and right ICP signals became more consistent with each other at the higher resting ICPs than they were at the lower resting ICPs. Given that the experimental series began at the lower resting ICPs and finished at the higher resting ICPs, it is very likely that the positioning of the impact site and direction relative to the sagittal plane improved throughout the testing. Although this would be considered a very obvious systematic bias, the effects of it were quite subtle and only noticeable when comparing the left and right ICP signals with the CORA method.

After further considering that the reference side ICP signal was derived from the left parietal bone of the cadaver model, the left ICP signal from the BIPED was chosen to remain in the analysis while the right ICP signal was removed.

The CORA results that included both the left and right ICP signals referenced to the cadaver left parietal signal are shown below followed the results that excluded the right signal.

Summary Report Date: Nov 21 2023

Rating of: BIPED Pressurized to Different Resting ICPs

Description: BIPED has been pressurized to 0, 3, 6, 9inH2O and tested against Nahum and Smith Cadaver Experiment 37

Rating:

No.	Load Case	Rating	Weight
1	Evaluation of 7.9kN Impacts at 0inH20	0.597	0.250
2	Evaluation of 7.9kN Impacts at 3inH20	0.606	0.250
3	Evaluation of 7.9kN Impacts at 6inH20	0.608	0.250
4	Evaluation of 7.9kN Impacts at 9inH20	0.619	0.250
	Total rating	**0.608**	1.0

Summary Report Date: Nov 22 2023

Rating of: BIPED Pressurized to Different Resting ICPs

Description: BIPED has been pressurized to 0, 3, 6, 9inH2O and tested against Nahum and Smith Cadaver Experiment 37

Rating:

No.	Load Case	Rating	Weight
1	Evaluation of 7.9kN Impacts at 0inH20	0.614	0.250
2	Evaluation of 7.9kN Impacts at 3inH20	0.616	0.250
3	Evaluation of 7.9kN Impacts at 6inH20	0.612	0.250
4	Evaluation of 7.9kN Impacts at 9inH20	0.617	0.250
	Total rating	**0.615**	1.0